

1

SECURITY CLASSIFICATION OF THIS PAGE

REPORT DOCUMENTATION PAGE

Form Approved  
OMB No. 0704-0188

1a. REPORT SECURITY CLASSIFICATION  
UNCLASSIFIED

1b. RESTRICTIVE MARKINGS  
NONE

2a.  
2b.

3. DISTRIBUTION / AVAILABILITY OF REPORT  
APPROVED FOR PUBLIC RELEASE;  
DISTRIBUTION UNLIMITED.

4. P  
**AD-A220 914**

5. MONITORING ORGANIZATION REPORT NUMBER(S)  
AFIT/CI/CIA- 90-008D

6a. NAME OF PERFORMING ORGANIZATION  
AFIT STUDENT AT  
Univ of New Mexico

6b. OFFICE SYMBOL  
(if applicable)

7a. NAME OF MONITORING ORGANIZATION  
AFIT/CIA

6c. ADDRESS (City, State, and ZIP Code)

7b. ADDRESS (City, State, and ZIP Code)  
Wright-Patterson AFB OH 45433-6583

8a. NAME OF FUNDING / SPONSORING ORGANIZATION

8b. OFFICE SYMBOL  
(if applicable)

9. PROCUREMENT INSTRUMENT IDENTIFICATION NUMBER

8c. ADDRESS (City, State, and ZIP Code)

10. SOURCE OF FUNDING NUMBERS  
PROGRAM ELEMENT NO. PROJECT NO. TASK NO. WORK UNIT ACCESSION NO.

11. TITLE (Include Security Classification) (UNCLASSIFIED)  
Heterodyne Characterization of High-Speed Photomixers for the Ultraviolet

12. PERSONAL AUTHOR(S)  
Billy Wayne Mullins

13a. TYPE OF REPORT  
THESIS/DISSERTATION

13b. TIME COVERED  
FROM \_\_\_\_\_ TO \_\_\_\_\_

14. DATE OF REPORT (Year, Month, Day)  
1990

15. PAGE COUNT  
199

16. SUPPLEMENTARY NOTATION  
APPROVED FOR PUBLIC RELEASE IAW AFR 190-1  
ERNEST A. HAYGOOD, 1st Lt, USAF  
Executive Officer, Civilian Institution Programs

| 17. COSATI CODES |       |           |
|------------------|-------|-----------|
| FIELD            | GROUP | SUB-GROUP |
|                  |       |           |
|                  |       |           |
|                  |       |           |

18. SUBJECT TERMS (Continue on reverse if necessary and identify by block number)

19. ABSTRACT (Continue on reverse if necessary and identify by block number)

**SDTIC**  
**ELECTE**  
**APR 25 1990**  
**B D**

90 04 23 055

20. DISTRIBUTION / AVAILABILITY OF ABSTRACT  
 UNCLASSIFIED/UNLIMITED  SAME AS RPT.  DTIC USERS

21. ABSTRACT SECURITY CLASSIFICATION  
UNCLASSIFIED

22a. NAME OF RESPONSIBLE INDIVIDUAL  
ERNEST A. HAYGOOD, 1st Lt, USAF

22b. TELEPHONE (Include Area Code)  
(513) 255-2259

22c. OFFICE SYMBOL  
AFIT/CI

HETERODYNE CHARACTERIZATION OF HIGH-SPEED  
PHOTOMIXERS FOR THE ULTRAVIOLET

BY

BILLY WAYNE MULLINS

B.S., Angelo State University, 1978

M.S., Air Force Institute of Technology, 1979

DISSERTATION

Submitted in Partial Fulfillment of the  
Requirements for the Degree of

Doctor of Philosophy in Physics

*The University of New Mexico*  
Albuquerque, New Mexico

December, 1989

HETERODYNE CHARACTERIZATION OF HIGH-SPEED  
PHOTOMIXERS FOR THE ULTRAVIOLET

BY

BILLY WAYNE MULLINS

ABSTRACT OF DISSERTATION

Submitted in Partial Fulfillment of the  
Requirements for the Degree of

Doctor of Philosophy in Physics

The University of New Mexico  
Albuquerque, New Mexico

December, 1989

*To my loving wife Jill, who with her love, devotion, encouragement, and occasional swift kick made this work possible.*

| Accession For       |                                     |
|---------------------|-------------------------------------|
| NTIS GRA&I          | <input checked="" type="checkbox"/> |
| DTIC TAB            | <input type="checkbox"/>            |
| Unannounced         | <input type="checkbox"/>            |
| Justification _____ |                                     |
| By _____            |                                     |
| Distribution/       |                                     |
| Availability Codes  |                                     |
| Dist                | Avail and/or<br>Special             |
| A-1                 |                                     |

Billy Wayne Mullins

*Candidate*

Physics

*Department*

This thesis is approved, and it is acceptable in quality  
and form for publication on microfilm:

*Approved by the Thesis Committee:*

*Steven R. J. Bruner* . Chairperson

*John K. Wain*

*W. Beale*

*Ken Jungling*

Accepted:

\_\_\_\_\_  
*Dean, Graduate School*

\_\_\_\_\_  
*Date*

Heterodyne Characterization of High-Speed  
Photomixers for the Ultraviolet

Billy Wayne Mullins

B.S. Physics, Angelo State University, 1978

M.S. Eng. Physics, Air Force Inst. of Technology, 1979

Ph.D. Physics, Univ. of New Mexico, 1989

A detailed experimental and theoretical investigation of high-speed photodiodes is presented. Detector geometries included both planar and interdigitated designs with gap widths of 1.0, 3.0 and 4.5  $\mu\text{m}$ . Detailed photomixing measurements were performed using a ultraviolet heterodyne system operating at 334.5 nm. Measurements included frequency response to 10 GHz as a function of beam position, bias and optical power. Limited measurements were made to 18 GHz. A detailed, first principles, model of msm-photodiode frequency response including carrier drift velocity, diffusion, recombination and beam position is derived. Including packaging effects, good agreement was found between the experimental results and the model.

A unique uv-heterodyne characterization system was assembled and calibrated for absolute responsivity,  $R(\omega)$ , from d.c. to 18 GHz. The system incorporated a single frequency Ar-ion laser uv local oscillator (334.5 nm) and a frequency-doubled dye laser signal source. Mode matching optics provided a spot as small as 1.7  $\mu\text{m}$  (FWHM) at the detector with a wavefront matching error of less than 5% calibrated against single laser beam dc measurements. An rf-spectrum analyzer was

used to monitor the heterodyne response. The rf-measurement system response was calibrated with a network analyzer and the data corrected to provide accurate detector/ package measurements.

The detector modeling includes the most detailed evaluation of msm photodetector frequency response presented to date. The model proceeds from a modulated point source excitation. The very short uv absorption length,  $\sim 10$  nm, and the high biases (hence short transit times) imply negligible diffusion away from the surface and permit an analytical two-dimensional solution for the currents under the assumption of a uniform carrier drift velocity. This solution is numerically integrated to allow for actual beam dimensions.

Planar-geometry detectors were extensively tested and the results compared with the model to frequencies of 10 GHz. The inductance of the bonding wire between the detector and a microstrip transmission line was found to limit the overall response. Including a simple-pole frequency response to model this inductive effect, good agreement for the detector response as a function of beam position and bias was found.

Measurements to 18 GHz on a  $4.5\text{-}\mu\text{m}$  gap detector were also in good agreement with the model predictions. With a properly designed rf package, the  $4.5\text{-}\mu\text{m}$  planar gap geometry should yield a 30% quantum efficient, 21-GHz bandwidth detector. For a  $1.0\text{-}\mu\text{m}$  gap geometry, the model predicts a 75-GHz bandwidth Si photodiode. The good agreement with the model also indicates that the charge transport processes near the Si surface are comparable with bulk properties.

Low-frequency gain, as seen in all msm photodiodes, in the detectors were compared to a simple-pole frequency response. The bandwidth of this gain mechanism was found to be directly related to the

drift velocity of the minority carriers. The gain amplitude was found to be related to the minority carrier transit time.

The planar gap geometries were compared to the the interdigitated detectors of equal gap dimensions.  $R(\omega)$  for the interdigitated design was less sensitive to changes in beam position and bias than the planar design. The corners of the interdigitated electrodes cause a locally higher  $\mathbf{E}$ -field, increasing the carrier drift velocity. Responsivity maps the active region of both planar and interdigitated detectors showed regions of very high responsivity near all of the electrode corners confirming the presence of locally higher  $\mathbf{E}$ -fields. These maps also showed that the active area of the planar-gap detectors decreasing with increasing frequency. The interdigitated detectors showed a decrease in active area going from d.c. to 1 GHz, but remained constant from 1 GHz to 9 GHz. The decreased sensitivity in  $R(\omega)$  and the constant active area at rf frequencies of the interdigitated design indicate that it is a superior detector design over the planar geometry.

## TABLE OF CONTENTS

| CHAPTER  | Page |
|--|------|
| I. INTRODUCTION .....                                      | 1    |
| A. Motivation .....  | 1    |
| B. Background .....  | 3    |
| C. Reported MSM Detector Properties .....                  | 6    |
| D. Detector Fabrication .....                              | 8    |
| E. Dissertation Contents Summary .....                     | 9    |
| II. THEORY .....   | 22   |
| A. Introduction .....                                      | 22   |
| B. Heterodyne Signal .....                                 | 22   |
| C. Metal-Semiconductor-Metal Photodiode .....              | 33   |
| D. Electric Fields due to Coplanar Pads .....              | 39   |
| E. Detector Photocurrent in an MSM<br>Photodiode .....     | 42   |
| F. Predicted Detector Performance<br>and Limitations ..... | 61   |
| III. EXPERIMENTAL APPARATUS .....                          | 86   |
| A. Introduction .....                                      | 86   |
| B. The Experimental Arrangement .....                      | 86   |
| C. System Calibration .....                                | 90   |
| D. Beam Alignment Procedure .....                          | 93   |
| E. Detector Alignment .....                                | 96   |

## TABLE OF CONTENTS (Cont.)

| CHAPTER   | Page |
|---|------|
| IV. RESULTS .....   | 108  |
| A. Introduction .....   | 108  |
| B. Experimental Procedure .....   | 108  |
| C. Data Fitting .....   | 112  |
| D. Saturation and Band Bending Test .....   | 115  |
| E. DC current versus voltage results .....  | 117  |
| F. $R(\omega)$ versus Bias and Beam Position<br>for Planar Geometry Detectors ..... | 121  |
| G. Performance of the 4.5- $\mu\text{m}$ Detector<br>to 18 GHz .....                | 128  |
| H. Full Bandwidth Analysis of Planar<br>Gap Detectors .....                         | 130  |
| I. Planar versus Interdigitated<br>Frequency Response .....                         | 135  |
| J. Responsivity Maps .....  | 136  |
| K. GaAs Detector Results .....  | 141  |
| V. CONCLUSIONS .....  | 178  |
| APPENDICES  |      |
| Appendix I: Photodiode or Photoconductor? .....                                     | 187  |

## List of Figures

| Figure |   | Page |
|--------|---|------|
| 1      | MSM detector geometries .....   | 11   |
| 2      | MSM detector construction .....   | 12   |
| 3      | MSM detector mounted on<br>microstrip waveguide package .....                             | 12   |
| 4      | Two Gaussian Beams with a Tilt $\theta$<br>between them .....                             | 69   |
| 5      | Mixing Efficiency versus Tilt Angle<br>for 1.7, 10 and 100 $\mu\text{m}$ FWHM Spots ..... | 70   |
| 6      | MSM Photodiode Band Structure versus<br>Bias Voltage .....                                | 71   |
| 7      | Simple Coplanar Geometry .....  | 72   |
| 8      | Simplified Coplanar MSM Geometry .....  | 73   |
| 9      | Semi-Infinite Coplanar Metal Pads .....   | 74   |
| 10     | Temporal MSM Photocurrent .....   | 75   |
| 11     | Predicted $R(\omega)$ for a 4.5- $\mu\text{m}$ Gap<br>Detector versus Bias Voltage .....  | 76   |
| 12     | Predicted $R(\omega)$ for a 3.0- $\mu\text{m}$ Gap Detector<br>versus Bias Voltage .....  | 77   |
| 13     | Predicted $R(\omega)$ for a 1.0- $\mu\text{m}$ Gap Detector<br>versus Bias Voltage .....  | 78   |
| 14     | Predicted $R(\omega)$ for a 4.5- $\mu\text{m}$ Gap Detector<br>versus Beam Position ..... | 79   |
| 15     | Predicted $R(\omega)$ for a 3.0- $\mu\text{m}$ Gap Detector<br>versus Beam Position ..... | 80   |

## List of Figures (Cont.)

| Figure |   | Page |
|--------|---|------|
| 16     | Predicted $R(\omega)$ for a 1.0- $\mu\text{m}$ Gap Detector<br>versus Beam Position .....                 | 81   |
| 17     | UV Heterodyne System .....  | 99   |
| 18     | Gain versus Frequency for the<br>400 MHz to 2.0 GHz Amplifier .....                                       | 100  |
| 19     | Gain versus Frequency for the<br>2.0 GHz to 8.0 GHz Amplifier .....                                       | 101  |
| 20     | Gain versus Frequency for the<br>5.0 GHz to 10.0 GHz Amplifier .....                                      | 102  |
| 21     | Mixing Efficiency Test .....  | 103  |
| 22     | Beam Alignment on the Detector<br>Parallel to the Detector Gap .....                                      | 104  |
| 23     | Beam Alignment on the Detector<br>Perpendicular to the Detector Gap .....                                 | 105  |
| 24     | Day-to-Day Reproducibility .....  | 106  |
| 25     | Detector Saturation Test .....  | 143  |
| 26     | D.C Current-Voltage Characteristics for 4.5,<br>3.0 and 1.0- $\mu\text{m}$ Interdigitated Detectors ..... | 144  |
| 27     | D.C Current-Voltage Characteristics for<br>4.5, 3.0 and 1.0- $\mu\text{m}$ Planar Detectors .....         | 145  |
| 28     | RF Package L/R Bandwidth Determination .....  | 146  |
| 29     | 4.5- $\mu\text{m}$ Planar Detector $R(\omega)$ to 18 GHz .....  | 147  |
| 30     | High-Frequency Model Fit to 18 GHz<br>for a 4.5- $\mu\text{m}$ Planar Gap Detector .....                  | 148  |

## List of Figures (Cont.)

| Figure |  | Page |
|--------|--|------|
| 31     | R( $\omega$ ) versus Bias for a 4.5- $\mu\text{m}$ Planar<br>Gap Detector .....                  | 149  |
| 32     | R( $\omega$ ) versus Beam Position for a<br>4.5- $\mu\text{m}$ Planar Gap Detector .....         | 150  |
| 33     | R( $\omega$ ) versus Bias for a 3.0- $\mu\text{m}$ Planar<br>Gap Detector .....                  | 151  |
| 34     | Low-Frequency Mechanism Bandwidth<br>versus Hole Drift Velocity .....                            | 152  |
| 35     | R( $\omega$ ) versus Bias for a 4.5- $\mu\text{m}$ Planar<br>Gap Detector .....                  | 153  |
| 36     | R( $\omega$ ) versus Bias for a 4.5- $\mu\text{m}$<br>Interdigitated Gap Detector .....          | 154  |
| 37     | R( $\omega$ ) versus Beam Position for a<br>4.5- $\mu\text{m}$ Planar Gap Detector .....         | 155  |
| 38     | R( $\omega$ ) versus Beam Position for a 4.5- $\mu\text{m}$<br>Interdigitated Gap Detector ..... | 156  |
| 39     | D.C. Responsivity Map of a<br>3.0- $\mu\text{m}$ Planar Gap Detector. (V = 3.0 V) .....          | 157  |
| 40     | Contour Plot of Figure 39 .....  | 158  |
| 41     | D.C. Responsivity Map of a 3.0- $\mu\text{m}$<br>Planar Gap Detector. (V = 15.0 V) .....         | 159  |
| 42     | 1 GHz Responsivity map of a 3.0- $\mu\text{m}$<br>Planar Gap Detector. (V = 3.0 V) .....         | 160  |
| 43     | Contour Plot of Figure 42 .....  | 161  |

## List of Figures (Cont.)

| Figure | Page   |
|--------|--|
| 44     | 1 GHz Responsivity map of a 3.0- $\mu\text{m}$<br>Planar Gap Detector. (V = 15.0 V) ..... 162                  |
| 45     | 9 GHz Responsivity map of a 3.0- $\mu\text{m}$<br>Planar Gap Detector. (V = 3.0 V) ..... 163                   |
| 46     | Contour Plot of Figure 45 ..... 164  |
| 47     | 9 GHz Responsivity map of a 3.0- $\mu\text{m}$<br>Planar Gap Detector. (V = 15.0 V) ..... 165                  |
| 48     | Contour Plot of Figure 47 ..... 166  |
| 49     | D.C. Responsivity Contour Plot of a 3.0- $\mu\text{m}$<br>Interdigitated Gap Detector. (V = 3.0 V) ..... 167   |
| 50     | 1 GHz Responsivity Contour Plot of a 3.0- $\mu\text{m}$<br>Interdigitated Gap Detector. (V = 3.0 V) ..... 168  |
| 51     | 9 GHz Responsivity Contour Plot of a 3.0- $\mu\text{m}$<br>Interdigitated Gap Detector. (V = 3.0 V) ..... 169  |
| 52     | 1 GHz Responsivity Contour Plot of a 3.0- $\mu\text{m}$<br>Interdigitated Gap Detector. (V = 15.0 V) ..... 170 |
| 53     | 9 GHz Responsivity Contour Plot of a 3.0- $\mu\text{m}$<br>Interdigitated Gap Detector. (V = 15.0 V) ..... 171 |
| 54     | D.C. Photoresponse versus Time of a<br>GaAs MSM Detector ..... 172   |
| 55     | Proposed Mesa MSM Photodiode Design,<br>End View ..... 185   |

## List of Tables

| Table |   | Page |
|-------|---|------|
| 1     | Mixing Efficiency verses Tilt Between<br>Two Guassian Beams .....   | 82   |
| 2     | Deviation in Electric Field Strength as a<br>Function of Position from The Surface .....                                  | 82   |
| 3     | Bias for a given electric field strength .....  | 83   |
| 4     | -3 db Points of three detectors<br>vs applied E-field .....   | 83   |
| 5     | -3db Points for an L/R Circuit,<br>with $R = 50 \Omega$ .....   | 84   |
| 6     | Coefficients for 10th Order Fit for<br>Amplifier Gain as a Function of<br>Frequency ( $G(\text{db}) = \sum_n f^n$ ) ..... | 107  |
| 7     | Bias and beam Position for<br>the 4.5- $\mu\text{m}$ planar detector .....  | 173  |
| 8     | Beam Position Fit to High-frequency Data .....  | 173  |
| 9     | Data fit variables .....  | 174  |
| 10    | Fit Parameters for a 4.5- $\mu\text{m}$ Planar Detector .....   | 175  |
| 11    | Low-frequency characteristics versus<br>hole drift velocity .....   | 176  |
| 12    | LF Gain vs Bias and Position .....  | 176  |

## Chapter 1

### Introduction

#### A. Motivation

Recent interest in optical communication and Doppler laser radar has led to increased research on very fast, highly efficient photodetectors. Advances in pico- and femto-second laser spectroscopy, in the near IR and visible spectral regions, have led to an improved understanding of the time evolution of many atomic and molecular processes. With a higher probe photon energy, this research can be extended to the physics of inner atomic shell transitions or very tightly bound molecules, for example. In order to access this high-energy spectral region, not only are ultrafast uv laser sources needed, but also high-speed, efficient uv photodetectors are required. The advent of excimer lasers and efficient frequency doubling crystals has opened up the once inaccessible region of ultrafast ultraviolet laser spectroscopy. In many areas, the present research trends appear to be moving towards shorter wavelengths for the higher resolution or higher photon energies available with uv light.

For example, a shorter wavelength Doppler laser-radar system would have many advantages over its microwave counterpart, if a suitable detector were available. To make an effective Doppler laser radar, the system's operational wavelength must be in one of the atmospheric transmission windows. An acceptable window lies between 350 nm and 250 nm. Also, the system's detector, called a photomixer, must have an acceptable frequency response, noise equivalent power, and quantum efficiency. A realistic upper bound for the maximum frequency shift a

Doppler laser radar would have to detect is 10 GHz. This corresponds to a closing velocity of 3.333 km/sec, which is faster than present aircraft, but in the realm of reentry speeds of low earth orbiting objects.

In response to this push for faster ultraviolet detectors, the Center for High Technology Materials (CHTM) is developing advanced ultraviolet photomixers.

The main thrust of this research was to study the limiting physics of very fast uv photomixers. In particular, this research program investigated the effects of incident power, biasing potential, and detector geometry on the limiting frequency response characteristics of the photomixer. Also studied was the detector response versus beam position on the detector surface. These responsivity maps are correlated to the applied **E**-field and detector geometry and with detector performance.

The realm of uv-detector characteristics and their limiting physical properties is basically unexplored. The bulk of the research on fast photodetectors has been associated with developments in fiber optic communications and has been concentrated on the red and near IR regions of the spectrum. At these wavelengths, the relatively long absorption lengths,  $\delta \approx 1.0 \mu\text{m}$ , imply that the bulk properties of the detector material will be the limiting factors.

By shifting to uv wavelengths, the absorption length,  $\delta$ , is decreased to approximately 10 nm and is relatively material independent. At these shallow depths in the crystal the surface physics of the material could influence detector response. Work has been reported on surface trapping and recombination at wavelengths as short as 600 nm.

However, this still basically probes the bulk properties since  $\delta = 0.22 \mu\text{m}$ .<sup>1</sup> Hence, any work looking at the basic properties in the uv could reveal new surface physics and surface carrier dynamics.

Another region of interest that has not yet been adequately explored is the correlation between temporal and frequency domain measurements on the same detector. Most of the research has used impulse, autocorrelation, or correlation response to test their detectors, with a few papers reporting a heterodyne technique. Deconvolving detector frequency response from impulse measurements is not an easy or well understood task. Autocorrelation measurement avoids the need for the very high speed electronics involved with impulse measurements, but requires that the detector have a nonlinear response to beam intensity and hence is useless on linear detectors.

A detailed photodiode model for both an impulse and heterodyne input signal is developed from basic principles. It is shown, as required, that the impulse and heterodyne responses of the detector are a Fourier transform pair. The model is extensively compared to experimental data out to 10 GHz. Some comparison is also made out to 18 GHz. Finally, a comparison of photovoltaic and photoconductive detection is presented. This is done in order to clarify what appears to be some confusion in the open literature between these detection mechanisms.

## B. Background

There has been extensive work to develop high-speed, low-noise photodetectors in the 0.8 - 1.5- $\mu\text{m}$  wavelength range for use in optical communication systems.<sup>2-30</sup> Two general device design types have been

developed, these being either vertical p-i-n<sup>5-14,31</sup> or planar interdigitated<sup>15-18,29,30,32-38</sup> geometries. Device materials tested range from Si<sup>33,35,37,40-42</sup> and InGaAs<sup>5,6,11-13,38</sup> to strained-layer superlattices<sup>22-27</sup>, to name the most predominant materials. In the near infrared region some very fast, highly responsive detectors have been fabricated. Frequency responses up to 67 GHz<sup>43</sup> and quantum efficiencies of greater than 3000% (a gain of 35)<sup>2</sup> have been reported for p-i-n devices, but not on the same detector. The fastest interdigitated design has a 105 GHz frequency response,<sup>44,45</sup> with the best quantum efficiency being 2500% (a 20 db gain with a base 25% quantum efficiency)<sup>45</sup>, again not on the same detector.

Detector frequency response has generally been evaluated from measurements of detector impulse or autocorrelation response. To determine the temporal, and hence frequency, response from impulse measurements the impulse response of the sampling electronics, amplifier, connecting cables, etc. must be deconvolved from the impulse data to obtain the true temporal response of the detector. This process is not that well understood. Also, until very recently (within the last year) the upper limit on commercially available oscilloscopes used to measure the impulse response was 1 GHz, or 160 psec. Sampling heads could move this upper frequency limit out to about 3 GHz or 50 psec. These frequencies/speeds are too low/slow to be of value in state-of-the-art high-speed detector research. Autocorrelation measurements avoid this problem. However, there is significant uncertainty in the determination of the impulse response from the autocorrelation signal. Sala, et. al.<sup>46</sup> have analytically derived the autocorrelation functions for pulses with different temporal intensity profiles. From these

results they determined the FWHM point in time for the initial pulse and the autocorrelation signal of an infinitely fast detector,  $t_i$  and  $t_d$ , respectively. They found that the ratio  $t_d/t_i$  was highly dependent upon the actual temporal profile of the incident pulse varying by up to a factor of 2.5 for different pulse shapes. Hence, an autocorrelation measurement has some built-in unknowns unless the true beam profile is constant known and remains constant from pulse to pulse. Most papers do not report on how this problem was handled in their autocorrelation analysis, while some just take a "conservative estimate of 1.5".<sup>47</sup>

True frequency response curves can be obtained via a heterodyne technique. As demonstrated below, these frequency response measurements give considerably more detailed information than does a temporal response measurement. In the 0.8 to 1.3- $\mu\text{m}$  wavelength region, only three papers have reported detector frequency responses measured in the frequency domain via a heterodyne technique.<sup>29,36,48</sup>

An extensive literature search revealed very little uv detector work. High-speed uv detectors have been attempted using vertical Schottky barrier<sup>32</sup>, planar interdigitated Schottky barrier<sup>37,40</sup>, Si p-n junction<sup>36</sup>, and vertical p-i-n with a thin p-layer<sup>31</sup> designs with only moderate success. The most promising design was the planar interdigitated Schottky barrier which had an overall quantum efficiency of 12% at 337 nm and a frequency response of 5.3 GHz at  $\approx$  800 nm.<sup>40</sup> However, since this wavelength, 800 nm, will penetrate approximately 100 times further into the material than uv wavelengths, this detector's frequency characteristics were probably determined more by the bulk properties than its surface characteristics. Also, no reports where

found that had made any picosecond impulse, autocorrelation, or heterodyne response measurements at uv wavelengths.

### C. Reported MSM Detector Properties

Due to the ease of fabrication and previously reported uv response, the detector design chosen for this study was a planar, back-to-back Schottky photodiode. The detector consists of two metal pads on a semiconductor surface comprising a metal-semiconductor-metal (msm) diode. The exposed semiconductor, between the metal pads, can be fully depleted by an appropriate applied bias. This depleted region is the photosensitive region of the diode and the high applied fields result in very fast drift velocities of the charge carriers. The direct access to the depletion region by uv photons avoids the short absorption length problem inherent in other designs.

MSM devices have been fabricated in a number of metalization geometries, with the predominant design being interdigitated metal fingers. Both photovoltaic and photoconductive devices have been made and tested. A photovoltaic device will have one Schottky barrier diode under reverse bias. This barrier is sufficient to prevent photoconductive gain and these detectors are usually very fast and highly responsive.<sup>30,36,37,39</sup> A photoconductive detector will have either both contacts ohmic<sup>15,17,33-35,38</sup>, or one ohmic contact and one forward-biased Schottky diode contact.<sup>29</sup> The photoconductor is generally recombination lifetime limited. This is because when a minority carrier exits one side of the photoconductor another minority carrier easily enters the semiconductor on the other side of the device. Thus, charge exits one side, the current due to this charge travels

around the circuit, and a like charge enters the semiconductor on the other side of the device. This round trip phenomenon is the photoconductive gain mechanism since a single electron-hole pair, generated by a single photon, results in several times the current corresponding to a single charge in the external circuit. This round trip phenomena continues until the minority carrier recombines.<sup>15,17,29,33-35,38</sup> High speed operation has been observed in photoconductors, but always at the expense of sensitivity. High-speed operation is achieved by reduction of the recombination lifetime, usually by ion-implantation of the depletion region.<sup>33,35,38</sup> Recombination lifetimes as short as 2-3 psec have been reported.<sup>33,38</sup> However, the measured mobility in these detectors drops drastically, 250 cm<sup>2</sup>/Vs for Si<sup>35</sup> and 100 cm<sup>2</sup>/Vs in InGaAs.<sup>38</sup> Not surprisingly, the quantum efficiencies of these detectors are very low, ranging from 0.11%<sup>33</sup> to as low as 1.48 x 10<sup>-6</sup>%.<sup>38</sup>

In the ultraviolet, where for a given input intensity the photon number is reduced compared with visible and near-IR spectral regions, a low efficiency detector is very unattractive. The more efficient photovoltaic detector, which is transit-time limited, seems a better choice when a small input signal is expected. There has been much attention in calculating the electric fields in these structures.<sup>37,40,49,50</sup> The theoretical work is entirely comprised of numerical solutions to several partial differential equations to arrive at the electric field in the semiconductor. Unfortunately, in each case, the MSM detector geometry has been simplified to semi-infinite coplanar pads, i.e. fringing effects have been neglected. Under this assumption, there is no need to resort to a numerical approach, the

analytical solution to this problem has been available since at least 1944.<sup>51</sup> However, once the fields in the detector are known, then the current from, say an IR source, must be calculated numerically, since a closed analytical solution for the current can not be obtained. At ultraviolet wavelengths, however, the very short penetration depths allow some approximations that permit for an analytical solution for the charge density, current density, and external current. These are derived in the next chapter.

One common phenomenon is seen in all of the photovoltaic msm devices reviewed. They all show a high quantum efficiency, >100%, at low frequency.<sup>15,17,18,30,36,37,39</sup> Some explanations have been put forth, but no definitive analytic models have been published. This phenomenon is seen in the devices tested in this study.

#### D. Detector Fabrication

The detectors used in this work were those fabricated in the CHTM facilities as part of this detector development program. These detectors have been fabricated by S. F. Soares as part of his dissertation.<sup>52</sup> The detectors are all metal-semiconductor-metal, back-to-back Schottky diodes with two basic metallization geometries, planar and interdigitated. (Fig. 1) The most extensively evaluated set of detectors used Ni electrodes on a Si substrate with an SiO<sub>2</sub> dielectric isolation layer. The Ni pads are connected to chrome-gold bonding pads.(Fig. 2) The detector is then mounted in a high-speed microstrip waveguide package designed for a 50- $\Omega$  transmission impedance.(Fig. 3) Additional detectors were fabricated on GaAs to investigate any substrate material dependence.

### E. Dissertation Contents Summary

In the next chapter, a detailed theoretical model, starting from basic principles, is derived. This model incorporates diffusion, recombination, charge carrier drift, beam position, and beam intensity distribution across the detector. This model is the most rigorous and detailed analytical treatment of the msm photodiode frequency response available and is a significant extension of previous models.<sup>37,40,49,50</sup> This model is extensively compared to data in the 5 to 10-GHz frequency range to avoid the low-frequency gain region previously mentioned.

The data was collected using the calibrated uv heterodyne system described in detail in Chapter III. The hardware and calibration procedures are discussed extensively. Also presented are the alignment procedures and some initial results on day-to-day reproducibility.

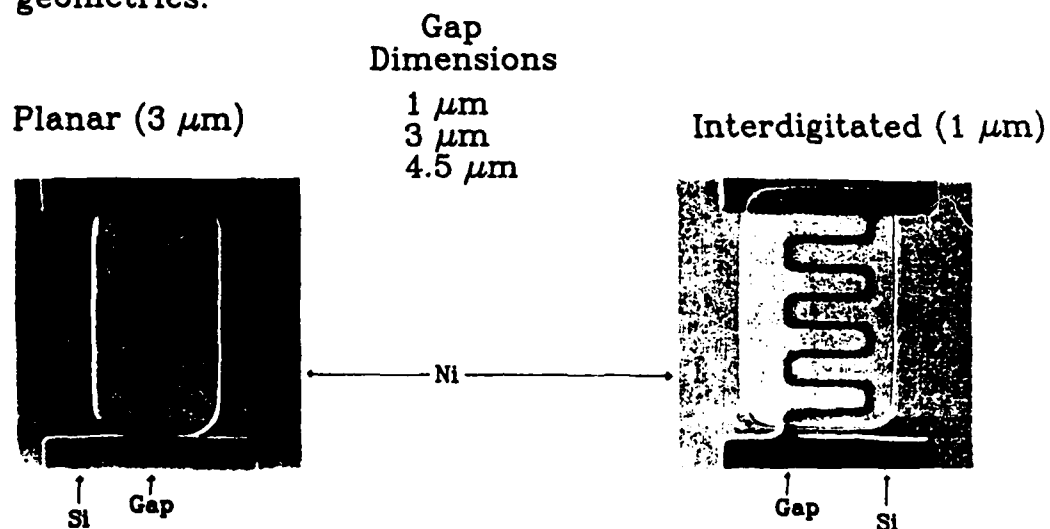
Chapter IV presents the detailed results of tests performed on several detectors. It is shown that the rf package used to mount the detector was the limiting high-frequency component in the system. The standard wire bonding technique used in the package presents a series inductance. This small inductance results in a simple L/R circuit response that was found to be the predominant effect in the high-frequency response data. This limited the comparison of data to theory. However, the L/R response could not account for changes in the response curves with respect to bias and beam position. A combination of the theoretical model and the L/R circuit response was able to fit the high-frequency data quite adequately. An extension of the frequency response data to 18 GHz is shown for one detector. It is shown that a 4.5- $\mu\text{m}$  gap detector, with a properly designed rf package, with a 21-GHz bandwidth

and a 30% rf quantum efficiency, can be fabricated on bulk Si which is in agreement with the detector model in Chapter II. The model predicts that a 1.0- $\mu\text{m}$  gap detector would have a 75-GHz bandwidth. The comparison of the model with data indicates that charge transport near the surface of Si is identical to transport in the bulk.

Finally, the low-frequency gain of these detectors has been investigated. A correlation of the bandwidth and gain with bias and beam position is made for this low-frequency behavior.

Figure 1: MSM detector geometries.

All are Ni-on-Si, metal-semiconductor-metal (M-S-M) back-to-back Schottky diodes with varying metallization geometries.



Planar geometry is chosen due to short absorption lengths in the uv, approx 10 nm, for semiconductors in general. Planar geometry allows direct access to the photosensitive area.

Detector pads are  $10\ \mu\text{m} \times 20\ \mu\text{m}$  with  $75\ \mu\text{m} \times 75\ \mu\text{m}$  bonding pads. Implying that RC is much less than 5.1 psec (31 GHz).

Figure 2: MSM detector construction.

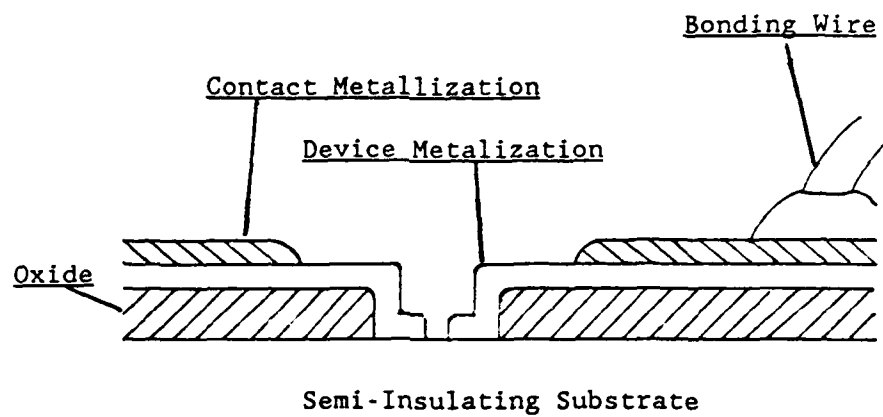
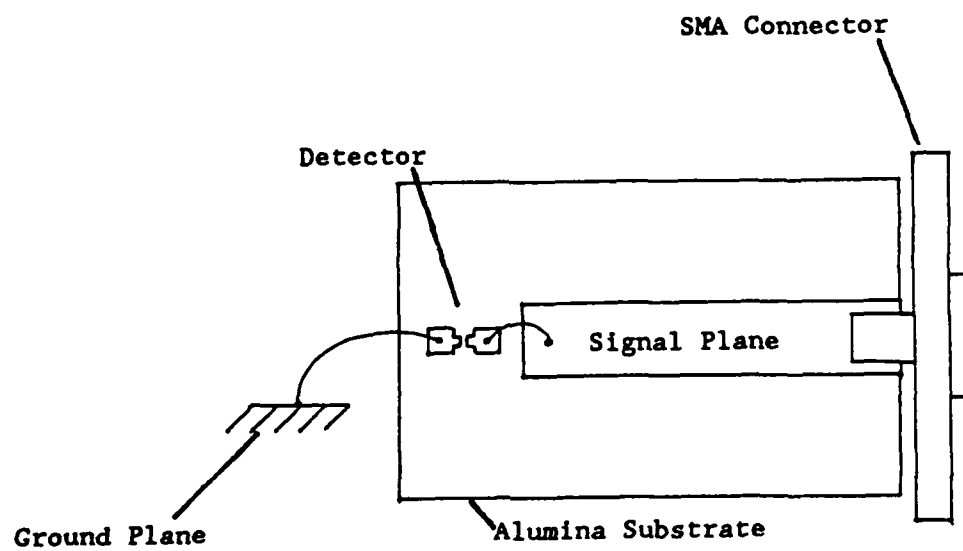


Figure 3: MSM detector mounted on microstrip waveguide package.



## References

1. D. G. McLean, M. G. Roe, A. I. D'Souza, and P. E. Wigen, "Picosecond recombination of charged carriers in GaAs", Applied Physics Letters, 48(15), 14 April 1986.
2. J. C. Campbell, W. S. Holden, G. J. Qua, and A. G. Dentai, "Frequency Response of InP/InGaAsp/InGaAs Avalanche Photodiodes with separate Absorption 'Grading' and Multiplication Regions", IEEE Journal of Quantum Electronics, Vol. QE-21, No. 11, November 1985.
3. C. Y. Chen, B. L. Kasper, H. M. Cox, J. K. Plourde, "2-Gb/s sensitivity of a  $\text{Ga}_{0.47}\text{In}_{0.53}\text{As}$  photoconductive detector/GaAs field-effect transistor hybrid photoreceiver", Applied Physics Letters, 46(4), 15 Feb. 1985.
4. Gammel, George M. Metzger, and Joseph M. Ballantine, "A Photoconductive Detector for High-Speed Fiber Communication", IEEE Transactions on Electron Devices, Vol. ED-28, No. 7, July 1981.
5. V. Diadiuk and S. H. Groves, "Lateral photodetectors on semi-insulating InGaAs and InP", Applied Physics Letters, 46(2), 15 Jan. 1985.
6. P. M. Downey and R. J. Martin, R. E. Nahory, O. G. Lorimor, "High-speed, ion bombarded InGaAs photoconductors", Applied Physics Letters, 46(4), 15 Feb. 1985.

7. M. Ito, T. Kumai, H. Hamaguchi, M. Makiuchi, K. Nakai, O. Wada, and T. Sakurai, "High-speed monolithically integrated GaAs Photoreceiver using a metal-semiconductor-metal photodiode", Applied Physics Letters, 47(11), 1 Dec. 1985.
8. W. Lenth, A. Chu, L. J. Mahoney, R. W. McClelland, R. W. Mountain, and D. J. Silversmith, "Planar GaAs p-i-n photodiode with picosecond time response", Applied Physics Letters, 46(2), 15 Jan. 1985.
9. S. Muira, H. Kuwatsuka, T. Mikawa, and O. Wada, "Planar, embedded InP/GaInAs p-i-n photodiode with very high speed response characteristics", Applied Physics Letters, 49(22), 1 Dec. 1986.
10. O. Wada, H. Hamaguchi, S. Miura, M. Makiuchi, K. Nakai, H. Horimatsu, and T. Sakurai, "AlGaAs/GaAs p-i-n photodiode/preamplifier monolithic photoreceiver integrated in a semi-insulating GaAs substrate", Applied Physics Letters, 46(10), 15 May 1985.
11. C. Y. Chen, A. G. Dental, B. L. Kasper, P. A. Garbinski, "High-speed junction-depleted  $\text{Ga}_{0.47}\text{In}_{0.53}\text{As}$  photoconductive detectors", Applied Physics Letters, 46(12), 15 June 1985.
12. Ock Ky Kim, Bulusu V. Dutt, R. J. McCoy, and John R. Zuber, "A Low Dark-Current, Planar InGaAs p-i-n Photodiode with a Quaternary InGaAsP Cap Layer", IEEE Journal of Quantum Electronics, Vol. QE-21, No. 2, Feb 1985.

13. K. Ohnaka, K. Inoue, T. Uno, K. Hasegawa, N. Hase, and H. Serizawa, "A Planar InGaAs PIN/JFET Fiber-Optic Detector", IEEE Journal of Quantum Electronics, Vol. QE-21, No. 8, Aug. 1985.
14. W. T. Tsang, J. C. Campbell, "InGaAs/InP p-i-n photodiodes grown by chemical beam epitaxy", Applied Physics Letters, 48(21), 26 May 1986.
15. C. Y. Chen, Y. M. Pang, K. Alavi, A. Y. Cho, and P. A. Garbinski, "Interdigitated  $\text{Al}_{0.48}\text{In}_{0.52}\text{As}/\text{Ga}_{0.47}\text{In}_{0.53}\text{As}$  photoconductive detectors", Applied Physics Letters, Vol. 44, No. 1, 1 Jan. 1984.
16. L. Figueroa and C. W. Slayman, "A Novel Heterostructure Interdigital Photodetector (HIP) with Picosecond Optical Response", IEEE Electron Device Letters, Vol. EDL-2, No. 8, Aug. 1981.
17. C. W. Slayman and L. Figueroa, "Frequency and Pulse Response of a Novel High Speed Interdigital Surface Photoconductor (IDPC)", IEEE Electron Device Letters, Vol. EDL-2, No. 5, May 1981.
18. T. Sugeta, T. Urisu, S. Sakata, and Y. Mizushima, "Metal-Semiconductor-Metal Photodetector for High-Speed Optoelectronic Circuits", Japanese Journal of Applied Physics, Vol. 19, Supp. 19-1, 1980.

19. Y. K. Jhee, J. C. Campbell, W. S. Holden, A. G. Dentai, and J. K. Flourde, "The Effect of Nonuniform Gain on the Multiplication Noise of InP/InGaAsP/InGaAs Avalanche Photodiodes", IEEE Journal of Quantum Electronics, Vol. QE-21, No. 12, Dec. 1985.
20. M. Rezeghi, J. Ramdani, H. Verrielle, D. Decoster, M. Constant, and J. Vanbremeersch, "Planar monolithic integrated photoreceiver for 1.3-1.55  $\mu\text{m}$  wavelength applications using GaInAs-GaAs heteroepitaxies", Applied Physics Letters, 49(4), 28 July 1986.
21. H. Temkin, A. Antreasyan, N. A. Olsson, T. P. Pearsall, and J. C. Bean, " $\text{Ge}_{0.6}\text{Si}_{0.4}$  rib waveguide avalanche photodetectors for 1.3  $\mu\text{m}$  operation", Applied Physics Letters, 49(13), 29 Sept. 1986.
22. G. E. Bulman, D. R. Meyers, T. E. Zipperian, and L. R. Dawson, "Proton isolated  $\text{In}_{0.2}\text{Ga}_{0.8}\text{As}$ /GaAs strained-layer superlattice avalanche photodiode", Applied Physics Letters, 48(15), 14 April 1986.
23. A. Larsson and A. Yariv, "Spectral and temporal characteristics of AlGaAs/GaAs superlattice p-i-n photodetectors", Applied Physics Letters, 47(8), 15 Oct. 1985.
24. B. F. Levine, R. J. Malik, C. G. Bethea, and J. Walker, "Long wavelength GaSb photoconductive detectors grown in Si substrates", Applied Physics Letters, 48(16), 21 April 1986.

25. F. Osaka, T. Mikawa, and O. Wada, "Electron and Hole Impact Ionization Rates in InP/Ga<sub>0.47</sub>In<sub>0.53</sub>As Superlattice", IEEE Journal of Quantum Electronics, Vol. QE-22, No. 10, Oct. 1986.
26. D. G. Parker, N. R. Couch, M. J. Kelly, and T. M. Kerr, "High-speed response of a quasi-graded band-gap superlattice p-i-n photodiode", Applied Physics Letters, 49(15), 13 Oct. 1986.
27. H. Temkin, J. C. Bean, T. P. Pearsall, N. A. Olsson, and D. V. Lang, "High photoconductive gain in Ge<sub>x</sub>Si<sub>1-x</sub>/Si strained-layer superlattice detectors operating at  $\lambda = 1.3 \mu\text{m}$ ", Applied Physics Letters, 49(3), 21 July 1986.
28. C. Y. Yen, A. Y. Cho, C. G. Bethea, P. A. Garbinski, Y. M. Pang, B. F. Levine, K. Ogawa, "Ultrahigh speed modulation-doped heterostructure field-effect photodetectors", Appl. Phys. Lett., Vol. 42(12), pg 1040-1042, 15 June 1983.
29. D. K. Donald, S. Y. Wang, T. R. Ranganath, S. A. Newton, W. R. Trutna, Jr., "Photocurrent amplification in Schottky photodiodes", Appl. Phys. Lett., Vol. 49(10), pg 567-568, 8 Sept 1986.
30. O. Wada, H. Hamaguchi, L. LaBella, C. Y. Boisrobert, "Noise Characteristics of GaAs Metal-Semiconductor-Metal Photodiodes", Elec. Lett., Vol. 24, pg 1574, (1988).

31. Wingo (C.-Y.) Huang, C. Salupo, L. F. Szabo, G. P. Ceasar, W. Javurek, "A new type of stable and sensitive uv detector fabricated with amorphous silicon based alloys", MRS Spring Meeting, Reno, April 5-9, 1988.
32. Henrik Fabricius, Torben Skettrup, and Paul Bisgaard, "Ultraviolet detectors in thin sputtered ZnO films", Applied Optics, Vol. 25, No. 16, 15 Aug. 1986.
33. R. B. Hammond, N. G. Paulter, R. S. Wagner, "Observed circuit limits to time resolution in correlation measurements with Si-on-sapphire, GaAs, and InP picosecond photoconductors", Appl. Phys. Lett., Vol. 45, pg 289, (1984).
34. Ghavam G. Shahidi, E. P. Ippen, J. Melngailis, "Submicron-gap high-mobility silicon picosecond photodetectors", Appl. Phys. Lett., Vol. 46, pg 719-721, (1985).
35. R. B. Hammond, N. G. Paulter, R. S. Wagner, W. R. Eisenstadt, "Integrated picosecond photoconductors produced on bulk Si substrates", Appl. Phys. Lett., Vol. 45(4), pg 404-405, 15 Aug 1984.
36. H. Blauvelt, G. Thurmond, J. Parsons, D. Lewis, H. Yen, "Fabrication and characterization of GaAs Schottky barrier photodetectors for microwave fiber optic links", Appl. Phys. Lett., Vol. 45(3), pg 195-196, 1 Aug 1984.

37. R. J. Seymour, B. K. Garside, "Ultrafast silicon interdigital photodiodes for ultraviolet applications", Can. J. Phys., Vol 63, pg 707-711, 1985.
38. R. Loepfe, A. Schaelin, H. Melchior, M. Blaser, H. Jaeckel, G. L. Bona, "2 ps InGaAs photoconductors and their speed-of-response evaluation by optical pulse mixing at inherent nonlinearities", Appl. Phys. Lett., Vol. 52(25), pg 2130-2132, 20 June 1988.
39. M. Ito, O. Wada, "Low Dark Current GaAs Metal-Semiconductor-Metal (MSM) Photodiodes Using  $WSi_x$  Contacts", IEEE Journ. of Quan. Elec., Vol. QE-22, No. 7, pg. 1073-1077, 1986.
40. B. K. Garside, R. E. Park, and R. Seymour, "On picosecond optical detection", SPIE, Vol. 533, 1985.
41. H. Ouchi, T. Mukai, T. Kamei, and M. Okamura, "Silicon p-n Junction Photodiodes Sensitive to Ultraviolet Radiation", IEEE Transactions on Electron Devices, Vol. ED-26, No. 12, Dec. 1979.
42. Suwat Thaniyavarn, T. K. Gustafson, "Metal/tunnel-barrier/semiconductor/tunnel-barrier/metal fast photodetector", Appl. Phys. Lett., Vol. 40(3), pg 255-257, 1 Feb 1982.

43. R. S. Tucker, A. J. Taylor, C. A. Burrus, G. Eisenstein, J. M. Wiesenfeld, "Coaxially Mounted 67 GHz Bandwidth InGaAs Pin Photodiode", Appl. Phys. Lett., 14 July 1986.
44. S. Y. Wang and D. M. Bloom, Elec. Lett., Vol 19, pg. 554, (1983).
45. S. Y. Wang, D. M. Bloom, and D. M. Collins, Appl. Phys. Lett., Vol. 42, pg. 190, (1983).
46. K. L. Sala, G. A. Kenny-Wallace, and G. E. Hall, IEEE Journ. Quantum Electron., QE-16, 990 (1980).
47. T. F. Carruthers and J. F. Weller, "Picosecond optical mixing in fast photodetectors", Applied Physics Letters, 48(7), 17 Feb. 1986.
48. S. Kawanishi, M. Saruwatari, "Wideband frequency response measurement of photodetectors using optical heterodyne detection technique", Electronics Letters, Vol. 22, No. 6, 13 Mar 1986.
49. D. Marcuse, " Electrostatic field of coplanar lines computed with the point matching method", IEEE Journ. of Quan. Elec., Vol. 25, No. 5, pg. 939, (1989).
50. R. L. Peterson, " Numerical studies of currents and fields in a photconductive detector", IEEE Journ. of Quan. Elec., Vol. QE-23, pg. 1185, (1987).

51. S. Ramo and J. R. Whinnery, Fields and Waves in Modern Radio, John Wiley and Sons, Inc., (1944).

52. S. F. Soares, Ultraviolet Heterodyne Photodetectors, Ph.D Dissertation, Dept. of Elec. Eng, Univ. of NM, (1989).

## Chapter II

### Theory

#### A. Introduction

In this chapter the theory of heterodyne detection is presented. The theory of heterodyne, or coherent, detection for an ideal photodetector is reviewed, as is the theory of charge transport in a metal-semiconductor-metal diode. Under the assumption that the drift velocities of the charge carriers are constant in a metal-semiconductor-metal diode, the current in the external circuit is derived for both an impulse and a constant frequency heterodyne source. It is also shown that these two results are just a Fourier transform pair, as expected. If a detector's frequency response is transit time limited by the carrier's drift velocity across the semiconductor gap, then the upper-bound frequency response is the gap dimension divided by the drift velocity. For a 4.5, 3.0 and 1.0  $\mu\text{m}$  gap detector and a drift velocity of  $10^7$  cm/sec, the upper bound frequency response is 3.5, 5.3, and 16 GHz, respectively, by this simple transit time argument. A more rigorous model presented in this chapter predicts that the bandwidths for the 4.5, 3.0 and 1.0- $\mu\text{m}$  gap detectors are 21, 31 and 75 GHz, respectively. Finally, rf-packaging limitations are discussed and some theoretical predictions of detector performance are made.

#### B. Heterodyne Signal

Heterodyne detection at optical frequencies was first achieved by Forrester, et al<sup>1</sup>, in 1955. A rigorous quantum mechanical treatment of heterodyne detection was derived by Teich<sup>2</sup> in 1969. More recently, the

theory of heterodyne detection has been reviewed by Kingston<sup>3</sup>. The development presented here will closely follow that of Kingston with some additional detail presented.

A heterodyne system consists of a signal source and a local oscillator, denoted by subscripts S and LO, respectively. Standard heterodyne systems are set up such that the local oscillator power,  $P_{LO}$ , is much greater than the signal power,  $P_S$ . By driving the detector with a sufficiently high  $P_{LO}$  the shot noise in the detector becomes significant. The shot noise power,  $N_{SHOT}$ , resulting from the dc photocurrent produced by the local oscillator,  $i_{LO}$ , in a semiconductor photodiode is given by<sup>3</sup>

$$N_{SHOT} = 4Rqi_{LO}B \quad (\text{Watts}) \quad (1)$$

where B is the bandwidth of the sampling electronics, and R is the 50-ohm termination resistor of the electronics. The shot noise is the noise source arising from the discreteness of the charge in the current. These discrete charges obey Poisson statistics and the shot noise power is given by the above equation. Given a 1-MHz bandwidth and a 1-mA photocurrent, then  $N_{SHOT}$  is -75 dbm. The thermal noise power,  $N_{TH}$ , from this detector is<sup>3</sup>

$$N_{TH} = kTB \quad (2)$$

where k is Boltzman's constant, and T is the temperature of the detector in degrees Kelvin. Thermal noise, as used here, is the noise source arising from the thermal excitement of free charges inside of a resistor. At room temperature, the thermal noise for a 1-MHz bandwidth

is -114 dbm. The magnitude of  $i_{LO}$  needed for the shot noise to equal the thermal noise is approximately 249  $\mu$ A. Hence, by driving the detector hard enough with the local oscillator, the system noise can be dominated by the shot noise. Thus, the current,  $i_{LO}$ , must be known and is now derived.

Start by considering the two  $\mathbf{E}$ -fields incident upon the detector;

$$\begin{aligned} \mathbf{E}_{LO}(x,y,t) &= \text{Re}(\mathbf{E}_{LO}(x,y)\exp[i\omega_{LO}t]), \text{ and} \\ \mathbf{E}_S(x,y,t) &= \text{Re}(\mathbf{E}_S(x,y)\exp[i\omega_S t]). \end{aligned} \quad (3)$$

The total field,  $\mathbf{E}_T$ , incident upon the detector is

$$\mathbf{E}_T(x,y,t) = \mathbf{E}_{LO}(x,y,t) + \mathbf{E}_S(x,y,t) \quad (4)$$

and the differential injection current,  $di$ , produced by this field in the detector is

$$di = \frac{q\eta c \epsilon_0}{\hbar\omega_{LO}} \left| \text{Re}(\mathbf{E}_{LO}(x,y)\exp[i\omega_{LO}t] + \mathbf{E}_S(x,y)\exp[i\omega_S t]) \right|^2 dx dy \quad (5)$$

where  $\eta$  is the detector quantum efficiency,  $q$  the unit of charge,  $\epsilon_0$  the dielectric constant of free space, and  $c$  the speed of light. Assuming  $\omega_S \approx \omega_{LO}$ , then  $\hbar\omega_{LO}$  is a good approximation for the energy per photon for either the signal or local oscillator beams. Evaluating  $di$  gives

$$di = \frac{q\eta \epsilon_0 c}{\hbar\omega_{LO}} ( |\mathbf{E}_{LO}|^2 \cos^2(\omega_{LO}t) + |\mathbf{E}_S|^2 \cos^2(\omega_S t) + 2\mathbf{E}_{LO} \cdot \mathbf{E}_S \cos(\omega_{LO}t)\cos(\omega_S t) ) dx dy \quad (6)$$

which can be written as

$$\begin{aligned}
 di = \frac{q\eta\epsilon_0 c}{\hbar\omega_{LO}} & \left( \frac{1}{2} |\mathbf{E}_{LO}|^2 [1 + \cos(2\omega_{LO}t)] + \right. \\
 & \frac{1}{2} |\mathbf{E}_S|^2 [1 + \cos(2\omega_S t)] + \\
 & \left. \mathbf{E}_{LO} \cdot \mathbf{E}_S [\cos((\omega_{LO} + \omega_S)t) + \right. \\
 & \left. \cos((\omega_{LO} - \omega_S)t)] \right) dx dy
 \end{aligned}
 \tag{7}$$

Several terms in the above equation can now be identified. The  $\frac{1}{2}E^2$  terms are the differential d.c. photocurrents,  $di_{LO}$  and  $di_S$ , due to the local oscillator and signal, respectively. The two  $\cos(2\omega t)$  terms and the  $\cos((\omega_{LO} + \omega_S)t)$  term are at twice the optical frequency,  $\approx 2 \times 10^{15}$  Hz for uv light, well above the frequency response of the detector and can be ignored. The remaining  $\cos(\Delta\omega t)$  term,  $\Delta\omega = \omega_{LO} - \omega_S$ , is the heterodyne signal. By tuning  $\omega_S$  to be close to  $\omega_{LO}$ , a radio frequency differential injection current,  $di_{RF}$ , is introduced in the detector and,

$$\begin{aligned}
 di = \frac{q\eta\epsilon_0 c}{\hbar\omega_{LO}} & \left( \frac{1}{2} |\mathbf{E}_{LO}|^2 + \frac{1}{2} |\mathbf{E}_S|^2 + \right. \\
 & \left. \mathbf{E}_{LO} \cdot \mathbf{E}_S \cos(\Delta\omega t) \right) dx dy
 \end{aligned}
 \tag{8}$$

Now the power in either of the beams is

$$P = \frac{1}{2} \epsilon_0 c \iint_{-\infty}^{+\infty} |\mathbf{E}(x,y)|^2 dx dy
 \tag{9}$$

and the total injection current in the detector, assuming that  $\eta$  is not a function of  $x$  and  $y$  ( $\eta \neq f(x,y)$ ), and that the detector collects all of the incident beam, is,

$$i = \int di = \frac{q\eta}{\hbar\omega_{LO}} \left[ \frac{1}{2}\epsilon_0 c \iint_{-\infty}^{+\infty} [|\mathbf{E}_{LO}|^2 + |\mathbf{E}_S|^2] dx dy + c\epsilon_0 \cos(\Delta\omega t) \iint_{-\infty}^{+\infty} \mathbf{E}_{LO} \cdot \mathbf{E}_S dx dy \right] \quad (10)$$

which becomes

$$i = \frac{q\eta}{\hbar\omega_{LO}} \left[ (P_{LO} + P_S) + c\epsilon_0 \cos(\Delta\omega t) \iint_{-\infty}^{+\infty} \mathbf{E}_{LO} \cdot \mathbf{E}_S dx dy \right] \quad (11)$$

The first term is just the dc injection photocurrent; hence, the dc quantum efficiency is

$$\eta_{DC} = \frac{i_{DC}}{(P_{LO} + P_S)} \cdot \frac{\hbar\omega_{LO}}{q} \approx \frac{i_{DC}}{P_{LO}} \cdot \frac{\hbar\omega_{LO}}{q} \quad (12)$$

assuming that  $P_{LO} \gg P_S$ . The radio frequency heterodyne injection current,  $i_{RF}$ , is

$$i_{RF} = \frac{q\eta\epsilon_0 c}{\hbar\omega_{LO}} \cos(\Delta\omega t) \iint_{-\infty}^{+\infty} \mathbf{E}_{LO} \cdot \mathbf{E}_S dx dy. \quad (13)$$

Note that  $i_{RF}$  is proportional to  $\mathbf{E}_{LO} \cdot \mathbf{E}_S$ , demonstrating that the "mixing" of the two beams is important. It is important to note here, that present models equate the injection current with the current in the external circuit, which is not true in general. Carrier diffusion and recombination, along with beam position and intensity profile, will in general reduce the current in the external circuit while the injection current remains constant. These effects will be discussed in great detail later in this chapter. Nevertheless, continuing with Kingston's approach, multiply the square of  $i_{RF}$  by unity to get

$$i_{RF}^2 = \frac{q^2 n^2}{h^2 \omega_{LO}^2} c \epsilon_0 \cos^2(\Delta\omega t) \times$$

$$\left[ \frac{\left| \iint_{-\infty}^{+\infty} \mathbf{E}_{LO} \cdot \mathbf{E}_S \, dx dy \right|^2}{\iint_{-\infty}^{+\infty} |\mathbf{E}_{LO}|^2 \, dx dy \iint_{-\infty}^{+\infty} |\mathbf{E}_S|^2 \, dx dy} \iint_{-\infty}^{+\infty} |\mathbf{E}_{LO}|^2 \, dx dy \iint_{-\infty}^{+\infty} |\mathbf{E}_S|^2 \, dx dy \right]$$

(14)

The mixing efficiency,  $m$ , is defined as

$$m = \frac{\left| \iint_{-\infty}^{+\infty} \mathbf{E}_{LO} \cdot \mathbf{E}_S \, dx dy \right|^2}{\iint_{-\infty}^{+\infty} |\mathbf{E}_{LO}|^2 \, dx dy \iint_{-\infty}^{+\infty} |\mathbf{E}_S|^2 \, dx dy}$$

(15)

which is, provided  $\eta_{RF} = f(x,y)$ , identical to Kingston's expression for the mixing efficiency<sup>3</sup>. Thus, Eqn 13, can be written as

$$i_{RF}^2 = \frac{4q^2\eta_{RF}^2}{(\hbar\omega_{LO})^2} \cos^2(\Delta\omega t) \cdot m \cdot P_{LO}P_S \quad (16)$$

Now, the rf-spectrum analyzer, used in these experimental measurements, actually measures the rf power. Under the assumption that the injection current is equal to the external circuit current, the rf power,  $P_{RF}$ , is given by

$$P_{RF} = \overline{i_{RF}^2} \cdot R_{SA} \quad (17)$$

where  $R_{SA}$  is the 50- $\Omega$  input impedance of the spectrum analyzer. The time average rf injection current is given by

$$\overline{i_{RF}^2} = \frac{4q^2\eta_{RF}^2}{(\hbar\omega_{LO})^2} \cdot \frac{m \cdot P_{LO}P_S\Delta\omega}{2\pi} \int_0^{2\pi/\Delta\omega} \cos^2(\Delta\omega t) dt \quad (18)$$

and

$$\left[ \overline{i_{RF}^2} \right]^{1/2} = \frac{q\eta_{RF}}{\hbar\omega_{LO}} \cdot [2mP_{LO}P_S]^{1/2} \quad (19)$$

and if  $m \approx 1$ , then

$$\eta_{RF} = \frac{\left[ \frac{1}{i_{RF}^2} \right]^{1/2}}{[2P_{LO}P_S]^{1/2}} \cdot \frac{\hbar\omega_{LO}}{q} \quad (20)$$

Having derived the rf-quantum efficiency, the mixing efficiency,  $m$ , is now considered. The denominator of  $m$  can easily be reduced to  $4P_{LO}P_S/c^2\epsilon_o^2$ , giving for Eqn 15

$$m = \frac{c^2\epsilon_o^2 \left| \iint_{-\infty}^{+\infty} \mathbf{E}_{LO} \cdot \mathbf{E}_S \, dx dy \right|^2}{4P_{LO}P_S} \quad (21)$$

Now, assume two Gaussian beams of equal beam widths,  $w$ , comprising the local oscillator and signal beams. The x-y plane is chosen to correspond to the surface of the detector and the local oscillator beam is normally incident upon the surface. The signal beam is tilted with respect to the local oscillator beam with the axis of rotation being about the y-axis (Fig 4). The local oscillator is travelling along the z-axis and the signal beam is traveling along the z'-axis, and  $\theta$  is the angle of tilt between the two directions of propagation. Writing down  $\mathbf{E}_{LO}$  and  $\mathbf{E}_S$  for the described geometry one finds

$$\begin{aligned} \mathbf{E}_{LO} &= \text{Re}(\mathbf{E}_{LO} \cdot \exp[-(x^2+y^2)/w^2] \cdot \exp[i(zk_{LO} - \omega_{LO}t)]) \cdot \mathbf{i}' \\ \mathbf{E}_S &= \text{Re}(\mathbf{E}_S \cdot \exp[-(x'^2+y'^2)/w^2] \cdot \exp[i(z'k_S - \omega_S t)]) \cdot \mathbf{i}' \end{aligned} \quad (22)$$

Then rotating the primed into the unprimed coordinates by<sup>8</sup>

$$\begin{aligned}x' &= x \cos \theta + z \sin \theta \\y' &= y \\z' &= -x \sin \theta + z \cos \theta\end{aligned}\tag{23}$$

one obtains, combining Eqns 22 and 23:

$$\begin{aligned}\mathbf{E}_{LO} \cdot \mathbf{E}_S &= E_{LO} E_S \cos \theta \exp[-2y^2/w^2] \exp[-x^2(1+\cos^2\theta)/w^2] \times \\&\quad \cos(k_S x \sin \theta + \Delta \omega t)\end{aligned}\tag{24}$$

which, integrated over all x and y, leads to

$$\begin{aligned}\iint_{-\infty}^{+\infty} \mathbf{E}_{LO} \cdot \mathbf{E}_S \, dx dy = \\E_{LO} E_S \frac{\pi w^2 / 2 \cos \theta}{4 [1 + \cos^2 \theta]^{1/2}} \exp \left[ \frac{-k_S^2 w^2 \sin^2 \theta}{4(1 + \cos^2 \theta)} \right] \cos(\Delta \omega t)\end{aligned}\tag{25}$$

which leads to an expression for m as

$$m = \frac{2 \cos^2 \theta}{[1 + \cos^2 \theta]} \exp \left[ \frac{-k_S^2 w^2 \sin^2 \theta}{2(1 + \cos^2 \theta)} \right]\tag{26}$$

The dominant term in the above expression for small  $\theta$  is the exponential. Its argument clearly shows that the relationship between the wavelength, beam spotsize, and tilt is very important. Plots of m versus tilt are shown in Figure 5 for three different spotsizes. Note the change in

scale of the tilt axis as the spotsize increases. This is because the amount of tilt needed for a  $\pi$  phase shift between the two beams is less with a larger spot, than with a smaller one. If an experiment could always be performed with a small spotsize, then the tilt in the beam would not be of great consequence. This, however, is impractical and minimizing the amount of tilt as much as possible is desired and beam alignment is of paramount importance. The mixing efficiency at a given tilt is tabulated in Table 1 for a  $100 \mu\text{m}$   $e^{-2}$  radius beam. The tilt of  $3345 \mu\text{rad}$  corresponds to the value of the wavelength divided by the spotsize. This amount of tilt produces a  $2\pi$  phase shift across the beam radius, and the integrated rf power at the detector is nearly zero.

The signal-to-noise ratio of a heterodyne measurement is now considered. The heterodyne signal power is given in Eqn 18 and can be written as

$$\overline{i_{\text{RF}}^2} = \frac{2q^2 \eta_{\text{RF}}^2}{(\hbar\omega_{\text{LO}})^2} \cdot m \cdot P_{\text{LO}} P_{\text{S}} \quad (27)$$

The shot noise from a semiconductor photodiode has been given above as

$$\overline{i_{\text{N}}^2} = 4qi_{\text{LO}}B \quad (28)$$

where  $B$  is the bandwidth of the sampling electronics and  $i_{\text{LO}}$  is the d.c. photocurrent out of the detector, given by

$$i_{\text{LO}} = \eta_{\text{DC}} P_{\text{LO}} \cdot (q/\hbar\omega_{\text{LO}}) \quad (29)$$

It is assumed that the shot noise is the predominant noise source. It has been shown above that  $P_{\text{LO}}$  can be increased until the shot noise due

to the local oscillator dominates all other noise sources. At this point, it is assumed that the dc quantum efficiency of the detector is not equal to the rf quantum efficiency. Then, the power signal-to-noise ratio, S/N, is given by

$$S/N = \frac{\overline{i_{RF}^2}}{i_N^2} = \frac{2q^2 \eta_{RF}^2 m P_{LO} P_S}{4\hbar^2 \omega^2 q i_{DC} B} \quad (30)$$

then from Eqn 29

$$S/N = \frac{m \eta_{RF}^2 P_S}{2 \eta_{DC} B \hbar \omega_{LO}} \quad (31)$$

For a typical bandwidth of 10 GHz, and  $\hbar \omega_{LO} = 5.94 \times 10^{-19}$  J ( $\lambda = 334.5$  nm), then for an unity signal to noise ratio and assuming  $\eta_{DC} = \eta_{RF} = m = 1$ ,  $P_S$  must be 12 nW. Reducing the bandwidth to 1 MHz, a signal power of 1.2 pW will be sufficient to produce a unity signal-to-noise ratio. Contrast this with direct detection operation that is thermal or Johnson noise limited. Johnson noise arises from the fluctuation in the resistivity of the terminating resistor of the electronics due to thermal heating. Johnson noise is related, but not identical to thermal noise. For an unity signal-to-noise ratio the above beam would need 3.4  $\mu$ W of incident power in the case of a thermal noise limit. This assumes a kTB = -74 dbm thermal noise source (300 K and a 10 GHz bandwidth). If the detector is Johnson noise limited, then 68 nW of signal power is needed for a unity signal-to-noise ratio. Clearly, the heterodyne detection will give a very large signal-to-noise ratio for even a microwatt of signal beam power on the detector.

Thus it has been shown that, with good mutual beam alignment, there will be a sinusoidal photocurrent superimposed on top of the dc photocurrent in a heterodyne detection experiment. The dc and rf quantum efficiencies have been derived and lastly it has been shown that heterodyne measurements can give a very large signal-to-noise ratio for a small signal power.

### C. Metal-Semiconductor-Metal Photodiode

Having derived the source term for charge carriers, the photodiode structure used to detect the light signal is now considered.

At uv wavelengths, the absorption depth in all semiconductors is approximately  $10 \text{ nm}^4$ . Hence, for high speed and maximum responsivity, the photodetective area must be directly illuminated by the uv light. This obviates the use of a p-i-n structure, since all of the incident uv radiation would be absorbed in the top layer, and not in the intrinsic region required for operation of the p-i-n detector. Hence, a p-i-n device is diffusion limited as a result of the short absorption depth of the ultraviolet light in the top layer.

A very simple photodiode that has the depletion region on the surface of the semiconductor is a metal-semiconductor-metal back-to-back Schottky diode. Two parallel metal pads of equal dimension and composition are deposited on the surface of a semiconductor. A gap region between the pads allows for direct illumination of the semiconductor, making up the photodiode. The doping for the diodes used in this study is n-type with a concentration of approximately  $10^{14} \text{ cm}^{-3}$ .

The basic theory of the metal-semiconductor-metal, msm, diode has been developed by Sze et al<sup>5</sup> for plane parallel metal pads sandwiching the semiconductor. This geometry is somewhat different than the detector design used in this study. However, it will be shown in the next section that the difference between the two designs can be made negligible.

Sze has calculated depletion widths, conduction and valence band curvatures, and leakage currents as a function of bias voltage, electrode spacing, temperature, and doping density. This section will review the parts of Sze's msm theory that pertain to high-speed heterodyne detection. At the heart of the basic operation of any photodiode is the transport of carriers inside the semiconductor. For high-speed detection, the predominant transport mechanism is drift under the influence of an externally applied field. To understand carrier drift velocities, it is necessary to consider the conduction and valence band structure of a simple, vertical-geometry msm diode (Fig. 6). Figure 7 shows the msm band structure for a n-type semiconductor at three bias conditions.

Figure 7a is the unbiased case. At thermal equilibrium the Fermi levels of the metal and semiconductor must be equal. If there were no defect states at the metal-semiconductor interface then the band structure near the interface would be controlled by the work functions of the metal and the semiconductor. However, the existence of surface defect states in materials such as GaAs causes the Fermi level to be at mid-gap at the interface. This causes free carriers in the semiconductor to move in order that the Fermi levels coincide at the interface, thus the semiconductor bands bend near the surface. This

band bending produces a built-in field near the interface. Away from the interface, the free carriers do not have to move as much as they do at the interface and the semiconductor bands return to their normal bulk levels. One interesting point should be noticed. In the flat central region the flow of carriers is entirely by diffusion. If a point source of light is incident upon the detector near the center of the device, the charge carriers will diffuse radially and symmetrically outward. If the point source is at the exact center of the device, then the net current in both directions is equal and no external current will be measured. Displacing the point source from the center, however, causes more charge to be flowing on one side of the device than the other producing a net current in the external circuit. Hence, these devices might prove to be a sensitive position sensor.

Figure 7b shows the band structure at what Sze calls the "reach-through" voltage,  $V_{RT}$ . Simply,  $V_{RT}$  is the minimum bias at which the semiconductor is fully depleted. A semiconductor is defined to be fully depleted when all of the free carriers have been swept out and the charge in the semiconductor is just due to ionized-impurity atoms. Even though the gap between the electrodes is fully depleted at  $V_{RT}$ , the band structure shows that the electrons in the conduction band will reach a minimum energy prior to being collected by the positive electrode. This is not a desirable condition for high-speed operation of a photodiode since carriers at the energy minimum move only by diffusion.

Increasing the applied voltage further, the diode finally reaches the "flat-band" voltage,  $V_{FB}$ , shown in Figure 7c. The "flat-band" voltage is defined by Sze as the minimum bias at which the depletion region due to the cathode reaches across the gap region to the anode.

At this point, the minimum energy in the charge carriers is located at the metal-semiconductor interface. If the bias is increased further, the amount of curvature in the bands will decrease, implying a more uniform drift velocity of the charge carriers between the electrodes. Therefore, it is easily seen that the minimum bias across the detector for high-speed photodetection is the "flat-band" voltage. Using Gauss' Law, an expression can easily be derived for  $V_{FB}$  as<sup>5</sup>

$$V_{FB} = \frac{qN_D L^2}{2\epsilon_s} \quad (32)$$

where  $q$  is the unit of charge,  $N_D$  is the doping density of the semiconductor,  $\epsilon_s$  is the permittivity of the semiconductor, and  $L$  is the gap distance between electrodes. For Si doped at  $2 \times 10^{14} \text{ cm}^{-3}$ , and electrode spacings of 1.0, 3.0 and 4.5  $\mu\text{m}$ , the flat-band voltages are 0.16, 1.44, and 3.24 Volts, respectively.

The maximum voltage that can be applied to the detector is ultimately limited by the dielectric breakdown voltage of the semiconductor. However, long before dielectric breakdown is reached, the applied field will be strong enough to cause avalanche breakdown, a carrier multiplication process which drastically increases the noise and degrades the high-frequency response of the detector. For Si, the onset of avalanche breakdown occurs at  $E \geq 10^5 \text{ V/cm}$ . The point of highest field is at the negatively biased electrode<sup>5</sup>. The magnitude of the field at this point,  $E_{m1}$ , is given by<sup>5</sup>

$$E_{m1} = \frac{V + V_{FB}}{L} \quad (33)$$

where  $V$  is the actual applied bias. Setting  $E_{m1} = 10^5$  V/cm, the maximum bias, without causing avalanche breakdown, for a  $4.5\text{-}\mu\text{m}$  gap is  $\approx 42$  V. The maximum biases for the  $3.0$  and  $1.0$  micron gap devices are  $28.6$  and  $9.84$  Volts, respectively. The minimum electric field occurs at the anode, and has the strength  $E_{m2}$  given by<sup>5</sup>,

$$E_{m2} = \frac{|V - V_{FB}|}{L} \quad (34)$$

With the values of the electric field at the two metal pads, Poisson's equation can be solved for the electric field,  $E(x)$ , as a function of  $x$ , and is given by

$$E(x) = \frac{V_{FB}}{L} \left[ 1 - \frac{2x}{L} \right] + \frac{V}{L} \quad (35)$$

for plane parallel electrodes sandwiching the fully depleted semiconductor, which is a much simpler case than the msm geometry used in this study.

From this equation one can see that the electric field seen by an electron, or hole, in an msm diode, is not constant between the electrodes. The drift velocity,  $v_d$ , is directly proportional to the electric field by

$$v_d = \mu E \quad (36)$$

where  $\mu$  is the carrier mobility. However,  $\mu$  is a constant only at low fields, and  $v_d$  becomes a sublinear function of field strength for

increasingly higher fields, eventually saturating at  $10^7$  cm/sec in Si.<sup>4</sup> As a result of this saturation behavior of the drift velocity, at sufficiently high fields, the drift velocity changes very little across the MSM structure. At  $V \geq 2V_{FB}$ , the change in  $v_d$  across the diode is  $\leq 20\%$  from the average drift velocity calculated for the average electric field. This percentage decreases with increasing bias. Therefore, for high biases,  $V \geq 3V_{FB}$ , the change in the drift velocity of the charge carriers across the diode is negligible.

The final consideration for the MSM photodiode is the leakage, or dark current. Sze shows that the dark current of these devices, at room temperature, is limited by thermionic emission<sup>4,5</sup> and static barrier lowering<sup>4</sup> due to the formation of image forces when the detector is biased. In direct detection, the dark current is of primary importance in determining the minimum detectable power. Soares deals extensively with the dark current behavior of these devices in his dissertation<sup>6</sup>. For heterodyne detection, however, the dark current is of little importance if the dc photocurrent, produced by the local oscillator, is much greater than the dark current. The rationale is that the local oscillator drives the detector hard enough, such that the shot noise arising from the dc photocurrent is the predominant noise source. Hence, the dark current is of little consequence in heterodyne detection, as long as it is much less than the shot noise from the dc photocurrent produced by the local oscillator.

#### D. Electric fields due to coplanar pads.

In the previous section, a simplified band structure model for a msm photodiode was calculated for  $V_A \geq V \geq 2V_{FB}$ , where  $V_A$  is the voltage at which avalanche breakdown starts. The results were that, within this range of  $V$ , the electric field across the detector can be modeled as an average field with a strength of  $V/L$ . The drift velocity of the carriers will only vary by  $\approx 20\%$ , or less, from that calculated for the actual field. However, the model for this diode has the metal pads parallel to each other. The diode structure studied here has the metal pads coplanar with each other, a slightly different geometry. In order for the arguments of the preceding section to be valid, it must now be shown that, at least within the total carrier penetration depth in the semiconductor, the fields due to the coplanar pads are nearly identical to that of the parallel geometry. Here the total carrier penetration depth is not related to the optical penetration depth,  $\delta$ , of uv light into the semiconductor which is very shallow. The total carrier penetration depth,  $Z_{MAX}$ , is the maximum depth into the semiconductor that a carrier could reach before being collected at a pad and is totally due to diffusion, and given by

$$Z_{MAX} = (D_1 \tau_{S1})^{1/2} \quad (37)$$

where  $D_1$  is the diffusion constant of either the electrons or holes and the sweep out time,  $\tau_{S1}$ , is the transit time of the carrier. For Si with a  $10^4$  V/cm E-field applied, the value of  $Z_{MAX}$  for a  $4.5 \mu\text{m}$  detector is  $0.16 \mu\text{m}$ .

To show that the  $\mathbf{E}$ -field near the surface is almost constant, it is only necessary to consider the fields due to the metal pads, in the absence of the semiconductor. If, in air, a nearly constant  $\mathbf{E}$ -field exists near the plane of the coplanar pads, then the boundary condition requiring tangential  $\mathbf{E}$ -fields to remain invariant across a boundary will insure that the  $\mathbf{E}$ -field in the semiconductor will be the same as for the parallel pads. Therefore, the preceding arguments about band structure will remain valid.

First, consider two metal pads of semi-infinite length, as shown in Figure 8. A potential difference of  $2V$  is applied to the pads. This is a Dirichlet boundary value problem and a solution for  $\mathbf{E}(x,y,z)$  can be found by using Green's theorem. To solve this problem one only needs to know the value of  $\phi(x,y)$ , the potential, in the plane of the electrodes. This two dimensional problem can be attempted by employing the Schwartz-Christoffel transformation. The solution to this transform, however, results in an elliptical integral of the third kind, which does not have an analytical inverse. Attempts at indentifying variations on the geometry to be transformed, by employing symmetry arguments to reduce the complexity of the transform, did not produce any usable results. Any transform that still retained at least one  $90^\circ$  corner and one infinite ground plane, as shown in Figure 9, always resulted in a transformation with a non-analytical inverse. Hence, one is left with either a numerical solution to the problem, or further simplification of the geometry by using the solution for two plane parallel strips (Fig 10). The basic construction of the detectors tested is such that the width of the metal pads is much greater than the gap dimension implying that the approximation of parallel, infinite

strips should be adequate. The potential for this structure has been previously calculated<sup>9,10</sup>, as

$$\phi(x,z) = \begin{cases} \frac{2V}{\pi} \text{Arcsin}(u) - V ; & x > 0 \\ V - \frac{2V}{\pi} \text{Arcsin}(u) ; & x < 0 \end{cases} \quad (38a)$$

where

$$u = \frac{1}{x_g/2} \left( x_g^2 - x^2 - z^2 + \left[ (x_g^2 - x^2 - z^2)^2 + 4x_g^2 z^2 \right]^{1/2} \right)^{1/2} . \quad (38b)$$

and where  $2x_g$  is the gap dimension, and  $z$  is the distance into the semiconductor. Then

$$\mathbf{E} = -\vec{\nabla} \phi(x,z) = \frac{\pm \vec{\nabla} u}{(1 - u^2)^{1/2}} \quad (39)$$

where the  $\pm$  refers to  $\pm x$  as the point of interest. From Eqn 39, the value of the electric field can be calculated for any point in space. This can then be compared to the value of the electric field for plane parallel electrodes, separated by a distance of  $2x_g$ . The percentage change from the surface value of the  $\mathbf{E}$ -field strength for a 4.5- $\mu\text{m}$  wide gap with a 7-V bias across the gap is listed in Table 2. From Table 2, it is clearly seen that, at least to a depth of 2  $\mu\text{m}$  into the semiconductor, the strength of the  $\mathbf{E}$ -field is nearly constant. Couple

this result with the saturation behavior of the charge carriers at high fields and the net effect is that the variation of the drift velocity due to changes in the electric field can be ignored. Hence, in this region the drift velocity of the charge carriers can be assumed to be constant across the detector gap.

#### E. Detector photocurrent in an msm photodiode

The preceding two sections have established that the charge carriers will move with a constant drift velocity across the gap of a planar-geometry msm photodiode under sufficiently high biases. With this approximation, the photocurrent seen in the external circuit is now derived for several cases.

First consider a single photon producing a single electron-hole pair in the semiconductor region of an msm photodiode. The photodiode is biased to a level such that the drift velocities of the charge carriers are approximately constant across the depletion region. Using the geometry in Fig 10, the photon is incident at  $x_0$ . The distance that the electron and hole travel to their respective electrodes is  $x_G - x_0$ , and  $x_G + x_0$ . The current produced in the external circuit is shown in Fig 11, where the electron-hole pair is produced at  $t = t_0$  and recombination of the minority carrier is ignored. The electron, being the faster of the two carriers, is assumed to arrive at the positive electrode first at  $t = t_1$ . The slower hole arrives at the negative electrode at  $t = t_2$ . The transit times of the carriers are related to

the carrier velocities simply by

$$t_1 - t_0 = \frac{x_G - x_0}{v_n} \quad (40)$$

$$t_2 - t_0 = \frac{x_G + x_0}{v_p}$$

were  $v_n$  and  $v_p$  are the magnitudes of the electron and hole drift velocity, respectively. The current,  $i$ , in the detector can be written as

$$i(x_0, t) = \frac{q}{2} \left[ \frac{v_n}{(x_G - x_0)} [\theta(t - t_0) - \theta(t - t_1)] + \frac{v_p}{(x_G + x_0)} [\theta(t - t_0) - \theta(t - t_2)] \right] \quad (41)$$

where  $\theta$  is the unit step function. The measurements for this study, however, are made in the frequency domain, hence, taking the Fourier transform of  $i(x_0, t)$

$$i(x_0, \omega) = \frac{1}{(2\pi)^{1/2}} \int_{-\infty}^{+\infty} dt i(x_0, t) \exp(-i\omega t) \quad (42)$$

one gets, by letting  $t_0 = 0$

$$i(x_0, \omega) = \frac{iq}{2\omega} \left[ \frac{v_n}{(x_G - x_0)} \left[ \exp \left[ -i\omega \frac{x_G - x_0}{v_n} \right] \right] - 1 \right] + \left[ \frac{v_p}{(x_G + x_0)} \left[ \exp \left[ -i\omega \frac{x_G + x_0}{v_p} \right] \right] - 1 \right]$$

(43)

and finally taking the real part of  $i(x_0, \omega)$ , one gets the current in the external circuit as

$$i(x_0, \omega) = q \left[ \operatorname{sinc} \left[ \frac{\omega(x_G - x_0)}{2v_n} \right] + \operatorname{sinc} \left[ \frac{\omega(x_G + x_0)}{2v_p} \right] + \left[ \operatorname{sinc} \left[ \frac{\omega(x_G - x_0)}{2v_n} \right] \cdot \operatorname{sinc} \left[ \frac{\omega(x_G + x_0)}{2v_p} \right] \times \cos \left[ \frac{\omega(x_G - x_0)}{2v_n} - \frac{\omega(x_G + x_0)}{2v_p} \right] \right]$$

(44)

where  $\text{sinc}(x) = \sin(x)/x$ . This expression is the predicted current as a function of frequency derived from the Fourier transform of an impulse response. Note that the power into the detector has been set to one photon per second causing the factor of  $P/\hbar\omega_{LO}$  to be equal to unity with units of  $\text{sec}^{-1}$ . Comparison with Equation 19 allows some terms to be defined. The heterodyne power,  $(2P_{LO}P_S)^{1/2}$ , is the power stated above that is set equal to one photon per second. The mixing efficiency is assumed to be unity, leaving only the rf quantum efficiency,  $\eta_{RF}$ . The sinc terms comprise the rf quantum efficiency as a function of frequency. It is seen that the assumption in section B of the dc and rf quantum efficiencies were not equal being correct.

It is experimental measurements of this impulse response that dominate present high-speed detector research. It also is the predominant modeling scheme, with the frequency response being derived as the Fourier transform of this idealized impulse response.<sup>1,11</sup>

The external current from a true heterodyne source incident on the msm photodiode is now derived. Starting with the equation of continuity

$$\vec{\nabla} \cdot \mathbf{J}_p + \frac{\partial \rho_p}{\partial t} = G_p \quad (45)$$

where  $\mathbf{J}_p$ ,  $\rho_p$ , and  $G_p$  are the hole current density, hole charge density, and hole generation rate, respectively. The generation rate is given in Eqn 19 as

$$G_p = \frac{qnP}{\hbar\omega_{LO}} e^{i\omega t} \delta(x - x_0) \delta(y) \delta(z) \quad (46)$$

where  $P$  is the net heterodyne power of the light source

( $P = (\eta \cdot 2 \cdot P_{LO} P_s)^{1/2}$ ),  $\eta$  the quantum efficiency of the detector,  $\hbar\omega_{LO}$  the energy per photon, and  $\delta(x-x_0)\delta(y)\delta(z)$  places a point source of light on the surface of the semiconductor at  $x = x_0$ . Also, the hole current density and charge density are given by

$$\begin{aligned} \mathbf{J}_p &= q\mathbf{v}_p \\ \rho_p &= qp \end{aligned} \quad (47)$$

where  $\mathbf{v}_p$  is the hole drift velocity and  $p$  is the hole number density.

Assuming that  $\mathbf{v}_p = iv_p$ , then Eqn 45 becomes, after combining Eqns 46 and 47,

$$\frac{\partial}{\partial x} p + \frac{1}{v_p} \frac{\partial}{\partial t} p = \frac{nP}{v_p \hbar\omega_{LO}} e^{i\omega t} \delta(x-x_0)\delta(y)\delta(z) \quad (48)$$

Now, given an  $e^{i\omega t}$  source term it is assumed that

$$p = X(x) e^{i\omega t} \quad (49)$$

thus Eqn 48 becomes

$$\frac{\partial}{\partial x} X(x) + \frac{i\omega}{v_p} X(x) = \frac{nP}{v_p \hbar\omega_{LO}} \delta(x-x_0)\delta(y)\delta(z) \quad (50)$$

Then, a solution to this differential equation is

$$p = \frac{\eta P \theta(x-x_0)}{4\pi v_p \hbar\omega_{LO}} \exp \left[ \frac{-i\omega(x+x_0)}{v_p} + i\omega t \right] \delta(y)\delta(z) \quad (51)$$

And the hole current density inside of the semiconductor is

$$\mathbf{J}_p = \frac{iq\eta P\theta(x-x_0)}{4\pi\hbar\omega_{L0}} \exp\left[\frac{-i\omega(x+x_0)}{v_p} + i\omega t\right] \delta(y)\delta(z) . \quad (52)$$

Now to obtain the hole current in the external circuit,  $i_p(x_0, \omega, t)$ , one must integrate  $\mathbf{J}_p$  as follows

$$i_p(x_0, \omega, t) = \frac{1}{(x_G + x_0)} \int_{-\infty}^{+\infty} dy \int_{-\infty}^0 dz \int_{-x_G}^{+x_G} dx \mathbf{J}_p \cdot \mathbf{i} . \quad (53)$$

Remember, in one dimension the current density is equal to the current. Then, the current in the external circuit from a MSM photodiode, which acts like a capacitor, is the spatial average of the current between the electrodes. This is the photovoltaic effect. Contrast this to the photoconductive detector where it is the actual passage of charge that is measured. Thus, the current in the external circuit is equal to the current at any point inside of the detector. More on these differences is presented in Appendix A. The MSM devices are photovoltaic detectors.

Carrying out the integral and simplifying one arrives at the complex current due to the movement of holes in the semiconductor of the

msm photodiode, which is

$$i_p(x_0, \omega, t) = \frac{q\eta P}{\pi\hbar\omega_{10}} \exp\left[\frac{-i\omega(x_G + x_0)}{2v_p} + i\omega t\right] \times$$

$$\text{sinc}\left[\frac{\omega(x_G + x_0)}{2v_p}\right].$$

(54)

Likewise, the complex current in the external circuit due to electron flow is

$$i_n(x_0, \omega, t) = \frac{q\eta P}{\pi\hbar\omega_{10}} \exp\left[\frac{-i\omega(x_G - x_0)}{2v_n} + i\omega t\right] \times$$

$$\text{sinc}\left[\frac{\omega(x_G - x_0)}{2v_n}\right].$$

(55)

Then the total current seen in the external circuit is the sum of the electron and hole current. The current detected by most instruments will be the rms of the real part of the complex current, which is the average of the magnitude of the two complex currents, given by

equations 54 and 55, which is

$$i_{\text{RMS}} = \frac{q\eta P}{\hbar\omega_{\text{LO}}} \left[ \text{sinc} \left[ \frac{\omega(x_{\text{G}} - x_0)}{2v_{\text{n}}} \right] + \text{sinc} \left[ \frac{\omega(x_{\text{G}} + x_0)}{2v_{\text{p}}} \right] + \right. \\ \left. \left[ \text{sinc} \left[ \frac{\omega(x_{\text{G}} - x_0)}{2v_{\text{n}}} \right] \cdot \text{sinc} \left[ \frac{\omega(x_{\text{G}} + x_0)}{2v_{\text{p}}} \right] \times \right. \right. \\ \left. \left. \cos \left[ \frac{\omega(x_{\text{G}} - x_0)}{2v_{\text{n}}} - \frac{\omega(x_{\text{G}} + x_0)}{2v_{\text{p}}} \right] \right] \right] .$$

(56)

The above equation is identical to Eqn 44, which is the current from a single photon in the time domain, when  $\eta = 1$  and  $P =$  one photon per second, as is the case for a single photon generating a single electron-hole pair. Therefore, the current from a modulated source of light, as in a heterodyne experiment, does transform to the current measured in an impulse-type measurement, as expected.

The above calculations were derived assuming that the effects of carrier diffusion were negligible. However, due to the short absorption lengths of uv-wavelength radiation in any semiconductor, diffusion will play an important role in the response of these detectors. That is, with an absorption length of only 10 nm for  $\hbar\omega_{\text{LO}} \geq 3.3$  eV, the carrier

density near the surface will be very high. Since the diffusion current goes as the gradient of the charge density, then the high concentration of carriers at the surface under illumination will generate a substantial diffusion current normal to the semiconductor surface and to the applied fields.

The current in the external circuit, due to a heterodyne point source with diffusion and recombination included, is now derived. The derivation will then be generalized to an extended source with a Gaussian envelope.

Again, start by assuming a point source illumination with an  $e^{i\omega t}$  time variation in intensity, this time located at the origin. Generalization to a source not at the origin will be made by a coordinate translation later. Neglecting the d.c. terms of the heterodyne signal, the source term for the holes,  $G_p$ , in the semiconductor is given by

$$G_p = \frac{q\eta P}{\hbar\omega_{LO}} e^{i\omega t} \delta(x)\delta(y)\delta(z) \quad (57)$$

Then the equation of continuity is given by

$$\vec{\nabla} \cdot \mathbf{J}_p + \frac{\partial \rho_p}{\partial t} = G_p - R_p \quad (58)$$

where  $R_p$  is the recombination rate of the holes, given by

$$R_p = \frac{qP}{\tau} \quad (59)$$

where  $p$  is the number density of holes in an n-type semiconductor, and  $\tau$  is the effective recombination lifetime of the holes. The current and charge density can be written as

$$\begin{aligned} \mathbf{J}_p &= q\mathbf{v}_p - qD_p \vec{\nabla} p \\ \rho_p &= qp \end{aligned} \quad (60)$$

where  $D_p$  is the diffusion constant for the holes. It has previously been shown that the drift velocity for carriers in the semiconductor of an MSM diode structure is very nearly constant. Hence, assuming a constant drift velocity for the carriers, then Eqns 57 through 60 give

$$\mathbf{v}_p \cdot \vec{\nabla} p - D_p \vec{\nabla}^2 p + \frac{\partial p}{\partial t} + \frac{p}{\tau} = \frac{\eta P}{\hbar\omega_{LO}} e^{i\omega t} \delta(\mathbf{r}) \quad (61)$$

where

$$\delta(\mathbf{r}) = \delta(x)\delta(y)\delta(z) . \quad (61a)$$

The linearity of the differential equation with respect to time implies that the time variation of  $p$  will follow the source term. Also, the coordinate system is oriented such that  $\mathbf{v}_p$  is along the x axis only.

Hence, Eqn 61 reduces to

$$\vec{\nabla}^2 p_0 - \frac{v_p}{D_p} \frac{\partial p_0}{\partial x} - \left[ \frac{1}{D_p \tau} + \frac{i\omega}{D_p} \right] p_0 = \frac{-\eta P}{D_p \hbar\omega_{LO}} \delta(\mathbf{r}) \quad (62)$$

where

$$p = p_0 e^{i\omega t} \quad (62a)$$

Now in the limiting case of the drift velocity going to zero, i.e. no bias on the detector, the solution for  $p_0$  is

$$p_0(v_p=0) = A' \left[ \frac{\pi}{2u'} \right]^{1/2} \cdot I_{1/2}(u') + B' \left[ \frac{\pi}{2u'} \right]^{1/2} \cdot K_{1/2}(u') \quad (63a)$$

with

$$u' = \left[ (x^2 + y^2 + z^2) \left[ \frac{1}{D_p r} + \frac{i\omega}{D_p} \right] \right]^{1/2} \quad (63b)$$

and  $I_{1/2}$  and  $K_{1/2}$  are the modified spherical Bessel functions of the first and third kind, respectively. Under the boundary conditions that  $p_0$  goes to zero at infinity and  $p_0 = \infty$  at the origin, it is found that  $A' = 0$ , hence

$$p_0(v_p=0) = B' \left[ \frac{\pi}{2u'} \right]^{1/2} \cdot K_{1/2}(u') \quad (64)$$

which reduces to<sup>7</sup>

$$p_o = B' \left[ \frac{\pi}{2} \right]^{1/2} \cdot \frac{e^{-u'}}{u'} \quad (65)$$

Then substituting Eqn 65 back into the differential equation (Eqn 62), one can solve for B getting

$$B' = \frac{\eta P}{4\pi D_p \hbar \omega_{LO}} \left[ \frac{1}{D_p \tau} + \frac{i\omega}{D_p} \right]^{1/2} \quad (66)$$

The charge density for the zero bias case is then

$$p_o = \frac{\eta P}{4\pi D_p \hbar \omega_{LO}} \left[ \frac{1}{D_p \tau} + \frac{i\omega}{D_p} \right]^{1/2} \cdot \frac{e^{-u'}}{u'} e^{i\omega t} \quad (67)$$

Now, apply a bias across the detector and  $v_p \neq 0$ . Using the transform  $p = p' e^{ax} e^{i\omega t}$ , Eqn 61 reduces to an identical equation in  $p'$  as that of the zero drift velocity case with slightly different coefficients.

Hence, with drift velocity included,  $p$  becomes

$$p = \frac{\eta P}{4\pi D_p \hbar \omega_{LO}} \left[ \frac{1}{D_p \tau} + \frac{i\omega}{D_p} \right]^{1/2} \times \exp \left[ \frac{v_p x}{2D_p} - S \right] \frac{e^{i\omega t}}{S} \quad (68a)$$

where

$$S = \left[ (x^2 + y^2 + z^2) \left[ \frac{v_p^2}{4D_p^2} + \frac{1}{D_p \tau} + \frac{i\omega}{D_p} \right] \right]^{1/2} \quad (68b)$$

and now

$$B = \frac{\eta P}{4\pi D_p \hbar \omega_{LO}} \left[ \frac{v_p^2}{4D_p^2} + \frac{1}{D_p \tau} + \frac{i\omega}{D_p} \right]^{1/2} \quad (68c)$$

which reduces to the zero bias case when  $v_p = 0$ . Now, the complex hole current at any given point inside of the semiconductor,  $i_p'$ , is given by

$$i_p' = q \int_{-\infty}^{+\infty} dy \int_0^{+\infty} dz \mathbf{n} \cdot (\mathbf{v}_p p - D_p \vec{\nabla} p) \quad (69)$$

The above integrals can be carried out with a few simple steps. First, remember that the drift velocity is in the  $x$  direction only, therefore

$n = i$ , which simplifies Eqn 69 to

$$i_p' = q \int_{-\infty}^{+\infty} dy \int_0^{+\infty} dz \left[ v_p p(x, y, z) - D_p \frac{\partial}{\partial x} p(x, y, z) \right]. \quad (70)$$

Next, given the symmetry of  $p$ , change the variables to a cylindrical geometry by letting  $r^2 = y^2 + z^2$ , thus giving,

$$i_p' = qB \int_0^{+\infty} r dr \int_0^{\pi} d\theta \left[ v_p \frac{\exp(\alpha x - [(x^2+r^2)(\alpha^2+\beta^2)]^{1/2})}{[(x^2+r^2)(\alpha^2+\beta^2)]^{1/2}} - D_p \frac{\partial \exp(\alpha x - [(x^2+r^2)(\alpha^2+\beta^2)]^{1/2})}{\partial x [(x^2+r^2)(\alpha^2+\beta^2)]^{1/2}} \right]. \quad (71a)$$

where

$$\alpha = \frac{v_p}{2D_p} \quad ; \quad \beta^2 = \frac{1}{D_p \tau} + \frac{i\omega}{D_p} \quad (71b)$$

The partial with respect to  $x$  is now allowed to operate on the  $e^{\alpha x}$  term,

and Eqn 71 can be rewritten as,

$$i_p' = \pi q B (1 + \alpha) v_p \exp(\alpha x) \times$$

$$\int_0^{+\infty} r dr \frac{\exp(-[(x^2 + r^2)(\alpha^2 + \beta^2)]^{1/2})}{[(x^2 + r^2)(\alpha^2 + \beta^2)]^{1/2}} -$$

$$\pi q B D_p \exp(\alpha \omega) \int_0^{+\infty} r dr \frac{\partial \exp(-[(x^2 + r^2)(\alpha^2 + \beta^2)]^{1/2})}{\partial x [(x^2 + r^2)(\alpha^2 + \beta^2)]^{1/2}} .$$

(72)

The first integral is easily solved by making the transformation  $u^2 = x^2 + r^2$ . Notice that the partial derivative in the second integral only operates on the combination of  $(x^2 + r^2)$ . This allows the substitution of  $\partial/\partial x = (x/r)\partial/\partial r$  and the second integral can be written as,

$$\int_0^{+\infty} r dr \frac{x}{r} \frac{\partial \exp(-[(x^2 + r^2)(\alpha^2 + \beta^2)]^{1/2})}{\partial r [(x^2 + r^2)(\alpha^2 + \beta^2)]^{1/2}}$$

(73)

which can easily be solved by integration by parts. With the above steps,  $i_p'$  can be found and the current seen in the external circuit,  $i_p$ , by the motion of the holes is given by

$$i_p = \text{Re} \left[ \frac{1}{x_G - x_0} \int_{-x_G}^{+x_G} dx i_p'(x - x_0, t) \right]$$

(74)

where the location of the source has been translated from  $x = 0$  to  $x = x_0$ , and the spacing between the electrodes is  $2x_G$ . Hence, the total external complex current, due only to holes, is

$$i_p = B \frac{v_p + 2D_p[\alpha_p^2 + \beta_p^2]^{1/2}}{\alpha_p^2 + \beta_p^2} \times \frac{\exp[(x_G - x_0)(\alpha_p - [\alpha_p^2 + \beta_p^2]^{1/2})] - 1}{(x_G - x_0)(\alpha_p - [\alpha_p^2 + \beta_p^2]^{1/2})} \quad (75a)$$

where

$$\alpha_p = \frac{v_p}{2D_p} \quad ; \quad \beta_p^2 = \frac{1}{D_p \tau} + \frac{i\omega}{D_p} \quad (75b)$$

Similarly, the external complex current due to the electrons is

$$i_n = B \frac{v_n + 2D_n[\alpha_n^2 + \beta_n^2]^{1/2}}{\alpha_n^2 + \beta_n^2} \times \frac{\exp[(x_G + x_0)(\alpha_n - [\alpha_n^2 + \beta_n^2]^{1/2})] - 1}{(x_G + x_0)(\alpha_n - [\alpha_n^2 + \beta_n^2]^{1/2})} \quad (76a)$$

with

$$\alpha_n = \frac{v_n}{2D_n} \quad ; \quad \beta_n^2 = \frac{i\omega}{D_n} \quad (76b)$$

where  $v_n$  and  $D_n$  are the electron drift speed and diffusion constant, respectively. Note that the  $\beta_n$  term is missing the  $1/D\tau$  term that is in the  $\beta_p$  term. This is because the electrons are quickly separated from

the holes by the applied electric field. Hence, in n-type material the electrons can not recombine, yet the holes still can recombine with electrons in the material. For silicon, the  $1/D\tau$  term is insignificant, since both  $\beta_n$  and  $\beta_p$  are dominated by the  $v^2/4D^2$  and  $i\omega/D$  terms, both on the order of  $10^8$ , while the  $1/D\tau$  term is on the order of  $10^2$ .

The instrument utilized to measure the photocurrent is a radio-frequency spectrum analyzer, which measures the real total rms current at its input terminal. The expression in Eqns. 75a and 76a are the complex currents which cannot easily be expressed as real and imaginary parts. Therefore, let the time independent part of the current be expressed as  $a + ib$ , then the current is

$$i = \text{Re}((a + ib)(\cos(\omega t) + i\sin(\omega t))) \quad (77)$$

which becomes

$$i = a\cos(\omega t) - b\sin(\omega t) \quad (78)$$

Taking the time average of the square of the current gives

$$\overline{i^2} = \frac{\omega}{2\pi} \int_0^{2\pi/\omega} dt ( a^2\cos^2(\omega t) + b^2\sin^2(\omega t) - 2a'b'\cos(\omega t)\sin(\omega t) ) \quad (79)$$

The  $\cos^2(\omega t)$  and  $\sin^2(\omega t)$  terms give a factor of  $1/2$  for the integral, while the  $\cos(\omega t)\sin(\omega t)$  term integrates to zero giving

$$\overline{i^2} = (a^2 + b^2)/2 \quad (80)$$

Thus the real total rms current,  $i_{\text{RMS}}$ , is given by

$$i_{\text{RMS}} = (\overline{i^2})^{1/2} = \frac{|i_n + i_p|}{\sqrt{2}} \quad (81)$$

where  $i_p$  and  $i_n$  are the complex time independent portion of the complex currents given in Equations 75a and 76a, respectively.

The entire preceding calculation was with an assumed point source of charge with a sinusoidal time variation. In reality, the beam is nearly Gaussian and of significant finite extent relative to the gap dimension. To account for the effects of an extended source, consider equations 75a, 76a, and 78. These equations describe the current in the external circuit, due to a point source at position  $x_0$ , and  $i_{\text{RMS}}$  is a function of  $x_0$  only. Hence, the effects of the extended source in  $y$  and  $z$  are just a constant. To include the effect of an extended source upon the external current, assume a Gaussian shaped beam with a  $e^{-2}$  radius,  $w$ . Then the current in the circuit from this beam,  $i_{\text{EXT}}$ , is

$$i_{\text{EXT}} = \frac{\sqrt{2}}{w/\pi} \int_{-x_G}^{+x_G} dx' i_{\text{RMS}}(x') \exp \left[ -2(x_0 - x')^2/w^2 \right] \quad (82)$$

This current,  $i_{\text{EXT}}$ , is calculated numerically taking 0.1-lm steps and summing the weighted individual point source currents at each step.

The current in the external circuit, given by Equations 75a, 76a, and 78, were derived under a constant  $\mathbf{E}$ , or flatband, approximation. There is one other potential source of band bending in these detectors that has not been considered, that is, a space charge

effect due to photogenerated carriers. With no illumination, and  $V \geq 2V_{FB}$ , the semiconductor is fully depleted and the band curvature is negligible. By illuminating the surface with a light source, another source of charge is created inside the semiconductor. Under the influence of the applied electric field, the photogenerated electron-hole pairs separate, creating an opposing dipole  $\mathbf{E}$ -field to the applied  $\mathbf{E}$ -field. Given sufficiently high charge densities, this dipole field could significantly change the carrier drift velocities in the semiconductor. Consider the charge density given by Eqn 68c. Setting  $t = 0$ , one finds that the maximum charge density per second in the semiconductor is given by

$$\frac{p}{t} \approx \frac{\eta P}{4\pi D_p \hbar \omega_{LO}} \left[ \frac{v_p^2}{4D_p^2} + \frac{1}{D_p \tau} \right]^{1/2} \quad (\text{C/cm}^3 \cdot \text{sec}) \quad (68c)$$

This expression gives the charge density generated per second by the incident light. However, the charges do not stay around to collect, but move away from the light source under the influence of the applied bias. For a drift velocity of  $10^7$  cm/sec, an incident beam power of 1 mW, the value for  $p/tq$  is  $1.39 \times 10^{18} \text{ cm}^{-3}\text{sec}^{-1}$ . The transit time,  $t$ , for a charge inside the semiconductor is  $\Delta x/v$ , where  $\Delta x$  is the distance the charge has to travel. For a 4.5- $\mu\text{m}$  gap detector, this transit time is a maximum of 45 psec, for  $v = 10^7$  cm/sec. As the velocity drops, the transit time increases, hence the charge density in the semiconductor remains constant for a given incident light power. With the charge density known, the change in  $\mathbf{E}$  with respect to  $x$  is given by Gauss' Law

as

$$\frac{\Delta E_x}{\Delta x} = \frac{p}{\epsilon_s} \quad (84)$$

Given a transit time of 75 psec, corresponding to an applied Bias of  $V = V_{FB}$ , the change in  $E$  with respect to  $x$  is 16.46 V/cm<sup>2</sup>. This implies a change of 7.4 mV across the electrodes of a 4.5  $\mu$ m wide detector. Hence, it is clearly seen that even for this worst case, the effective band bending due to the photo-generated carriers is negligible, especially since a 1-mW beam is about twice the actual incident beam power upon the detector. Experimental evidence of negligible bandbending is shown in chapter 4 where the 5-10 GHz frequency response of a detector does not change with changes in  $P_{LO}$ .

#### F. Predicted Detector Performance and Limitations

The results of the derivations of the previous four sections in this chapter are now used to investigate the predicted physical limits of msm photodetectors.

First, consider the simple, non-diffusion photocurrent given by Eqn 56. Notice that the argument of every function in this equation has the same basic form of

$$\frac{\omega \Delta x_1}{2v_1} \quad (85)$$

where,  $\Delta x_1$  is the distance the charge has to travel and  $v_1$  is the average drift velocity. Noting that the transit time  $\tau_T = \Delta x_1/v_1$ , it is

clearly seen that in this very simple case that the detector will be transit-time limited.

Considering the more complete expression for the photocurrent given in Eqns 75a, 76a, and 78, the limiting physics is not as easily seen. For now, concentrate on the complex hole current given in Eqn 33. From the symmetry of the equations, any conclusions made about the limits on the hole current can then be equally applied to the electron current. Rewriting Eqn 75a, and dropping the subscripts for simplicity, gives

$$i_p = B \cdot \frac{v + 2D[(v/4D)^2 + (1/D\tau) + (i\omega/D)]^{1/2}}{[(v/4D)^2 + (1/D\tau) + (i\omega/D)]} \times$$

$$\frac{\exp((\Delta xv/2D)(1 - [1 + (4D/v^2\tau) + (i4\omega D/v^2)]^{1/2})) - 1}{((\Delta xv/2D)(1 - [1 + (4D/v^2\tau) + (i4\omega D/v^2)]^{1/2}))}$$
(86)

where  $\Delta x = x_g - x_0$ . Now, as a check, let  $D$  go to zero and  $\tau$  go to infinity. This turns off both diffusion and recombination and Eqn 86 should reduce to Eqn 56. After some algebra, Eqn 86 becomes

$$i_p \approx \frac{q\eta P}{\hbar\omega_{LO}} \cdot \frac{\exp[-i\Delta x\omega/v] - 1}{(i\Delta x\omega/v)}$$
(87)

which further reduces to

$$i_p = \frac{q\eta P}{\hbar\omega_{LO}} \exp[i\Delta x\omega/2v] \operatorname{sinc}(\Delta x\omega/2v)$$
(88)

A similar expression can be derived for the electron current. Adding the two currents and taking the real part, one then gets Eqn 56, as expected. Now, turn the diffusion and recombination back on and consider Eqn 86, written as

$$i_p = \frac{qnP}{2\hbar\omega_{LO}} \cdot \frac{1 + [1 + (4D/v^2\tau) + (i4\omega D/v^2)]^{1/2}}{[1 + (4D/v^2\tau) + (i4\omega D/v^2)]} \times$$

$$\frac{\exp\{(\Delta xv/2D)(1 - [1 + (4D/v^2\tau) + (i4\omega D/v^2)]^{1/2})\} - 1}{\{(\Delta xv/2D)(1 - [1 + (4D/v^2\tau) + (i4\omega D/v^2)]^{1/2})\}}$$

(89)

Now expand the square roots and keep the first two terms, in the small parameters of  $4D/v^2\tau$  and  $D\omega/v^2$ . For a 10-GHz beam modulation and a drift velocity of  $5 \times 10^6$  cm/sec, the upper bound for these two small terms are  $4D/v^2\tau \leq 10^{-7}$  and  $D\omega/v^2 \leq 0.10$ . The expansion gives

$$i_p = \frac{qnP}{\hbar\omega_{LO}} \cdot \frac{[1 + (D/v^2\tau) + (i\omega D/v^2)]}{[1 + (4D/v^2\tau) + (i4\omega D/v^2)]} \times$$

$$\exp\{(-i/2)[(\Delta x\omega/v\tau) + (i\Delta x/v\tau)]\} \times$$

$$\text{sinc}[(\Delta x\omega/v\tau) + (i\Delta x/v\tau)]$$

(90)

Examination of the argument of the exponential or sinc reveals some very interesting effects. First, the  $-\Delta x/v\tau$  is simply recombination of the carriers. The  $\Delta x/v$  term is just the transit time of the carrier in the diode. Hence, the current decreases as the transit time increases, or as the drift velocity (bias) decreases.

However, this is only important when the transit time starts to approach the carrier lifetime, implying that materials with high drift velocities and long carrier lifetimes will give the highest response. Also, the  $\Delta x/v\tau$  shows that the response of the detector is not uniform across the gap. This implies that there will be some optimal position on the detector. However, this position dependence will be very weak in Si, given the relatively long lifetime of the carriers.

Now consider the second term in the exponential,  $i\Delta x\omega/v$ . Again, it is seen that the transit time,  $\Delta x/v$ , is important. In this argument, however, it is the relationship between the carrier transit time and the period of the heterodyne signal that is important. Also note that for a heterodyne frequency of  $v/\Delta x$ , the exponential has the value of  $\exp(i2\pi) = 1$  and the hole current will be a minimum. However, since the electrons and holes usually have different drift velocities, while the hole current is at a minimum, the electron current will not be at a minimum. At saturation velocity, the electrons and holes do have the same speed in Si, and hence the current can be made to go to zero at 44.4 GHz, if the point source beam is placed in the center of a 4.5  $\mu\text{m}$  gap detector. This null in the current will be greatly diminished with a physical, extended source.

Another important physical parameter in detector behavior is the RC-time constant of the detector. The RC-time constant of the detectors used in this study is very small. Consider the capacitance of a plane parallel plate capacitor with plate areas equal to the largest electrode area of the detectors tested, 200  $\mu\text{m}^2$ . Separate the plates with a 1.0  $\mu\text{m}$  thick dielectric with the same permeability as Si,  $\epsilon_s = 11.9$ . Assuming a 50- $\Omega$  terminating impedance, the RC-time constant for this

circuit is 1 psec, which implies a 160-GHz bandwidth. The detectors used in this study have coplanar electrodes, not plane parallel. Hence, the actual capacitance, and time constant, of these detectors will be much less than the above case. Therefore, it is concluded that the RC-time constant is not a limiting factor in these detectors.

Thus, it has been shown that at a bias  $V > 2V_{FB}$  that the detectors are transit-time limited. The important parameters being the transit time compared to the recombination lifetime and the period of oscillation of the heterodyne signal.

Having discussed the ultimate factors limiting detectors performance, now consider the predicted performance of three Si detectors studied in this dissertation. The values for the drift velocities, diffusion constants, and recombination times are that of bulk Si.<sup>4</sup> First consider the frequency response versus  $\mathbf{E}$ -field for a 4.5, 3.0, and 1.0  $\mu\text{m}$  gap detectors. Four different electric field strengths were applied across each detector,  $1.0 \times 10^4$  V/cm,  $2.0 \times 10^4$  V/cm,  $3.3 \times 10^4$  V/cm, and  $6.6 \times 10^4$  V/cm. The necessary bias to achieve these fields, along with  $V_{FB}$ , is listed in Table 3. Figures 11, 12 and 13 show the relative responsivity,  $R(\omega)$ , versus frequency from d.c. to 100 GHz. Also shown are close-ups of the d.c. to 10 GHz and 5.0 to 10 GHz regions. All curves were normalized to unity at d.c. A  $1.7\text{-}\mu\text{m}$   $e^{-2}$  FWHM Gaussian beam, the approximate size of the actual experimental beam, at the geometric center,  $x = y = 0$ , was used as the heterodyne source. First notice that, at the highest bias, these detectors should be extremely fast. Table 4 lists the -3 db point for each detector at each  $\mathbf{E}$ -field. Also note that the  $6.6 \times 10^4$ ,  $3.3 \times 10^4$  and  $2.0 \times 10^4$  V/cm fields produce nearly identical performance on a given

detector. This implies that at higher biases, the detector performance will be only weakly dependent upon bias. This results from the saturation of the carrier drift velocities. The only appreciable change in the frequency response,  $R(\omega)$ , is seen at the lower biases. Hence, any data fits to the higher biased data will have problems discriminating between the higher fields, as seen in the 0 to 10-GHz plots. However, one should be able to see a difference at the lower biases.

Next, the electric field was set at  $2.0 \times 10^4$  V/cm and  $R(\omega)$  versus beam position is plotted in Figures 14, 15, and 16. The same beam spot parameters were used as in the previous graphs. As with the  $R(\omega)$  versus bias graphs, one sees that there is a condition where the change in  $R(\omega)$  is very slight. As the beam is moved from the center of the detector toward the cathode side, denoted by  $x > 0$ ,  $R(\omega)$  does not change significantly. Hence, by increasing the average electron transit time, and reducing the average hole transit time, very little effect is seen in  $R(\omega)$ . Yet, if the hole transit time is increased, and the electron's decreased, a notable difference is seen in the 4.5 and 3.0  $\mu\text{m}$  detectors. This implies that these detectors are mostly affected by the slower hole transport and weakly affected by the electron transport. This does not imply that it is the minority carrier that is important here, but only the least mobile. The model treats electrons and holes on an equal footing, with the only difference being the drift velocities of each carrier and the negligible difference arising from recombination in Si. Note that for the 1.0- $\mu\text{m}$  detector hardly any difference is seen in  $R(\omega)$  as a function of position. This is due to the size of the incident beam. The 1.7- $\mu\text{m}$   $e^{-2}$  FWHM beam is large enough such that the

illumination across the 1.0- $\mu\text{m}$  gap is very nearly uniform. A small beam would indeed show some change in  $R(\omega)$  versus position for the 1.0- $\mu\text{m}$  detector. But the 1.7- $\mu\text{m}$  FWHM beam is approximately the size of the incident beam used in the experiment, therefore a smaller spot size plot is not shown.

Finally, consider the entire detector package from the msm detector to the rf-spectrum analyzer. The electronics from the cable connected to the detector package, to the spectrum analyzer, used to measure the rf current, have been calibrated and their effect subtracted from the data. More on this calibration is given in the next chapter. Thus, the measurement is sensitive to the combined effects of the detector and the microwave package up to the SMA rf connector used to mate with the signal cable. The detector and microwave package, used to transmit the signal from the detector to the signal cable, has not been calibrated. Extensive work on the effect of the package on the rf current has been done by Soares<sup>3</sup> in his dissertation. Soares has concluded that the major limitation of the package is the small bonding wire leading from the detector to the rf microstrip. This small loop of wire is a small inductor which is placed in series with the detector, causing an L/R rolloff.<sup>3</sup> Soares has calculated that the inductance for a nominal bonding wire is in the 1 to 10 nH range, and R is the 50- $\Omega$  termination of the external circuit. Table 5 lists the inductance as a function of frequency for various -3 db points for a simple L/R circuit. Unfortunately, it is clearly seen that the detector performance could be limited by the inductance of the rf package.

In conclusion, a model for the frequency response characteristics has been developed for a msm photodiode under a flatband approximation.

The predicted behavior of these diodes indicates that they are transit-time limited, and more sensitive to changes in the hole transit time, than the electron transit time. However, the calculated 21-GHz bandwidth for a 4.5- $\mu\text{m}$  gap detector is much higher than the simple transit-time argument of 3.5 GHz given early in this chapter. Variations in  $R(\omega)$  can be seen for lower biases, hence slower drift velocities, and longer transit times. The relatively small changes in  $R(\omega)$  with beam position could possibly make discrimination between data sets somewhat tenuous. Likewise, the calculated change in  $R(\omega)$  with bias shows that only the low bias conditions should yield easily discriminated data.

Figure 4. Two Gaussian Beams with a Tilt  $\theta$  between them.

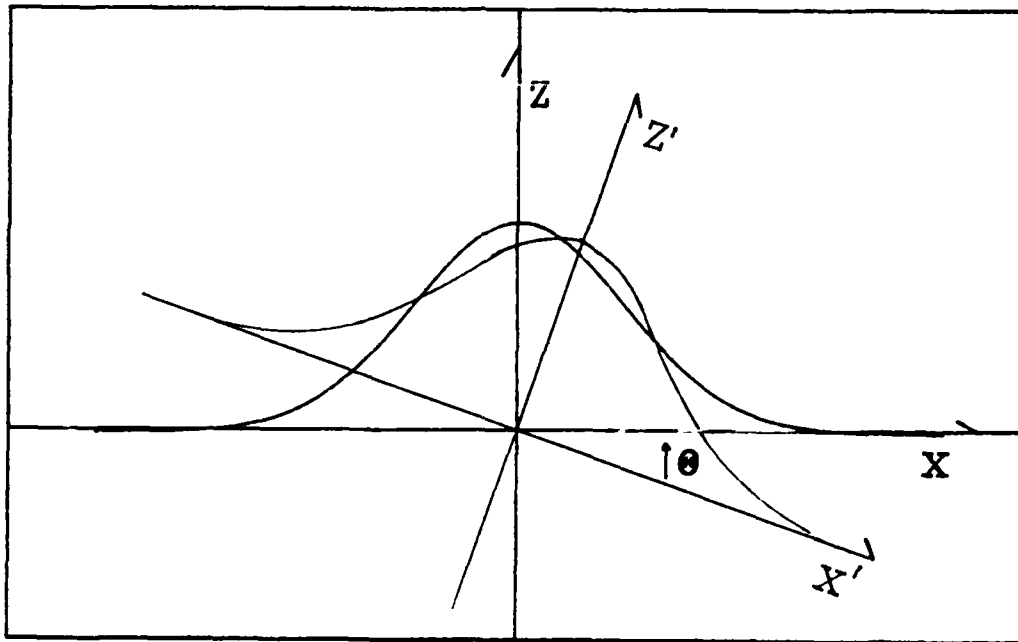


Figure 5. Mixing Efficiency versus Tilt Angle for 1.7, 10 and 100  $\mu\text{m}$  FWHM Spots.

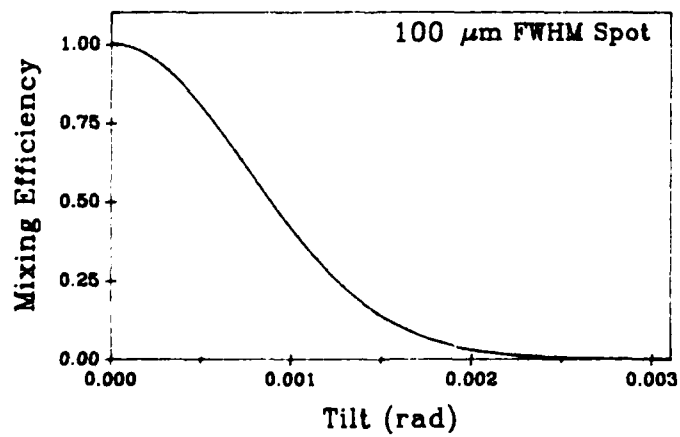
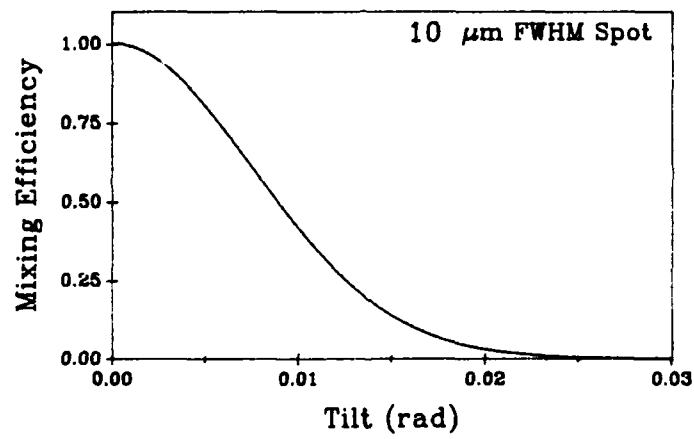
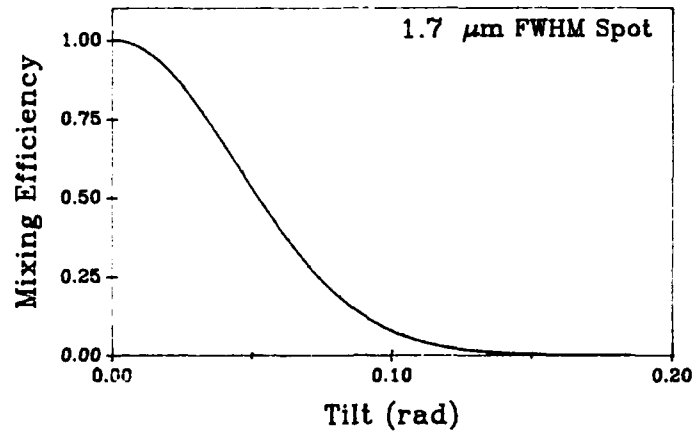
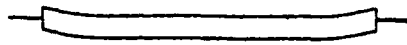


Figure 6. MSM Photodiode Band Structure versus Bias Voltage.

(a) Zero Bias



(b) Reach-Through Bias



(c) Flat-Band Bias

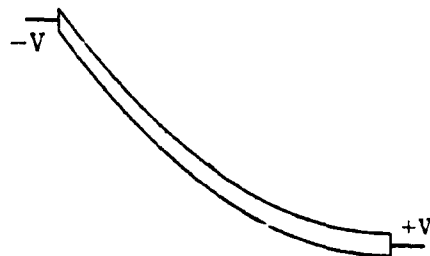
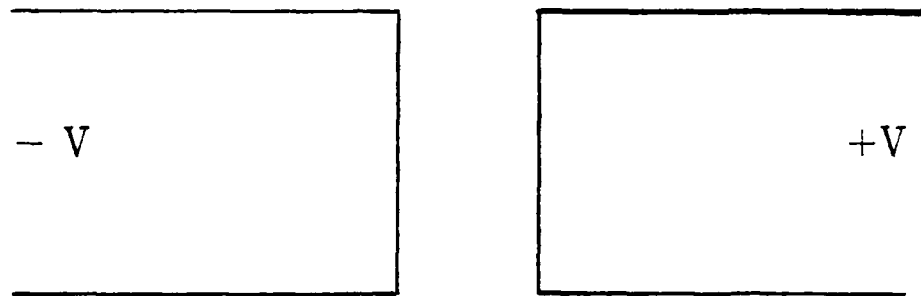


Figure 7. Simple Coplanar Geometry.

### Coplanar Metal Pads of an MSM Detector



Top View

Figure 8. Simplified Coplanar MSM Geometry.

Simplified Geometry for the Coplanar  
Metal Pads of a MSM Detector

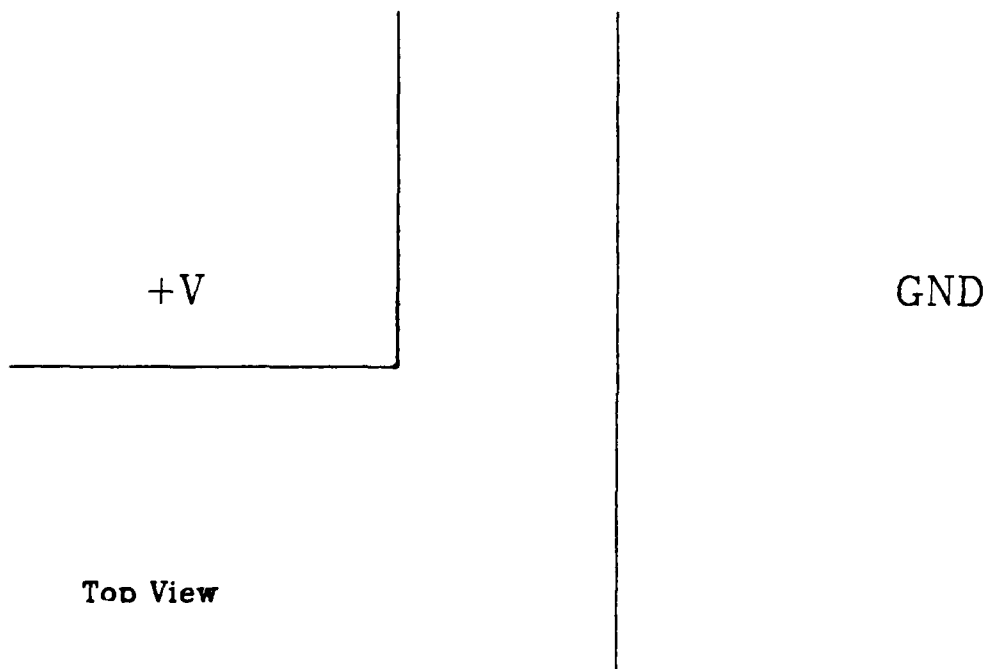


Figure 9. Semi-Infinite Coplanar Metal Pads.

## Semi-Infinite Coplanar Metal Pads

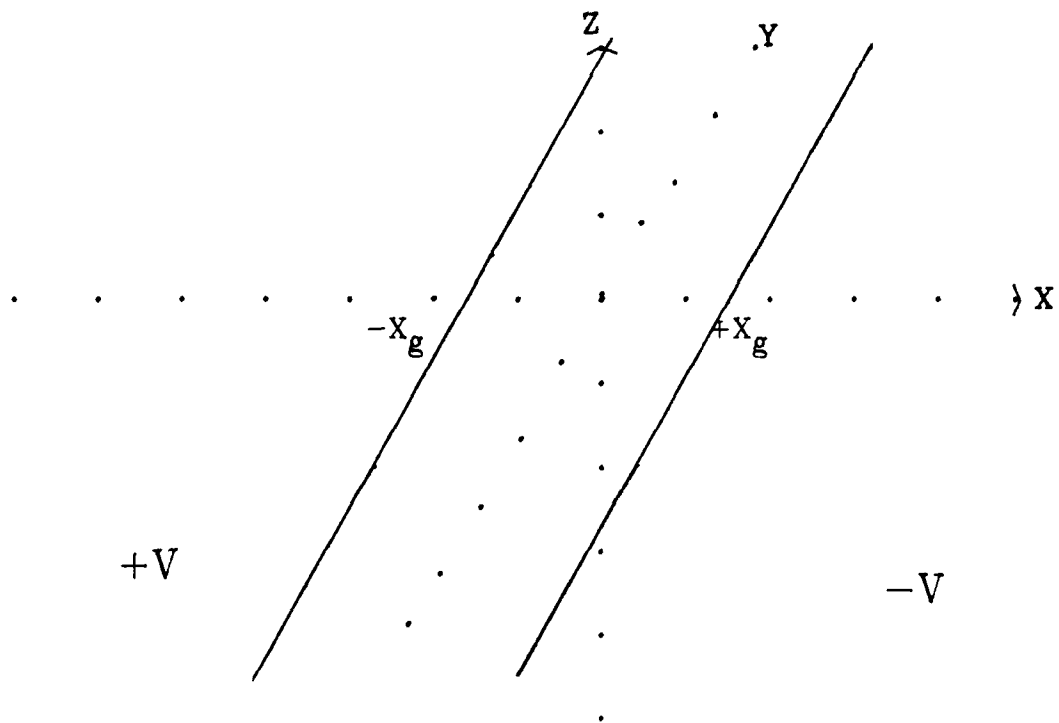


Figure 10. Temporal MSM Photocurrent

Current from a Single Electron-Hole Pair  
in an MSM Detector

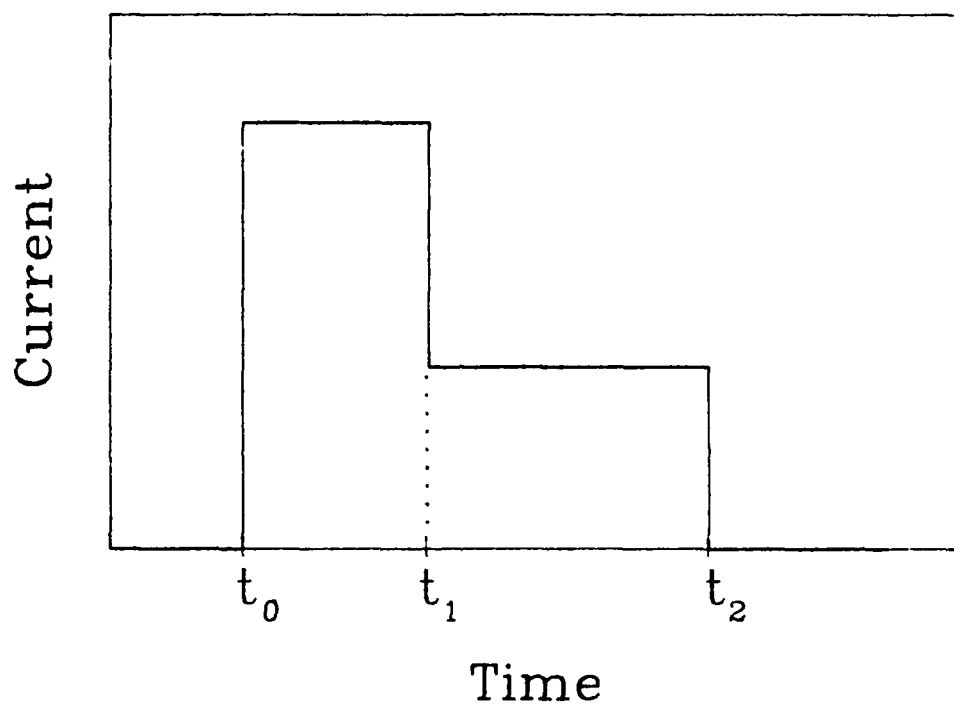


Figure 11. Predicted  $R(\omega)$  for a 4.5- $\mu\text{m}$  Gap Detector versus Bias Voltage.

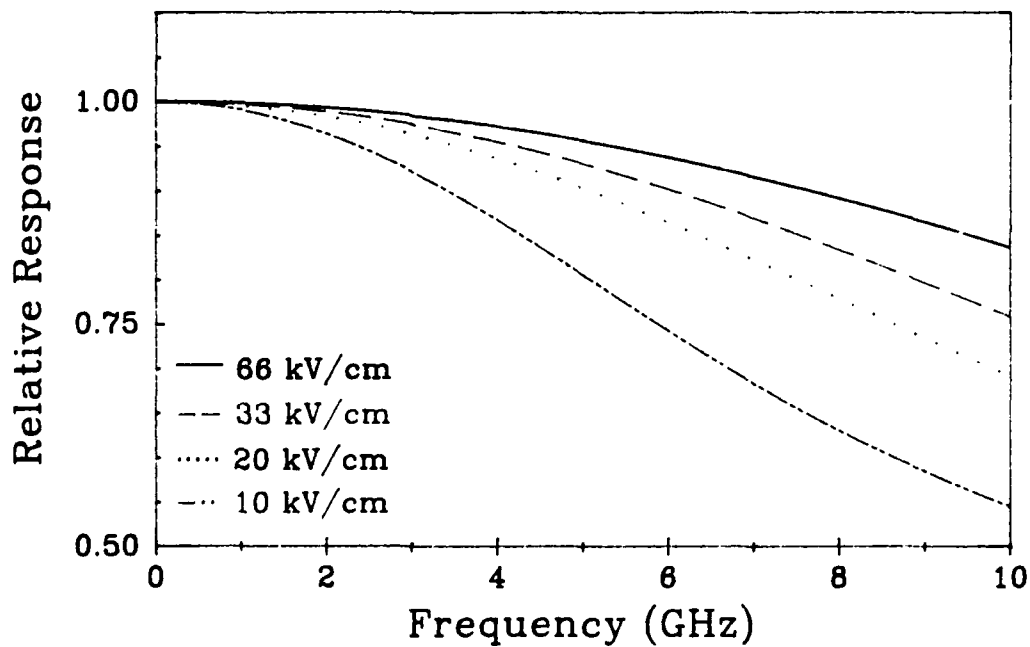
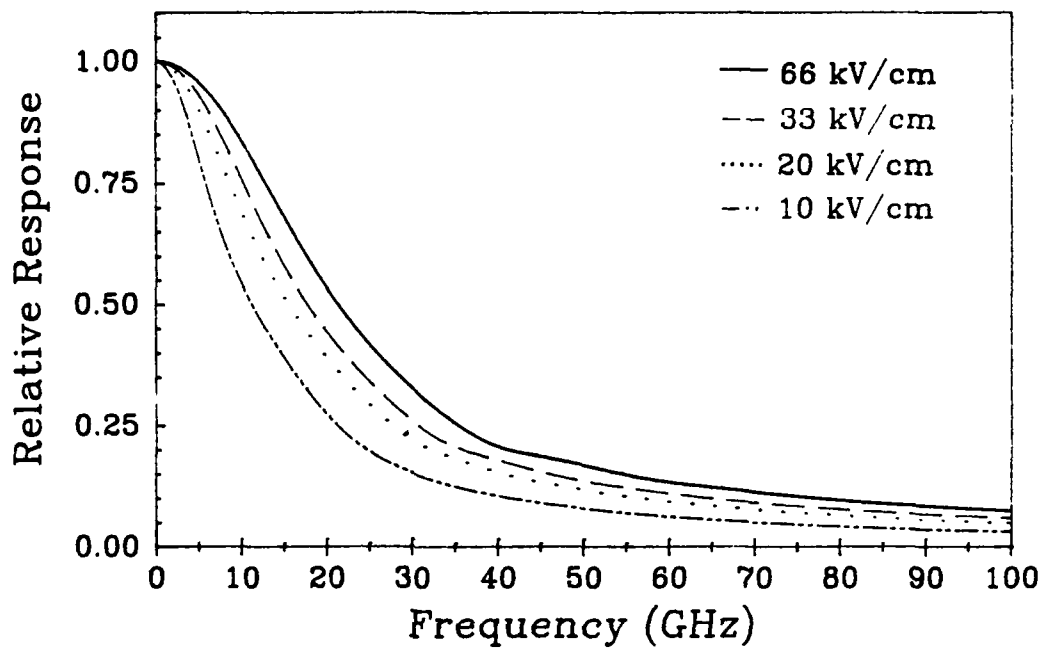


Figure 12. Predicted  $R(\omega)$  for a 3.0- $\mu\text{m}$  Gap Detector versus Bias Voltage.

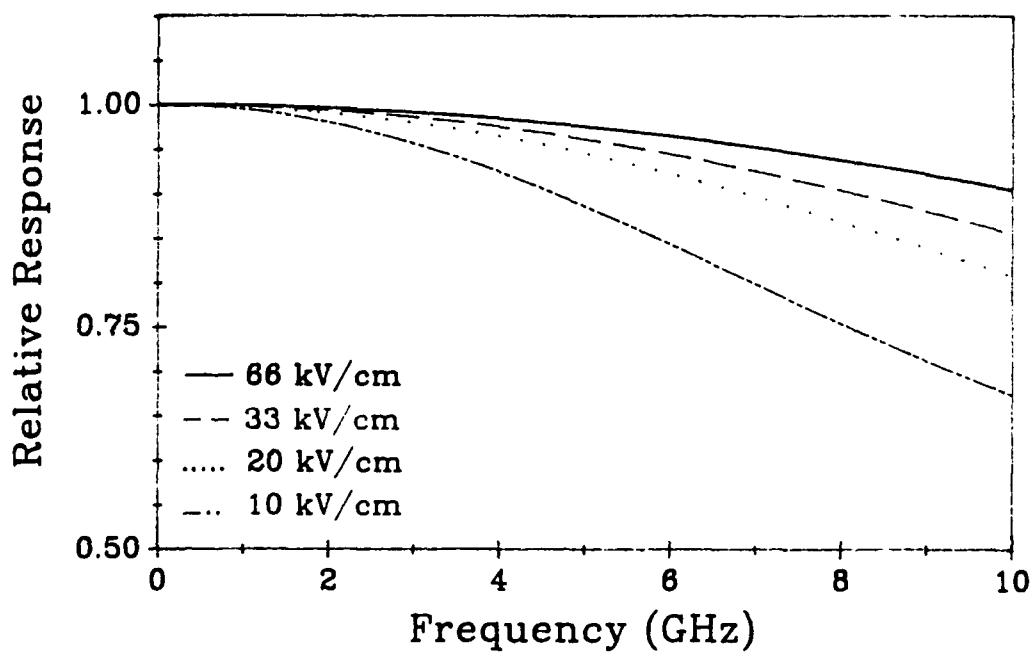
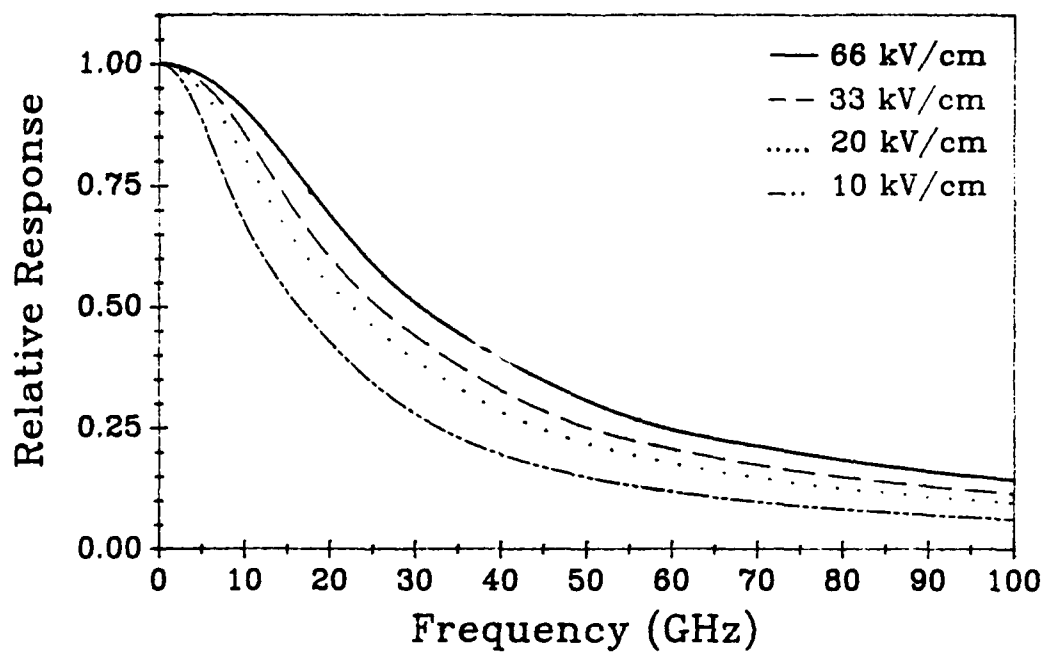


Figure 13. Predicted  $R(\omega)$  for a 1.0- $\mu\text{m}$  Gap Detector versus Bias Voltage.

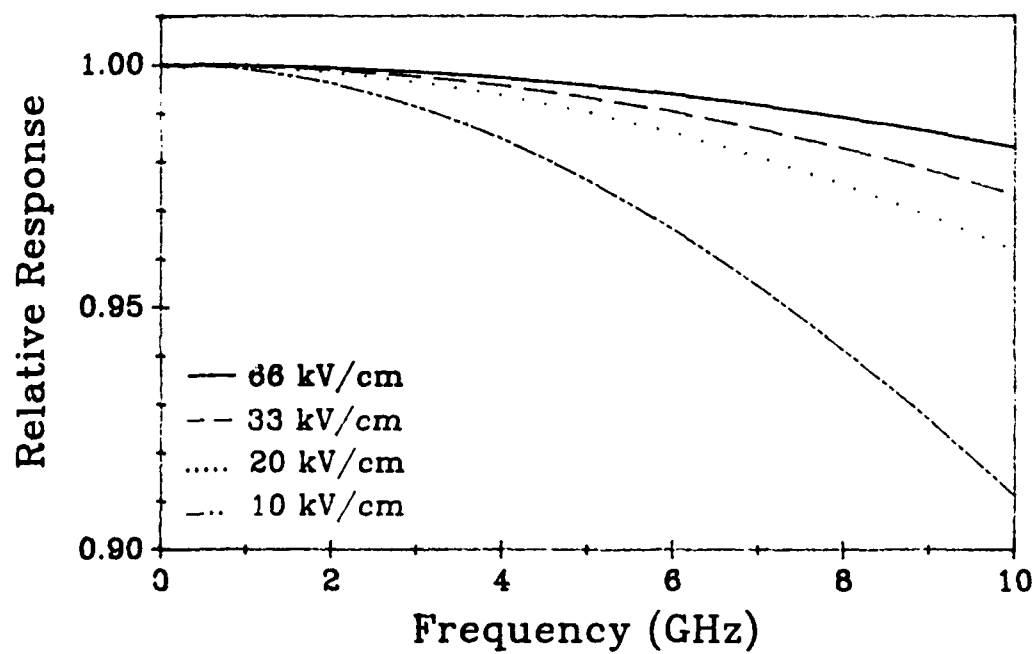
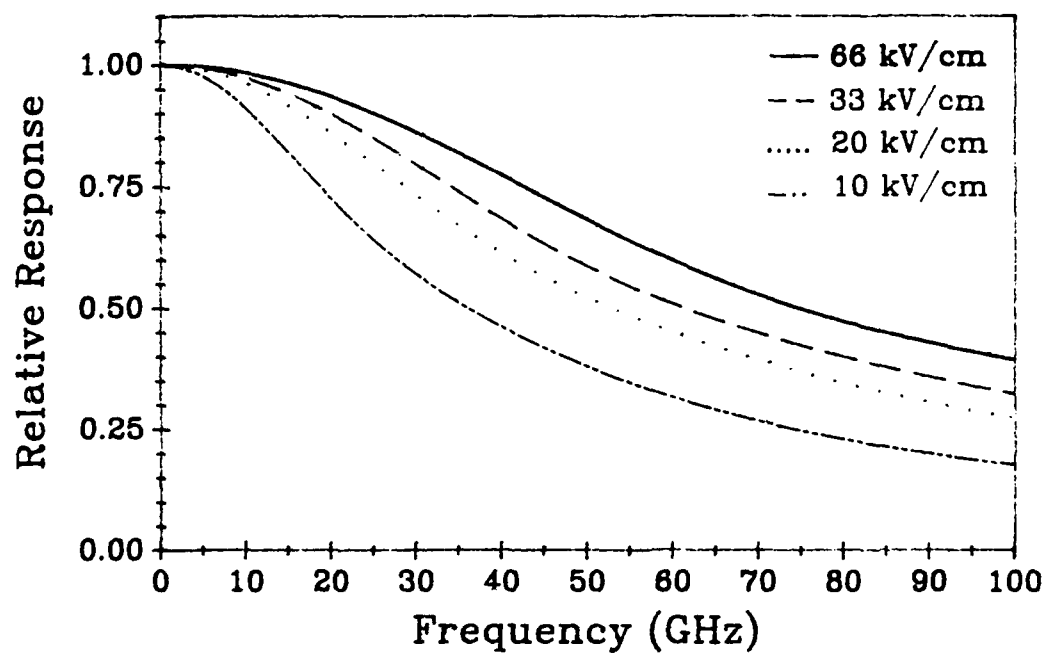


Figure 14. Predicted  $R(\omega)$  for a 4.5- $\mu\text{m}$  Gap Detector versus Beam Position.

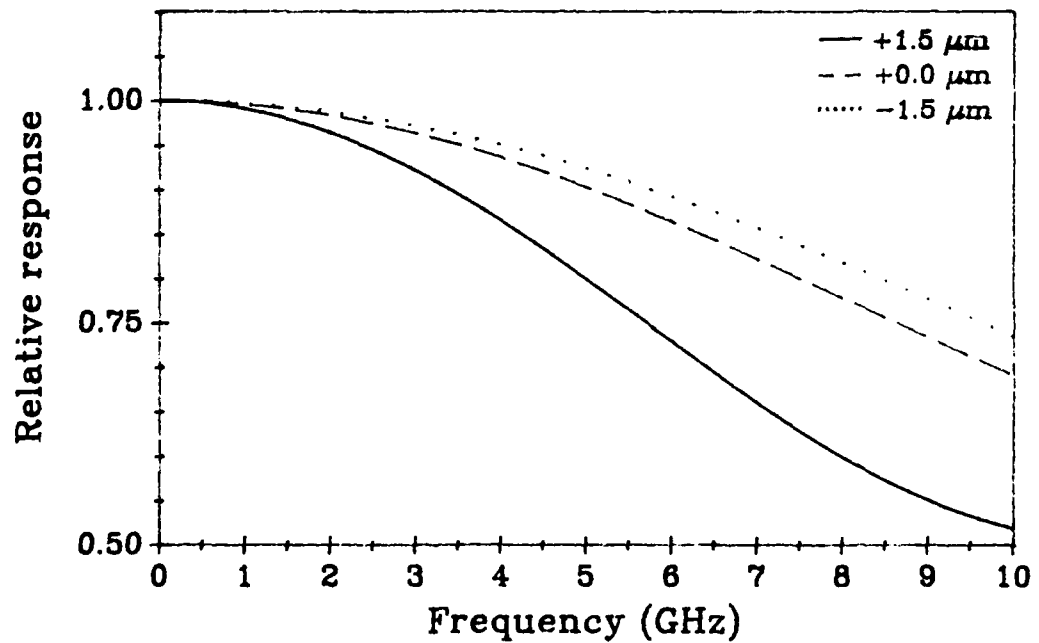
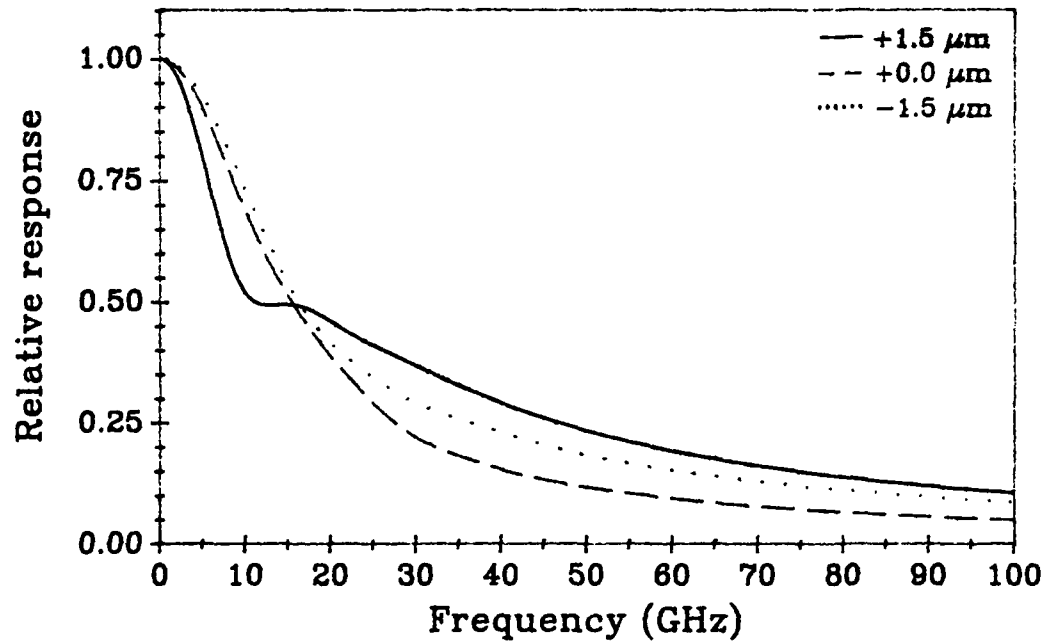


Figure 15. Predicted  $R(\omega)$  for a 3.0- $\mu\text{m}$  Gap Detector versus Beam Position.

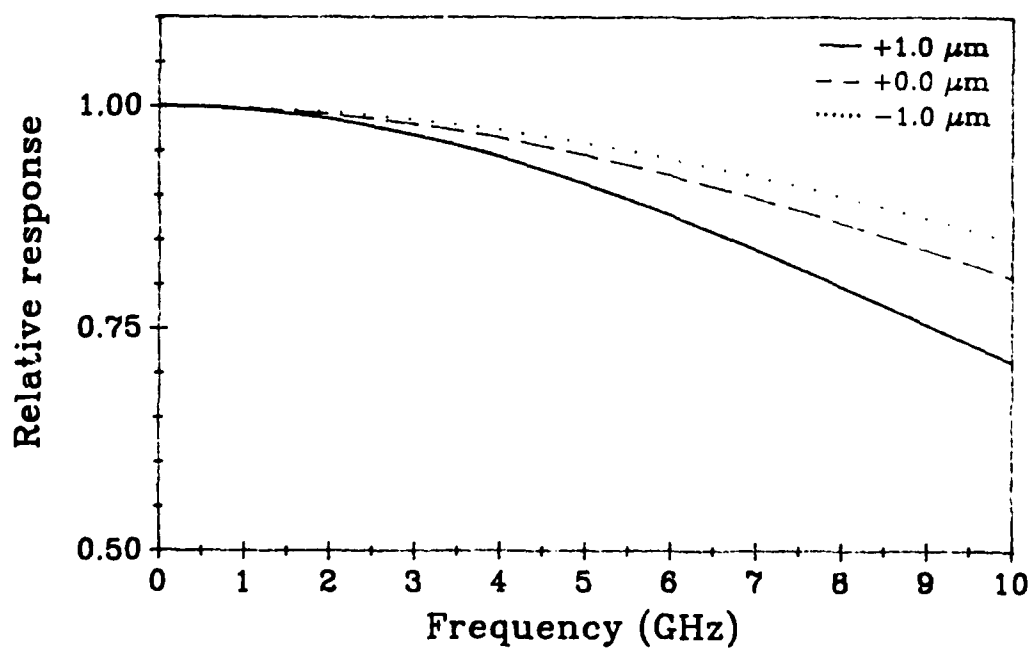
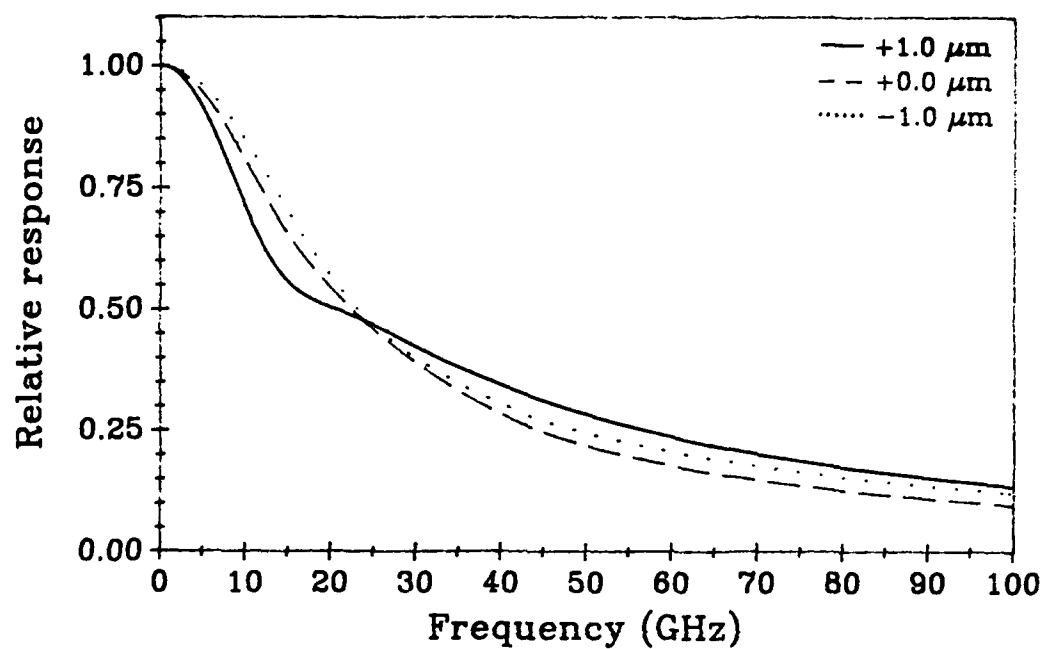


Figure 16. Predicted  $R(\omega)$  for a 1.0- $\mu\text{m}$  Gap Detector versus Beam Position.

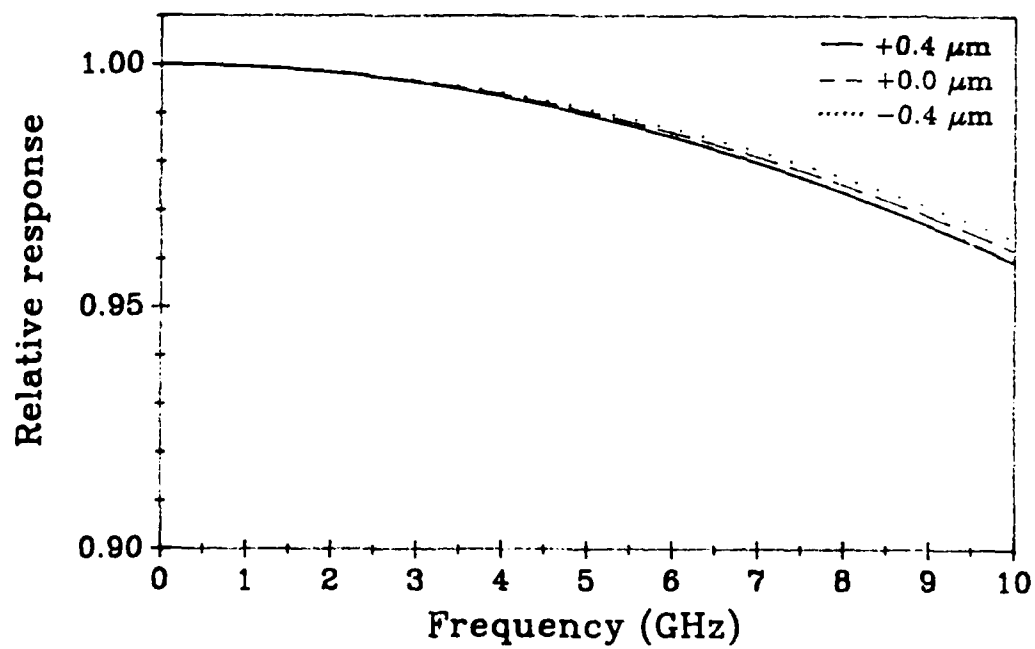
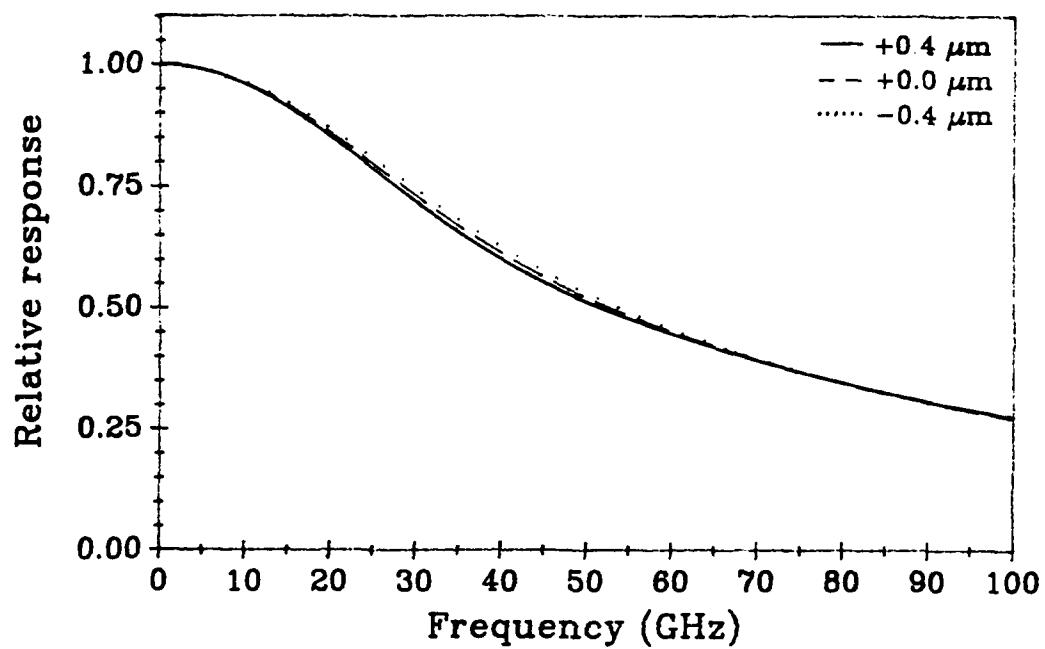


Table 1. Mixing Efficiency verses Tilt Between Two Guassian Beams.

| $\theta$ ( $\mu\text{rad}$ ) | $m$   |
|------------------------------|-------|
| 0.00                         | 1.00  |
| 94                           | 0.990 |
| 250                          | 0.950 |
| 500                          | 0.80  |
| 880                          | 0.50  |
| 1600                         | 0.10  |
| 3345                         | 0.00  |

Table 2. Deviation in Electric Field Strength as a Function of Position from The Surface.

| $Z$ ( $\mu\text{m}$ ) | % Change in $E$ Strength |                   |                   |
|-----------------------|--------------------------|-------------------|-------------------|
|                       | $x = 0.0 \mu\text{m}$    | $1.0 \mu\text{m}$ | $2.0 \mu\text{m}$ |
| 0.5                   | -1.88                    | -2.18             | -3.54             |
| 1.0                   | -3.75                    | -4.33             | -6.77             |
| 1.5                   | -5.62                    | -6.39             | -9.53             |
| 2.0                   | -7.48                    | -8.39             | -11.84            |

Table 3: Bias for a given electric field strength

| <b>E</b><br>( X 10 <sup>4</sup> V/cm) | <b>Bias for a Given Electrode Gap (V)</b> |                   |                   |
|---------------------------------------|---|-------------------|-------------------|
|                                       | 1.0 $\mu\text{m}$                         | 3.0 $\mu\text{m}$ | 4.5 $\mu\text{m}$ |
| 1.0                                   | 1.0                                       | 3.0               | 4.5               |
| 2.0                                   | 2.0                                       | 6.0               | 9.0               |
| 3.3                                   | 3.3                                       | 9.9               | 15.0              |
| 6.6                                   | 6.6                                       | 19.8              | 30.0              |
| $V_{\text{FB}}$                       | 0.16                                      | 1.44              | 3.24              |

Table 4: -3 db Points of three detectors vs applied E-field.

| <b> E </b><br>(x 10 <sup>4</sup> V/cm) | <b>-3 db Point (GHz)</b>      |                   |                   |
|--|-------------------------------|-------------------|-------------------|
|  | <b>Detector Gap Dimension</b> |                   |                   |
|  | 4.5 $\mu\text{m}$             | 3.0 $\mu\text{m}$ | 1.0 $\mu\text{m}$ |
| 6.6                                    | 21.3                          | 30.5              | 74.6              |
| 3.3                                    | 17.7                          | 25.6              | 61.4              |
| 2.0                                    | 15.5                          | 22.5              | 52.9              |
| 1.0                                    | 11.3                          | 16.4              | 36.1              |

Table 5. -3db Points for an L/R Circuit, with R = 50  $\Omega$ .

| -3db Point<br>(GHz) | L<br>(nH) |
|---------------------|-----------|
| 10.0                | 1.378     |
| 9.0                 | 1.531     |
| 8.0                 | 1.723     |
| 6.0                 | 2.297     |
| 4.0                 | 3.446     |
| 2.0                 | 6.892     |

## References

1. S. M. Sze, Physics of Semiconductor Devices, John Wiley and Sons, (1981).
2. S. M. Sze, D. J. Coleman, A. Loya, "Current Transport in Metal-Semiconductor-Metal (MSM) Structures", Solid State Elec., Vol. 14, pg. 1209, (1971).
3. S. F. Soares, Ultraviolet Heterodyne photodetectors, PhD Dissertaion, Dept. of Elec. Eng., Univ. of NM, (1989).
4. R. H. Kingston, Detection of Optical and Infrared Radiation, Springer-Verlag, (1979).
5. H. Goldstein, Classical Mechanics, Addison-Wesley, (1980).
6. S. Ramo. and J. R. Whinnery, Fields and Waves in Modern Radio, Wiley and Sons, (1949).
7. D. Marcuse, "Electrostatic Field of Coplanar Lines Computed with the Point Matching Method", Jour. of Quant. Elec., Vol. 25, No. 5, pg. 939, (1989).
8. A. T. Forrester, R. A. Gudmundsen, P. O. Johnson, Phys. Rev., Vol 99, pg. 1691, (1955).
9. M. C. Teich, Appl. Phys. Lett., Vol. 14, pg. 201, (1969).
10. M. Abramowitz and I. A. Stegun, Handbook of Mathematical Functions, Dover, (1972).
11. A. Yariv, Introduction to Optical Electronics, Holt, Rinehart, and Winston, (1976).

### III. The UV-Heterodyne System

#### A. Introduction

This chapter describes the experimental arrangement. Not only is the hardware described, but also the characterization of the system performance which enables the measurement of absolute detector performance parameters. A discussion of the laser system calibration includes, beam transmission characteristics, beam spotsize at the detector, and mixing efficiency of the two laser beams. Next the measurement of the total gain-loss of the detector electronics as a function of frequency, out to 10 GHz, is described. Finally, the procedure for finding beam focus and establishing a reference coordinate system on the detector is discussed.

#### B. The Experimental Arrangement

The experimental arrangement is shown in Figure 17. The uv-heterodyne system uses a large-frame Ar-ion laser as the local oscillator (LO). This laser operates on one of the doubly ionized lines of Argon, which is a triplet, and an intercavity prism is used to select the 334.5 nm line. This laser line was found to give the most output power of the three lines below 350 nm, the wavelength range of interest for this project. For this laser, the 333.6 nm and 335.8 nm lines have only 58% and 50% of the power in the 334.5 nm line, respectively. Single-frequency operation of the LO is achieved via a temperature-stabilized intracavity etalon and an intracavity aperture to assure single longitudinal and transverse-mode operation, respectively. A set of neutral density filters is used to attenuate the LO beam as

needed. A 50/50 beam splitter combines the LO beam with the signal beam and splits part of the combined beams off to the detector and part to a NIST traceable surface-absorbing calorimeter. The calorimeter head is enclosed in a thermal shield to eliminate drift and inaccuracy in the measured beam power induced by air current fluctuations. This calorimeter, the LO power meter, is used as the standard power meter for the system against which all other power meters are calibrated. The LO power meter readout is sampled by computer via an RS232 interface.

The signal beam is generated by pumping a ring dye laser with a second large-frame Ar-ion laser. The Ar-ion pump laser is operated with an intracavity aperture adjusted to give a  $TEM_{00}$  output beam and the discharge current is adjusted to give an 8 W, 514.5-nm output beam to pump the dye laser. The dye used is DCM which has its spectral peak at 650 nm. By tuning the dye laser to 669 nm and employing a  $LiIO_3$  intracavity frequency doubler, a tunable 334.5-nm signal beam is produced. The fundamental of the dye laser is electronically locked to a temperature-stabilized reference cavity which can be electronically scanned over a maximum range of 30 GHz. This implies a continuously tunable uv range of 60 GHz. A wavemeter measures the frequency of the fundamental dye laser beam to provide a coarse measurement of the frequency of the second-harmonic uv beam, the signal beam, from the dye laser. The second-harmonic beam is separated from the fundamental by a series of three prisms. A 50/50 beam splitter reflects a portion of the signal beam into a commercial Si p-i-n photodiode power meter, the signal power meter. The signal power meter readout is sampled by a computer via an A-to-D converter, with an internal gain of eight, and the digitized data converted back into absolute power at the detector.

A  $\frac{1}{4}$  wave Fresnel rhomb is used to rotate the polarization of the signal beam to be parallel to the LO beam in order to maximize the mixing efficiency of the two beams.

The complex radii of curvature of the LO and signal beams are adjusted to assure maximum overlap and mixing at the detector surface. The technique utilized is briefly discussed here with a more detailed explanation in section D. Maximum beam mixing is accomplished by focusing the two beams into a 25- $\mu\text{m}$  diameter pinhole by a condensing lens. The diffracted wave from the pinhole is focused on to the detector surface by a 15X reflecting microscope objective, 160 mm away from the pinhole. A reflecting microscope objective was chosen to avoid the absorption characterizing standard refracting objectives in the uv. The smallest focused spotsize at the detector surface, measured by a scanning knife edge technique is  $\approx 1.7 \mu\text{m}$  FWHM.

The detector photocurrent is separated into rf and dc components by a commercial biasing tee. The dc-photocurrent is measured with a picoammeter while an electrometer is used to provide a dc bias for the detector. The rf photocurrent from the detector is amplified by one of several wideband, high-gain, low-noise amplifiers covering the frequency range from 1.0 MHz to 18 GHz. Narrow band, very low noise amplifiers are used to provide an improved absolute responsivity measurement. The gain of each amplifier was chosen such that the -114 dbm thermal noise (plus amplifier noise) could be seen over the noise floor of the rf spectrum analyzer used to measure the amplitude and frequency of the heterodyne signal. The -114 dbm thermal noise limit represents a 300-K, 1-MHz bandwidth, thermal noise source. A pair of wideband, dc to 15 GHz, double-pole, eight-throw switches permits simple switching of

amplifiers, except for the 1-500 MHz and 8-18-GHz amplifiers, without disturbing the detector position. The necessity for a separate low frequency bias tee prohibited the 1-500-MHz amplifier being connected to the switching network. Bandwidth considerations obviously dictated that the 8-18-GHz amplifier also has a separate circuit. The signal cable from the detector is tied down to the optical table to minimize detector movement while the cable is switched between the three separate electronic systems. The heterodyne beatnote signal and dc photocurrent, respectively measured by the spectrum analyzer and picoammeter, are then down loaded via an IEEE-488 bus into a PC-AT compatible computer. The computer also monitors the LO and signal beam powermeters, so that absolute responsivity verses frequency is determined.

The detector is mounted in a computer-controlled micropositioning XYZ stage which allows for precise positioning of its surface relative to the laser beams. A micropositioner controller drives three motorized micropositioners. These positioners have a  $0.1\text{-}\mu\text{m}$  resolution and  $\approx 0.3\text{-}\mu\text{m}$  repeatability over a  $\geq 100\text{-}\mu\text{m}$  range. The micropositioner is computer controlled over the IEEE bus. This high-precision position control allows for repeatable beam placement on the detector and provides the capability for making detailed high-resolution XY maps of detector response. Precise beam focus is obtained by using the z-axis micropositioner. This allows for very repeatable control of the focus position allowing a reproducible spotsize of  $\geq 2.1\text{-}\mu\text{m}$  FWHM on the detector surface. This computer-controlled micropositioner also allows the detector to be moved up to 35 mm away from focus, for measuring beam transmission constants, and returning to within less than  $10\text{ }\mu\text{m}$  of

focus, greatly reducing the repositioning time of the detector in the focused beam.

Other beam diagnostic devices, including a scanning Fabry-Perot etalon and a spectrometer, are also available for additional beam characterization as needed.

### C. System Calibration

In order to make absolute responsivity measurements, several system constants must be known. The rf spectrum analyzer, picoammeter, and calorimeter (LO power meter) were calibrated according to their respective manufacturer's directions. Next, a commercial Si p-i-n photodiode power meter, which is normally used as the signal power meter, was calibrated with respect to the LO power meter. This cross calibration was performed by first measuring the reflectance to transmission ratio of a beam splitter, and then placing the LO power meter in the reflected beam from beam splitter, and the commercial photodiode power meter in the transmitted beam. The output from the commercial photodiode power meter was sampled with an A-to-D converter and the zero intensity level was subtracted. From the measured power at the LO power meter and the known transmission ratio of the beam splitter, a digital to analog calibration factor,  $d \rightarrow a.conv$ , was calculated for this detector. Over 100 individual  $d \rightarrow a.conv$  factors were averaged together to get a standard deviation,  $\leq 0.002$  of the average, and an average calibration factor for this detector over all operational settings. This detector has a three front panel settings of 6328, 5145, and 4880 which insert different gain settings at the output of the power meter. Also, a magnitude multiplier, from 0.1 to  $10^4$  in decade steps,

can be set. Hence, the power at this commercial photodiode power meter is obtained from the appropriate value for  $d \rightarrow a \cdot \text{conv}$ , corresponding to one of the three front panel settings and the front panel decade step, and the digitized signal strength.

A second Si p-i-n photodiode was also cross calibrated to the LO power meter. The LO power meter and the second p-i-n detector were placed as described above. The output of this photodiode was read by the picoammeter, with the bias provided by the electrometer. The photocurrent from the detector as measured by the picoammeter was transferred to the computer over the IEEE bus. Again 100 data points, each corrected for dark current, were averaged to get a dc responsivity of  $0.1446 \pm 0.0002$  Amps/Watt.

With these three calibrated detectors, the transmission characteristics of the LO beam and signal beam could be measured. The LO and signal beam transmission coefficients are measured each day, but not for each data run, assuming that once the system is aligned, and not disturbed, that the transmission characteristics through the system are constant for the day. The LO beam-transmission coefficient, LO.Trans, is calculated by taking the ratio of the power exiting the microscope objective to the power measured by the LO power meter. The signal beam-transmission coefficient, Sig.Trans, is measured by taking the ratio of the power exiting the microscope objective to the power at the signal power meter.

For these measurements, the three calibrated power meters are used. The calorimeter is set in its normal position as the LO power meter. The commercial p-i-n photodiode is used to measure the power exiting the microscope objective. The second p-i-n photodiode is placed

to sample the power in the signal beam, where the signal power meter normally resides. For each transmission coefficient, 100 data points for the zero intensity level are averaged and this average dark signal is subtracted from the average of 100 data points under illumination for each detector to give an average transmission coefficient for that day. The day to day fluctuation of the average transmission coefficients is less than 5%.

The final calibration is the gain verses frequency for the various amplifiers, cables, and bias tees used between the detector and the rf-spectrum analyzer. The gain verses frequency for all of the amplifiers from 400 MHz to 10 GHz was measured using an rf network analyzer. The entire cable-bias tee-switch-amplifier-switch-cable assembly that connects the detector to the rf-spectrum analyzer was tested as a unit. Hence, any losses in the cables, switches, etc. are automatically taken into account. The gain verses frequency data from the rf-network analyzer was then put into the computer and a 10th order polynomial fit to the data was performed. This 10th order fit was performed over two frequency ranges for each amplifier. First, an entire amplifier's frequency range was fitted. Secondly, only the frequency range of a given amplifier that was used for normal measurements was fitted. Not surprisingly, it was found that a better fit was possible for a more limited range of frequencies. The gain verses frequency for each of the amplifiers and the limited frequency range fit are shown in Figures 18 to 20. The coefficients of the polynomial fit, listed in Table 6, for the limited range of frequencies for each amplifier was then used to correct the measured rf data for amplifier/cable/bias tee frequency dependency. Due to the 130-MHz lower frequency limit of the network

analyzer, the low-frequency bias tee and 1-500 MHz amplifier used in a different set-up to calibrate the gain. This low frequency arrangement was calibrated by using the -20 dbm, 100 MHz calibration signal from the rf spectrum analyzer as the test signal. This calibration signal was input into the electronics and the total gain of the cable-bias tee-amplifier-cable assembly was measured with the spectrum analyzer. A calibrated 20-db attenuator was used to reduce the signal in order to avoid saturating the amplifier. The measured 45.6-db gain at 100 MHz was assumed to be flat across the entire 1-500 MHz range. The recently obtained 8-18 GHz amplifier has yet to be calibrated due to lack of availability of the network analyzer.

#### D. Beam Alignment Procedure

The alignment of the signal beam with respect to the LO beam is of extreme importance in heterodyne measurements. The heterodyne beatnote signal comes from the  $E_{LO} \cdot E_{SIG}$  term in the intensity pattern at the detector. It is then easily seen that the two wavefronts should be as closely matched as possible. To achieve this matching a 25- $\mu$ m diameter pinhole is used. A 75-mm focal length condensing lens focuses the two unmatched beams onto the pinhole. Diffraction through the pinhole, its diameter being smaller than the  $\geq 30$ - $\mu$ m-diameter focal spot of the beams, matches the wavefront curvature of the LO and signal beams. The first Airy disk of the diffracted beams slightly overfills the secondary mirror of the 15X reflecting microscope objective placed 160 mm away, nearly maximizing the transmission through the objective.

With the wavefronts matched, the only parameter left to adjust is the tilt between the two beams. A tilt between the two beams that

produces a  $2\pi$  phase shift across the beam diameter will cause the total integrated intensity in the beams to not change with time. Hence, a beatnote will not be observed. For a maximum heterodyne signal the tilt should ideally be zero.

The tilt between the two beams is reduced by observing the LO and signal beams after several meters of propagation beyond the pinhole. First the LO beam is centered in the pinhole by maximizing the power through the pinhole. Then this beam is propagated a distance of approximately 12 m and centered on a CCD television camera. To reduce beam spreading, a lens condenses the beam onto the active area of the camera. However, the lens does not recollimate the beam as this would greatly reduce the sensitivity of this alignment procedure. Next, the signal beam is observed by the camera. Its position is adjusted to give maximum transmission through the pinhole, while having its peak intensity co-located with the peak intensity of the LO beam as seen by the CCD camera. If care is taken to adjust the intensity of both beams to be nearly equal at the camera then the intensity patterns of both beams are seen to be nearly identical. With this technique a distance of 1 mm between the two peak intensities at the CCD camera is equal to an  $8\text{-}\mu\text{rad}$  tilt between the beams. A  $\frac{1}{2}$ -wavelength phase walk-off at the detector corresponds to a  $4.5\ \mu\text{rad}$  tilt between the beams. It is straight forward to align the beams to have less than a 0.05 mm difference between beam centers at the CCD camera, implying  $1/10$  wavelength tilt between the beams, or less, at the detector.

The net efficiency of this alignment technique can be monitored by comparing the low-frequency extrapolation of the rf-heterodyne quantum efficiency to the dc quantum efficiency for a known detector. A

commercial Si p-i-n photodiode, not the signal power meter, with a well characterized response was tested to measure the mixing efficiency. The results are shown in Figure 21. The rf measurements show the specified  $\pm 3$ -db roll-off point of  $\geq 100$  MHz and the extrapolated rf signal matches the measured dc response. The lowest measurable rf frequency in the system is 1 MHz. The lower bound to the heterodyne frequency range is limited by two factors. First, the lowest frequency amplifier cuts off below 1 MHz. Second, due to jitter of the LO frequency, the rf-spectrum analyzer must use a 1-MHz sampling window in order to get accurate measurements. The measured drift between the LO and signal beams is in excess of 100 MHz per hour. The frequency jitter in the beatnote is such that a smaller sampling window does not collect all of the rf signal resulting in a reduced beatnote signal. A larger sampling window of 3 MHz, however, does not change the beatnote amplitude from the 1-MHz window.

The matching of the dc and extrapolated rf measurements indicates that the tilt between the two beams is less than  $1/10$  of a wavelength. This is seen by actually calculating the mixing efficiency,  $m$ , of two gaussian beams of equal spot size, but with different tilts as has been shown above in Chapter II. (Eqns 21-26) The mixing efficiency versus tilt has been plotted in Chapter II, Fig. 5, and tabulated in Table 1. Hence, the mixing efficiency between the two beams must be  $\geq 0.95$  to fit the data, implying that the prescribed alignment procedure reduces the residual tilt between the LO and signal beams to  $\leq 0.1$  wavelength across the beam.

### E. Detector Alignment

Once the two beams are aligned they must be accurately placed on the detector. First, the detector is moved  $\approx 1$  mm away from focus. Using the florescence of a white business card when illuminated by uv light, the detector surface can then be seen in the reflected light to get a rough position. The detector is then moved toward focus in 0.1-mm steps keeping the active area of the detector within the beam. About 0.1 mm away from focus, the active area of the detector fills the region that can be seen in the reflected light. This region is then centered in the beam. A beatnote is usually detectable at this point. Taking the detector in the last 0.1 mm causes all definition in the reflected spot to be lost. If the beatnote is still seen on the rf spectrum analyzer, then the beam position is close enough for fine focus adjustment. If, however, a beatnote is not observed, the detector needs to be backed out from focus until the beatnote reappears and the detector centered in the beam by peaking the beatnote signal.

Fine adjustment of beam focus uses a scheme much like a confocal microscope. A sensitive Si photodiode detector is placed to measure the reflected light returning from the detector and going back through the 25- $\mu\text{m}$  mode-matching pinhole. Maximum transmission back through the pinhole, towards the LO laser, will be obtained when the detector is at the focus of the beam. Before these fine adjustments are made, the detector is moved  $\approx 50$   $\mu\text{m}$  from the active area, perpendicular to the focus axis, in order to avoid problems caused by the detector construction (edges of the metalization, dielectric window, bonding pads, etc). Then the sample is scanned to maximize the transmission

through the pinhole of the reflected beam. The point of maximum transmission through the pinhole corresponds to the best focus.

Once focus is established, the detector is returned to the position where a beatnote was previously observed, without disturbing the focus position. A longitudinal scan, parallel to the gap region, of the dc photocurrent versus position is recorded. If the beam goes across one of the metal pads as shown in Fig. 22a, then the photocurrent looks similar to that shown in Fig. 22b where the peaks occur at the semiconductor-metal interfaces. The center of the valley is arbitrarily defined as  $y = 0$ . Once the  $y$ , or longitudinal position, is defined then the  $x$ , or transverse, axis is defined. The beam is scanned perpendicular to the gap and the dc photocurrent is recorded. Two scans are made in this direction, one with a bias on the detector, and the second with zero bias. The resulting photocurrents are shown in Fig. 23. The non-zero bias curve is used to measure the beam spot size with the distance between the peak and the 50% point on the steepest side defined as the HWHM spot size of the beam. The second trace shows absolute dc photocurrent versus position at zero bias. Due to the symmetry of the detector, a current will flow in the external circuit if the beam is not exactly centered. Again by symmetry, the sign of the current changes as the beam position moves across the center of the gap. The minimum of the absolute-unbiased-dc photocurrent is taken to be gap center and defined as the  $x = 0$  position. The beam can be centered perpendicular to the gap to better than  $0.1 \mu\text{m}$ , the resolution of the micropositioner. Due to a slight asymmetry in the electrical circuit, there may exist a slight electrical imbalance in the zero-bias detector. This asymmetry may shift the null position of the unbiased photocurrent

slightly from gap center. The sharpness of this unbiased photocurrent suggests that a very sensitive position sensor is possible with these detectors.

Since the responsivity of the detector is very position dependent, several frequency response curves of a 3.0- $\mu\text{m}$  gap device were made. At a 3-V bias, four different scans were made over a two day period. Between each scan, the detector was moved and then repositioned back to  $x = y = 0$  as defined above. The LO and signal beams were also realigned on the second day to further test the reproducibility of our beam alignment technique. The average of the four scans are shown in Fig. 24. A standard deviation of the four data sets was calculated for similar frequencies in each set and is also shown. The resulting standard deviation was  $\leq 0.20$ , or 1 db, of the signal at any given frequency, showing excellent day to day reproducibility not only of detector placement in the beam, but also of the beam alignment technique.

Figure 17: UV Heterodyne System.

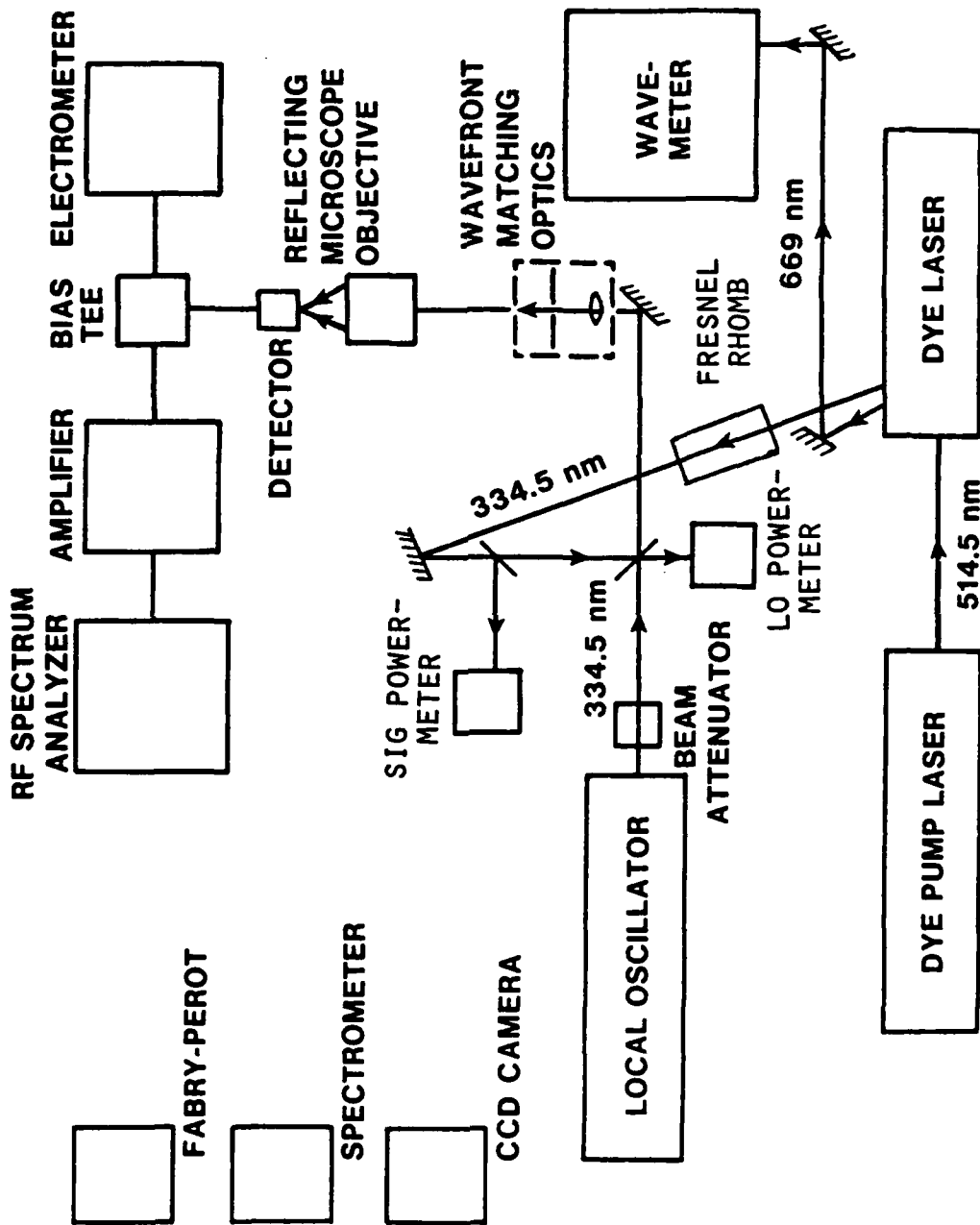


Figure 18: Gain versus Frequency for the 400 MHz to 2.0 GHz Amplifier.

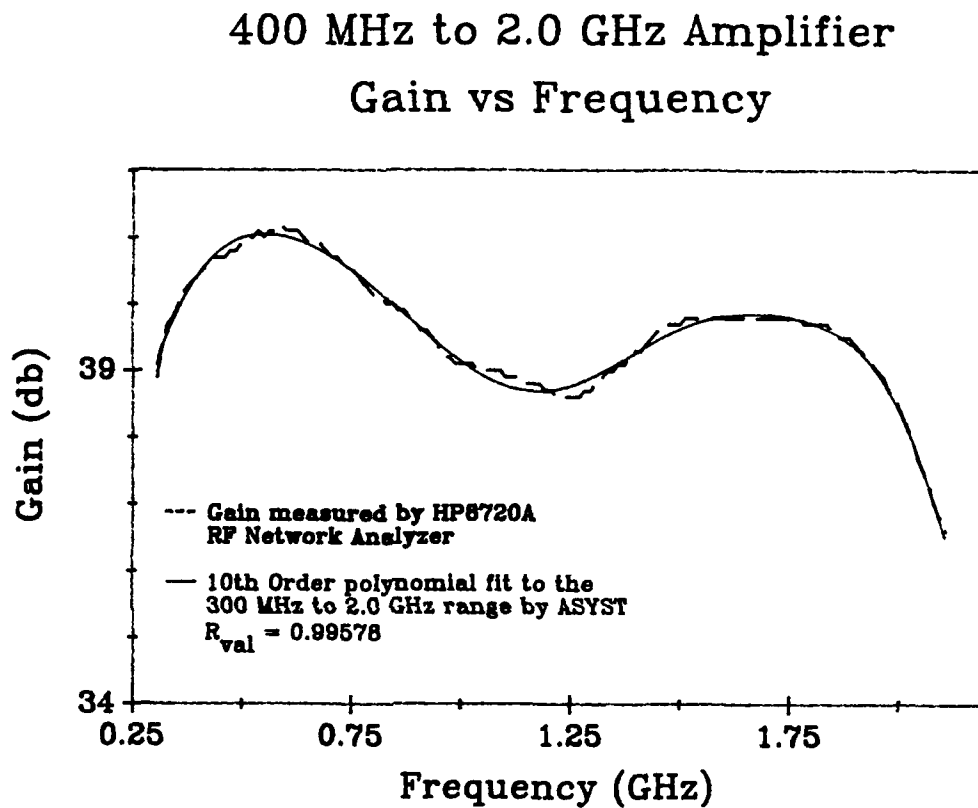


Figure 19: Gain versus Frequency for the 2.0 GHz to 8.0 GHz Amplifier.

### 2.0 GHz to 8.0 GHz Amplifier Gain vs Frequency

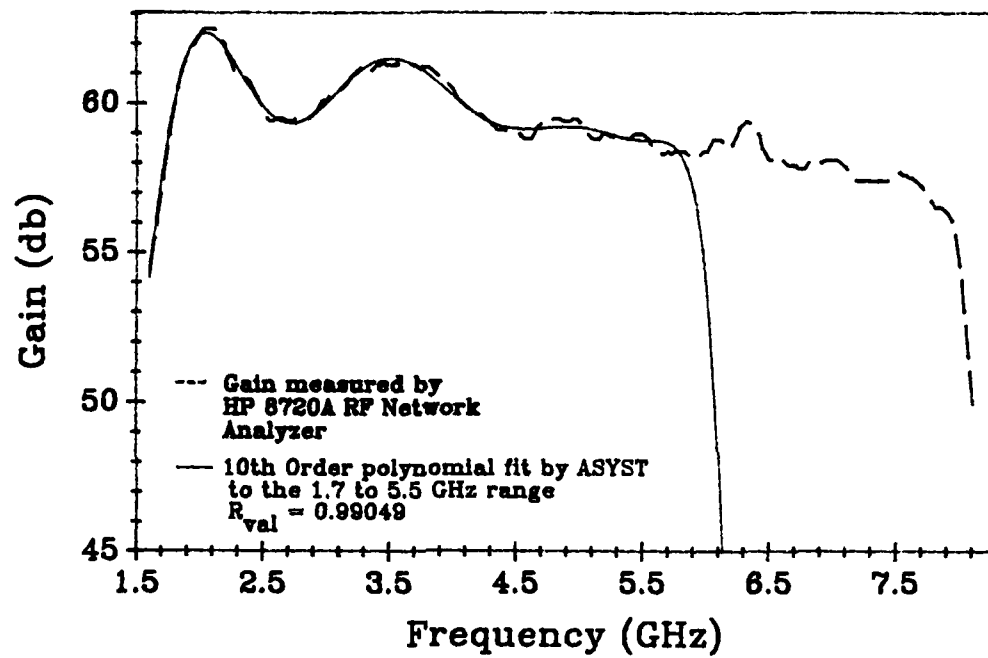


Figure 20: Gain versus Frequency for the 5.0 GHz to 10.0 GHz Amplifier.

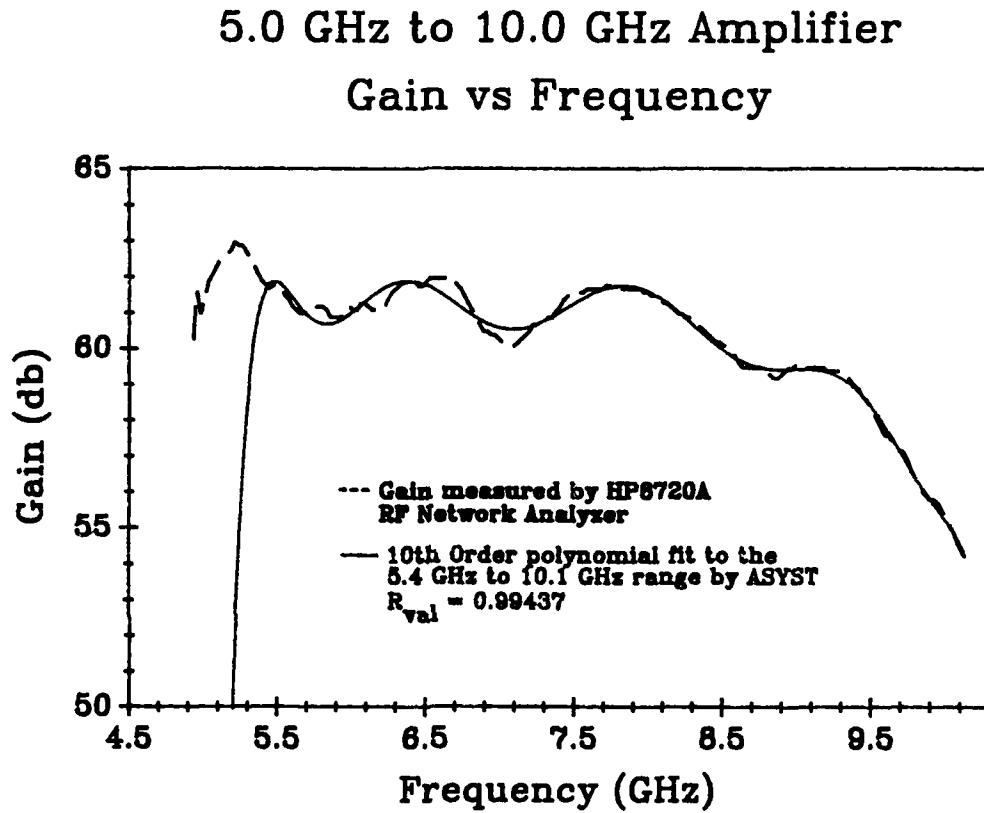


Figure 21: Mixing Efficiency Test.

### Frequency Response of a Commercial UV P-I-N Detector

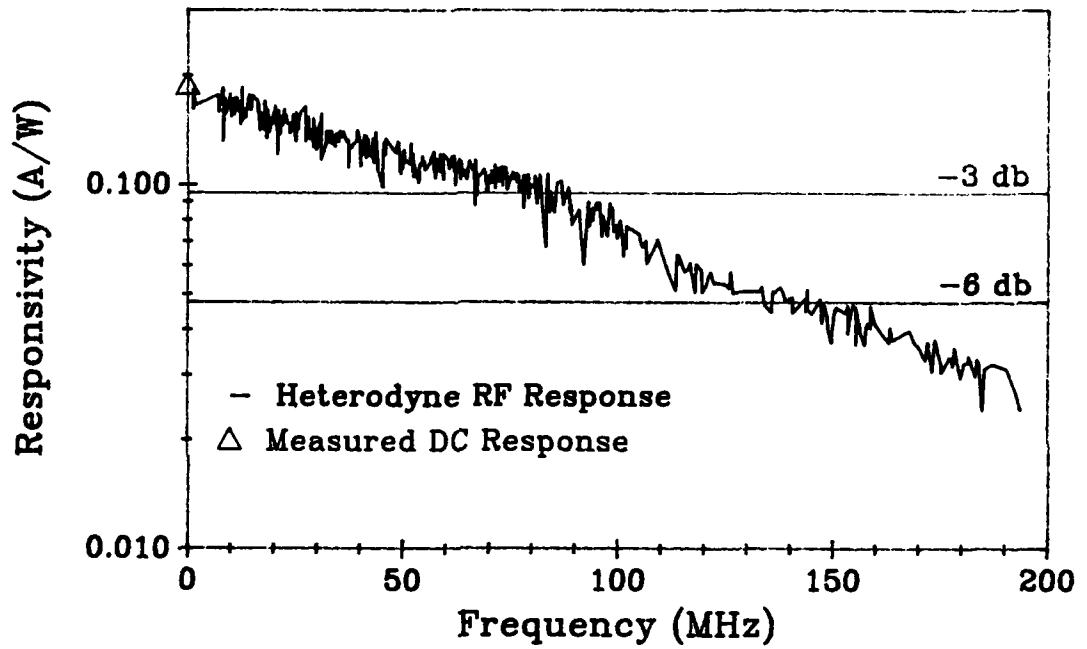
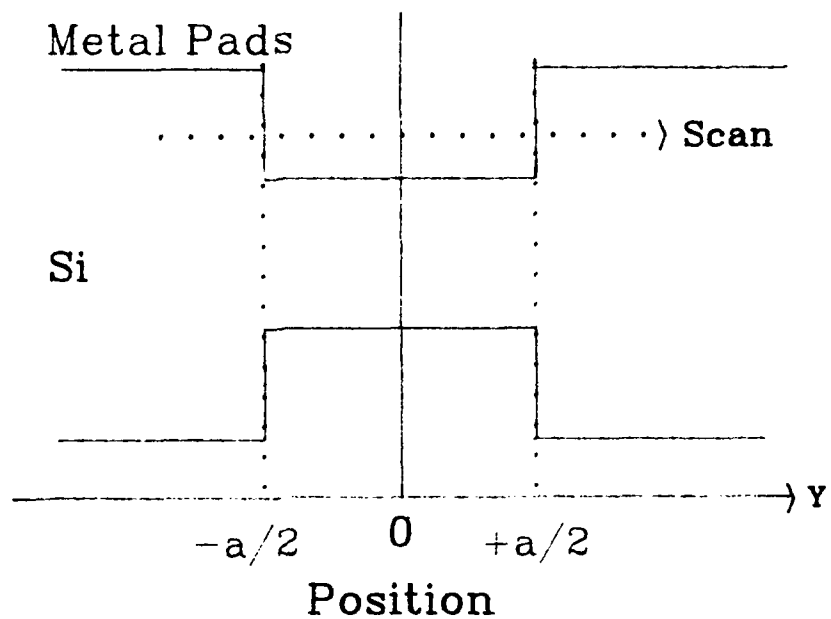


Figure 22: Beam Alignment on the Detector Parallel to the Detector Gap.

## a. Beam position on the detector



## b. Photocurrent versus beam position

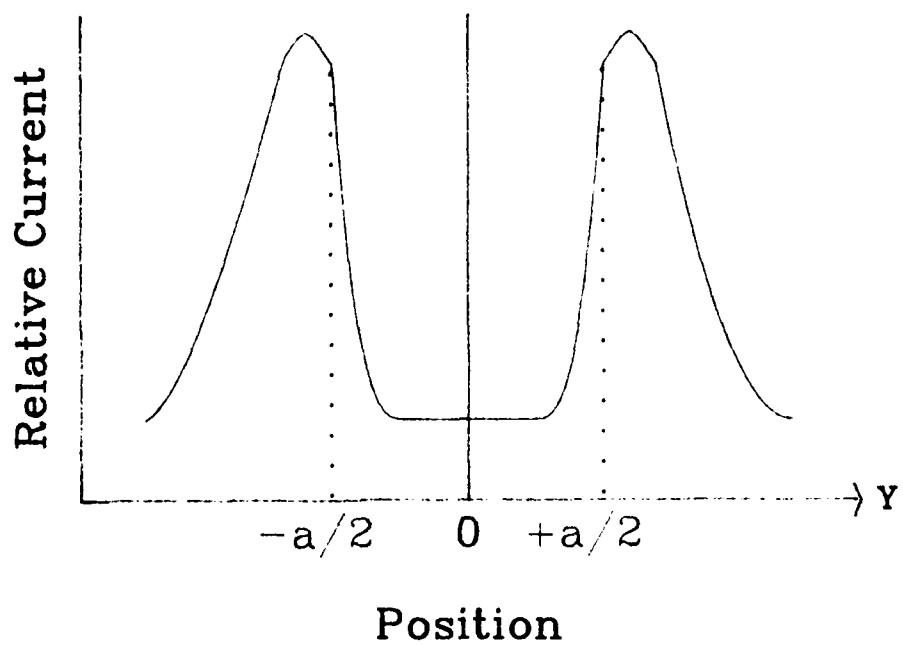
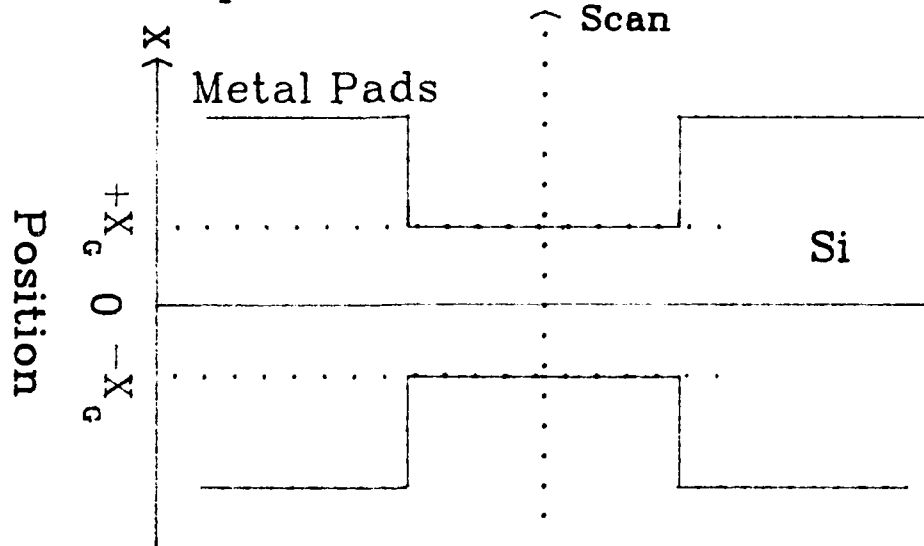


Figure 23: Beam Alignment on the Detector Perpendicular to the Detector Gap.

a. Beam position on the detector



b. Photocurrent versus beam position

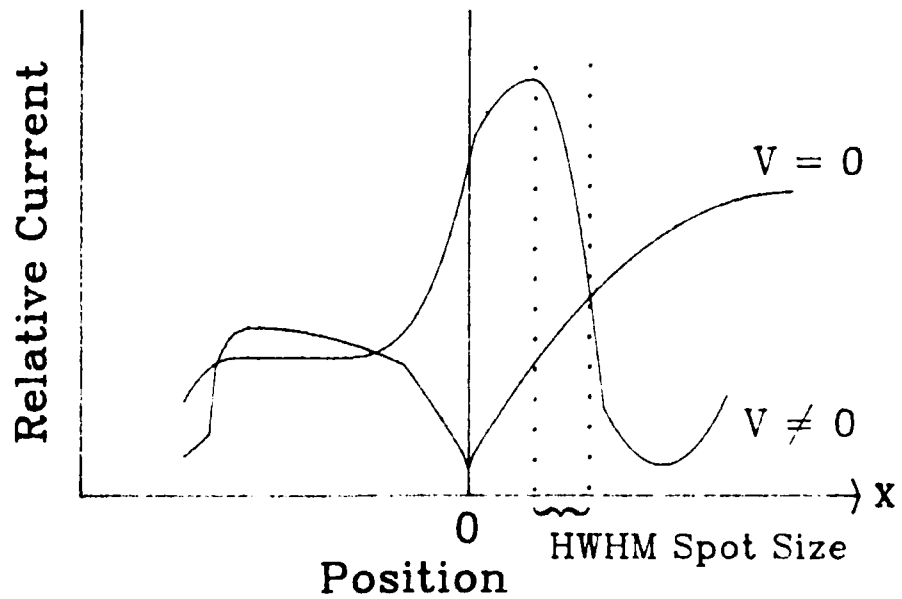


Figure 24: Day-to-Day Reproducibility.

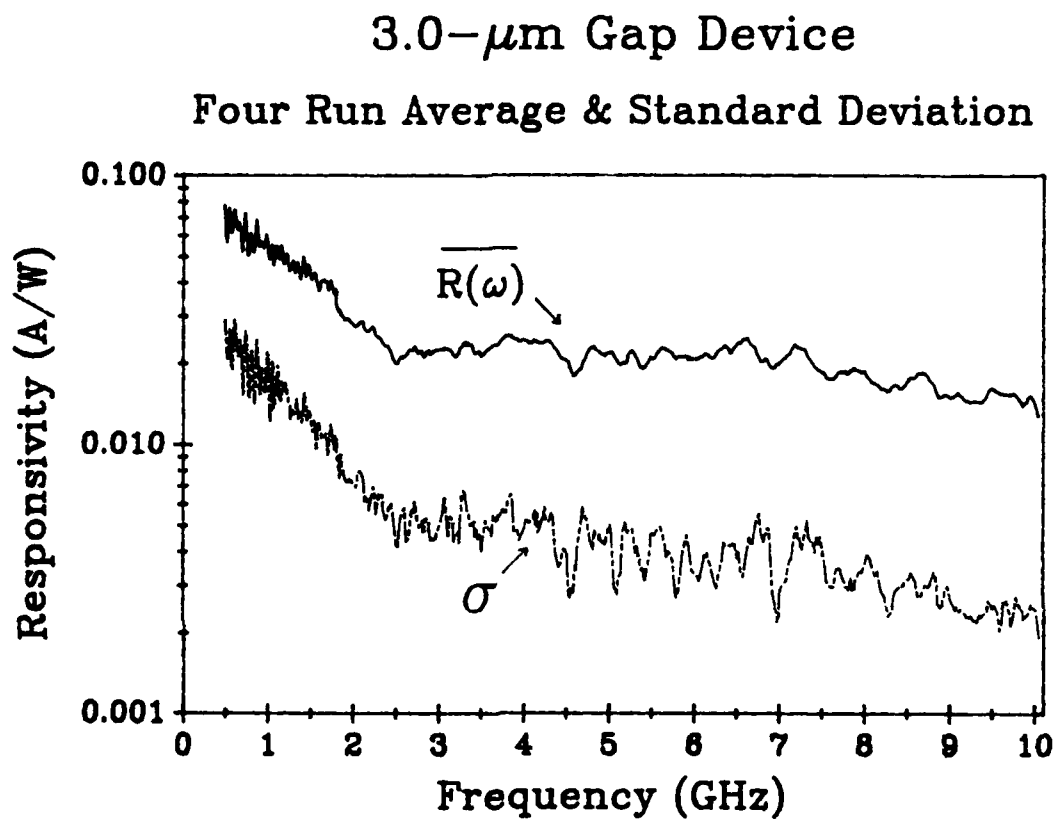


Table 6: Coefficients for 10th Order Fit for Amplifier Gain as a Function of Frequency ( $G(\text{db}) = \sum a_n f^n$ )

| COEF.<br>$a_n$ | AMPLIFIER             |                       |                        |
|----------------|-----------------------|-----------------------|------------------------|
|                | 400 MHz to<br>2.0 GHz | 1.7 GHz to<br>5.5 GHz | 5.4 GHz to<br>10.0 GHz |
| 10             | 56.615409740220       | 0.0000706449132       | -0.034669985181        |
| 9              | -664.3680499821       | -0.107262584531       | 2.7136987373078        |
| 8              | 3372.122544016        | 3.6073214222297       | -95.05280304701        |
| 7              | -9076.475989137       | -53.13833277679       | 1961.825136566         |
| 6              | 17466.52438043        | 446.0212103961        | -26419.08780396        |
| 5              | -20437.32224607       | -2341.092570918       | 242534.15840953        |
| 4              | 15666.62864537        | 7939.527076572        | -1537044.876502        |
| 3              | -7697.071714606       | -17330.78570514       | 6639520.52524          |
| 2              | 2262.1940293763       | 23381.26270615        | -18708024.97379        |
| 1              | -335.553673821        | -17606.59456297       | 31047879.873476        |
| 0              | 55.85331438977        | 5666.937584102        | -23045989.86179        |

## Chapter IV

### Experimental Results

#### A. Introduction

In this chapter the results of several experiments and comparisons with theory are presented. The d.c. current versus bias for both dark and illuminated cases are presented a number of different detector geometries. The model derived in Chapter II is compared to the high-frequency response data for three planar gap detectors with gap dimensions of 1.0, 3.0 and 4.5  $\mu\text{m}$  under a variety of test conditions. The low-frequency behavior of the planar gap detectors is compared to a simple pole. The frequency response of the planar gap devices are compared to the interdigitated detectors. Finally, maps of the responsivity of the detector surface will be presented and correlated to the applied electric field.

#### B. Experimental Procedure

Once the heterodyne system is aligned and the detector positioned in the system, as described in the previous chapter, a number of basic experiments were performed on each detector. The tests, comprising a full basic data set on each detector, include:

- determination of d.c. quantum efficiency versus bias voltage.
- determination of NEP versus bias voltage.
- Frequency response versus bias voltage at a given position on the detector.
- Frequency response versus position for a given bias voltage.
- Responsivity maps of detector surface versus bias at d.c., 1.

5, and 9-GHz.

Each of these tests are now discussed in more detail.

The first experiment performed on a detector is a current versus voltage (I-V) scan. Scans were made under both illuminated and dark conditions with an  $\approx 2.0\text{-}\mu\text{m}$  FWHM spot near the center of the detector gap. Only a positive voltage scan is taken since the detectors, being back-to-back diodes, should be symmetrical to a change in bias polarity. A cursory check of the electrical symmetry is made and any detector that is not symmetrical to a change in polarity is discarded. Then, the current versus bias-voltage curve is taken. At each bias, the detector is illuminated by the local oscillator and the induced photocurrent is measured. The dark current at this bias is also measured. The d.c. responsivity of the detector is calculated by subtracting the dark current from the photocurrent and then dividing the remainder by  $P_{LO}$ . The d.c. quantum efficiency is determined by multiplying the d.c. responsivity by  $\hbar\omega_{LO}/q = 3.71$ , where  $\hbar\omega_{LO}$  is the photon energy for 334.5 nm light and  $q$  is the unit of charge. The NEP (noise-equivalent power) of the detector is calculated by dividing the dark current by the d.c. responsivity. The d.c. quantum efficiency, NEP, and dark current, are recorded for each bias. The biases used range from near zero to a near maximum value of

$$V_{MAX} = (10^5 \text{ V/cm})(2x_G). \quad (91)$$

where  $10^5 \text{ V/cm}$  is the magnitude of the electric field for the onset of avalanche breakdown, and  $2x_G$  is the electrode gap spacing. Now, from Chapter II, it is known that  $V_{MAX}$  is above the maximum bias needed for

avalanche breakdown. The onset of avalanche breakdown is easily seen as an increase in the slope of the dark current curve. The bias for each detector was increased until the onset of avalanche breakdown was unmistakable. This was always at a bias less than  $V_{MAX}$ , and was near the maximum bias predicted in Chapter II for non-avalanche breakdown. These curves are discussed in more detail later.

After the d.c. I-V characteristics were determined for a detector, a frequency response,  $R(\omega)$ , was measured for three different biases. The 2.0- $\mu\text{m}$  FWHM spot was again positioned near the detector center, and its position recorded.  $R(\omega)$  was measured from 1-MHz to 10-GHz with four separate, but overlapping, frequency scans. The dye laser was set to slightly overscan each of the four frequency ranges. This overscanning was needed to insure that there was some overlap between each frequency range. Since each frequency range used a separate amplifier, it is important that there be some overlap between the ranges in order to determine that nothing has changed between scans. Unfortunately, the overscanning of the dye laser had one drawback, while the beatnote is outside of the set frequency range, the rf-spectrum analyzer kept on taking data, recording the noise floor of the amplifier as data, resulting in data dropouts in the scan. The large signal-to-noise ratio of the data, however, makes these data dropouts easily seen and removed. The data was reduced to give  $R(\omega)$  by first dividing out the gain versus frequency of the electronics. (see Chapter III) Then the amplifier compensated data was used to calculate  $R(\omega)$  as given by Eqn 20 in Chapter II. The data drop outs from the overscanning of the dye laser were then removed and a 7-point averaging was used to slightly smooth the data.

The three voltages used,  $V_1$ ,  $V_2$ , and  $V_3$ , were picked from the results of the I-V curve data.  $V_3$ , the largest, was always near, but always below, the bias where the onset of avalanche breakdown was first observed. The lowest,  $V_1$ , was near the lower limit for constant drift velocity operation as described in Chapter II. The third bias,  $V_2$ , was picked to be approximately midway between  $V_3$  and  $V_1$ .

Having measured  $R(\omega)$  versus bias, the charge in  $R(\omega)$  versus position is measured next. As predicted in Chapter II, the most substantial change in  $R(\omega)$  with position was observed at the lower biases. Hence, for all of the position studies, the bias was set at  $V_1$ .  $R(\omega)$  was measured at three positions,  $x_-$ ,  $x_0$ , and  $x_+$ . The  $x_0$  position was always the center position used for the two previously described experiments.  $x_-$  was the position of maximum response for an  $\approx 9$ -GHz beatnote, while  $x_+$  was sufficiently far enough away from  $x_0$  to give a discernable change in the 9-GHz response. Defining the center of the gap as  $x = 0$ , a positive position on the micropositioner moves the beam closer to the anode and a negative value positions the beam nearer the cathode. As with the  $R(\omega)$  versus Bias data, the  $R(\omega)$  versus position was then calculated.

The final data set taken was to map out the responsivity of the detector surface at three different bias conditions. Maps of the d.c., 1-GHz, 5-GHz, and 9-GHz responses were made at each bias. A map consists of an  $40 \times 40$  grid of data points with a  $2.0\text{-}\mu\text{m}$  data point separation. The responsivity was calculated and displayed on a three dimensional plot with the third axis being the responsivity at the given  $x, y$  coordinate. Contour plots of the map were also made. The three

biases used for the maps were the same as used in determining the  $R(\omega)$  versus Bias curves.

### C. Data Fitting

The  $R(\omega)$  calculated from the heterodyne measurements is now fit to the model of Chapter II by a "downhill simplex" method.<sup>1</sup> The "downhill simplex" method is a relatively simple data fitting routine that can handle up to 10 variables simultaneously. The routine attempts to minimize the residual error between the supplied data set and a parameterized mathematical model by a number of simple iterations. The simplex method is one where, for  $n$  variables, a  $n + 1$  simplex is defined. The vertice of the simplex with the largest residual error, and therefore worst fit, is moved with respect to the geometric center of the simplex. The vertice is moved in a set pattern about the line connecting it with the geometric center of the simplex until a position of lower residual error is found. Once a new position for the vertice is found, the residual error of all the vertices are compared and the vertice of the new simplex with the worst residual error is again moved. Each vertice represents a given set of the  $n$  variables. While a move of a vertice may indeed lower the residual error of the model to the data, there is no guarantee that the new position will have all of its variables closer to the true values. Thus, even though the routine moves a vertice of the simplex to get a better fit to the data, one of the variables may have a worse fit at this new position than at the old position. However, given a sufficient number of iterations the problem is overcome and the simplex will converge to an answer that minimizes the residual error between model and data.

As with most data fitting routines, the minimization of the residual error between model and data does not guarantee that this fit is the absolute best fit in a global sense. The routine just looks for a position of minimum error between model and data with respect to its local surroundings. To test for a local versus a global minimum, the data fitting routine must be run several times, with different starting parameters, to test if the same answer is always found at the end of the fitting procedure. This was accomplished by letting the simplex routine run for 400 iterations. It was found that after 400 iterations, the simplex routine typically had converged to the best fit it was going to find for that run. After a run, the value of the variables at the end of the data run was used to determine the values of the new variable points for the next run. The new data points were calculated by multiplying the old data points by a random number close to unity. The deviation from unity was decreased for each successive run. Thus, as the number of full fits performed by the simplex routine increased, the amount of randomization decreased. This is necessary in the event that a local minimum is close to the global minimum. At some point, depending upon the separation between the two minima, the randomization of the variables will not be enough to start the simplex outside of the global minimum valley and thus a local minimum will not be encountered by the simplex routine. The 1-MHz to 10-GHz  $R(\omega)$  data set was fit to the model in two steps. The existence of low-frequency gain in msm devices is well known and not modeled by the theory in Chapter II. To avoid this low-frequency gain, the theoretical responsivity, given by Equation 82 in Chapter II, was fit to the 5 to 10-GHz subset of the data. It was assumed that the low-frequency gain mechanism in the msm

devices was sufficiently small at these frequencies so as to be neglected. The existence of the inductance in the rf-microwave package was taken into account, since it appears that this will be the major contributor to the roll off of the data. The relationship between the responsivity of the detector,  $R_d(\omega)$ , and the actual responsivity,  $R_a(\omega)$ , which includes the effects of the rf package is given by,

$$R_a(\omega) = \frac{R_d(\omega)}{1 + i\omega(L/R)} \quad (92)$$

where  $L$  is the inductance of the rf package and  $R$  is the 50- $\Omega$  termination resistor of the rf amplifier. First, the high-frequency fit (5 to 10-GHz) was performed on all of the  $R_a(\omega)$  versus Bias data. Bulk values for drift velocities, diffusion constants, and minority carrier lifetimes were used for the model. The assumed position of the beam on the detector was also used, as was a 2.0- $\mu\text{m}$  FWHM Gaussian beam. The data fitting routine then determined the -3 db point in frequency of the rf package and the overall amplitude constant that best fit the data. The average of the -3 db points was taken to calculate the inductance of the bonding wire for that detector. This average inductance for a given detector was then used in the fitting of all the  $R(\omega)$  versus position data for that detector. The drift velocities, diffusion constants, and minority carrier lifetimes were set to their values, for the given bias, tabulated by Sze<sup>2</sup>. The -3 db point of the package was set to the average value previously determined. The data fitting routine then varied the overall amplitude constant and beam position of the 2.0- $\mu\text{m}$  FWHM spot on the detector to arrive at a best fit. The fitted values of the beam position to the known beam position for the  $R(\omega)$  versus

position data sets is then checked. Self consistency between the total amount of beam translation in the experiment and the total amount of beam translation found by the data fit was taken as an indication of a proper fit to the data by the model. The total distance moved by the beam across the detector is used instead of the actual values for  $x_+$  and  $x_-$ , since it is not known that  $x = 0$  lies precisely in the middle of the gap.

Once a self-consistent fit is found to the high-frequency data, the entire data set is fit to the sum of the high-frequency model and a low-frequency simple pole. The values of the variables for the high-frequency model portion for this full data fit is taken from the high-frequency data fits. The simplex routine then determines the value of the low-frequency pole amplitude and -3 db point in frequency that will best fit the entire data set when added to the high-frequency model.

#### D. Saturation and Band Bending Test

In all of the derivations in Chapter II involving the current in a detector, the carrier drift velocities were assumed constant. Also, the large signal-to-noise ratio assumes that the detector can be driven hard enough, without saturating the detector, so that the shot noise from the d.c. photocurrent dominates the other noise sources. It was shown in the previous chapter that the shot noise could indeed be made to be the predominant noise source. However, the issue of whether or not the detector is saturated was not explored. Also, a calculation showed that the band bending due to the space charge of the photogenerated electrons and holes should be negligible. Experimental results proving that both band bending and saturation are not occurring is now presented.

A 4.5- $\mu\text{m}$  planar gap detector was used for this study. The planar geometry was chosen because it will be compared to the model in Chapter II, which cannot be done with the interdigitated detectors. The 4.5- $\mu\text{m}$  gap was chosen so that the most light could fall on the detector and that the electrons and holes could have the maximum separation before being collected by the electrodes. A 2.0- $\mu\text{m}$  FWHM spot size beam was located in the middle of the detector gap and the detector was biased at 10 V.  $R(\omega)$  was measured from 5-GHz to 10-GHz at three different local oscillator powers. The three curves are shown in Figure 25. The near parallel behavior of the three curves indicates that there is no band bending present in these detectors, even at this low bias. If band bending were present, the space charge field that produces the bending would oppose the applied electric field and the drift velocity of charge carriers would not be constant across the detector. The net effect of band bending would be to reduce the high speed responsivity of the detector at higher LO power levels. A linear fit to the data shows that the 0.743-mW, 0.376-mW, and 0.217-mW curves have slopes of -0.00108, -0.00129, and -0.00111 A/(W.GHz), respectively. The 0.376-mW curve shows the steepest slope while the other two are nearly identical. If band bending were a problem, then the slope of the 0.217-mW curve should be less than both of the higher power curves. Since this is not the case, it is concluded that band bending is not a factor for the present set of experiments.

Detector saturation would be exhibited as a sublinear responsivity as a function of the incident power. The reader is reminded that the

responsivity is given by

$$R(\omega) = \frac{i(\omega)}{(2P_{LO}P_S)^{1/2}} \quad (93)$$

where  $i(\omega)$  is the current out of the detector and  $(2P_{LO}P_S)^{1/2}$  is the heterodyne power incident upon the detector. Consequently, if the detector photocurrent is linear with incident power, then the responsivity is not a function of incident power. The three curves in Figure 25 show that the responsivity is independent of incident beam power. The d.c. intercepts of the three linear fits are 0.021, 0.022, 0.020 A/W with a standard deviation of 0.0020 A/W, going from high to low power, respectively. A saturation effect would be indicated by an increasing responsivity with decreasing power. This is clearly not the case. With over a factor of three difference in the incident power the d.c. intercepts do not change by more than one standard deviation. It is clearly seen that this detector's responsivity and frequency response are not functions of the incident power. Since the smaller, 3.0 and 1.0- $\mu\text{m}$ , detectors collect less light than the 4.5- $\mu\text{m}$  detector, it can be reasonably assumed that these smaller detectors will also not suffer saturation and/or band bending effects.

#### E. DC current versus voltage results

The results of the d.c. current versus bias, or I-V, measurements are now presented. The dark current and d.c. quantum efficiency are plotted versus bias for all six msm detectors tested. The I-V curves for the three interdigitated detectors are shown in Figure 26. The dark current for all three detectors follows similar behavior in that it is

very low and relatively constant with bias until some threshold bias is reached. At this threshold bias, the dark current increases nonlinearly with bias, probably due to the onset of avalanche breakdown. This will be discussed more fully later in conjunction with the planar gap I-V curve results. The d.c. quantum efficiency shows some similarities between all three of the interdigitated detectors. All three detectors exhibit a region of near linear increase in the d.c. quantum efficiency with increasing bias. The 3.0 and 1.0- $\mu\text{m}$  detectors show that this linear region extends down to 0-V bias. The 4.5- $\mu\text{m}$  device shows a distinct turn on behavior with the linear region starting as low as 1.0-V Bias. A slight hint of this turning on behavior may be seen in the 3.0- $\mu\text{m}$  detector below 0.5 V, but it is so small as to be almost negligible. The 4.5- $\mu\text{m}$  and 3.0- $\mu\text{m}$  detectors also show a definite break in the d.c. quantum efficiency at higher biases occurring at the same bias as the dark current starts its rapid increase. At, or very near, to the avalanche breakdown voltage derived in Chapter II, the d.c. quantum efficiency sharply decreases in the two larger detectors. It was observed that at these biases the dark current was a major portion of the total d.c. photocurrent, hence reducing the quantum efficiency. The 1.0- $\mu\text{m}$  detector, however, did not exhibit any of these nonlinear behaviors in its d.c. quantum efficiency. The maximum applied field to this detector was the same as for the other two, therefore a lack of field strength was not the reason that this behavior was not seen.

The I-V characteristics for the planar gap detectors are shown in Figure 27. Many similarities with the interdigitated detectors are clearly seen. The dark current for the 4.5 and 3.0- $\mu\text{m}$  planar gap device shows the same behavior as their interdigitated counterparts. The break

in the dark I-V curve occurs at approximately the same bias for interdigitated and planar gap devices. The 4.5- $\mu\text{m}$  device shows the probable onset of avalanche breakdown at about 30 to 35 volts. This is, as previously mentioned, seen as the sharp, nonlinear, increase in the dark current with bias. The onset of avalanche breakdown in 3.0- $\mu\text{m}$  gap detectors, both planar and interdigitated, is seen to occur around 24 to 25 volts. These threshold biases for the onset of avalanche breakdown are somewhat below the 42-V and 29-V biases for the onset of avalanche breakdown computed in Chapter II for a 4.5- $\mu\text{m}$  and 3.0- $\mu\text{m}$  gap device, respectively. A possible reason for this is the presence of the sharp corners on the electrodes for these detectors. It is well known that the field around a sharp corner, similar to a lightning rod, is much higher than around a planar region. Thus, the fields around these corners will reach the  $10^5$ -V/cm threshold for avalanche breakdown at a lower bias than would a set of parallel electrodes, with no corners. The quantum efficiency of the planar 4.5 and 3.0- $\mu\text{m}$  gap devices show similar behavior with bias. Both the interdigitated and planar gap devices show a region of turn on at low biases. This turn-on region is more easily seen in the planar gap detectors than for the interdigitated ones. This result could again be due to the presence of the corners in the electrodes. By design, the interdigitated detectors have many more corners than do the planar detectors. Therefore, the average field inside the detector will be higher for the interdigitated than for planar detectors of the same gap dimension and at the same bias. Both types of detectors exhibit a region of nearly flat d.c. quantum efficiency with a decrease in the quantum efficiency roughly correlated with the bias where the dark current starts to increase. The decrease

in the d.c. quantum efficiency seen in the interdigitated detectors was not detected in the planar gap detectors over the bias range investigated. The reason for this is the maximum bias applied to the planar detectors was that which the peak d.c. quantum efficiency was observed in the interdigitated detectors. The planar detectors were not biased any higher because the dark current was so large at this bias, that the possibility of burning out the detector appeared to be very good if the voltage was increased further. In fact, for the 4.5 and 3.0- $\mu\text{m}$  detectors, it was seen that the planar gap detectors had significantly larger dark currents than their interdigitated counterparts at any given bias. Leakage currents in diodes should scale linearly with the diode area, assuming a constant leakage current density. The interdigitated detectors have less Ni-Si contact area than their planar counterparts. Yet the change in area between the planar and interdigitated is not sufficient to account for this discrepancy. This result is not fully understood.

A notable exception to all of the above is the 1.0- $\mu\text{m}$  gap detectors. Both the planar and interdigitated detectors showed a linear increase with bias in their respective d.c. quantum efficiencies, starting at 0-V bias. The interdigitated detector maintained this linear region out to 10-V bias, where avalanche breakdown should occur. The quantum efficiency of the planar detector increased linearly to a bias of 1.25 V and then remained constant with further increases in bias. The dark current in the 1.0- $\mu\text{m}$  interdigitated detector followed a behavior similar to the larger gap devices. A region of low dark current was observed, with a rapid increase in dark current, presumably the onset of avalanche breakdown, starting about 4.5 to 5-V bias.

Notable, though, is that the d.c. quantum efficiency continues to rise linearly with bias out to 10 V and does not decrease as it does for the 4.5- $\mu\text{m}$  and 3.0- $\mu\text{m}$  gap detectors. The 1.0- $\mu\text{m}$  detector was not biased beyond 2.0 volts because a problem with burning out these detectors at higher biases was encountered.

One consistent result between all the detectors is that at a given bias, the interdigitated detectors had a lower dark current than their planar gap counterparts. This result is totally unexpected. All detector types are processed on the same chip at the same time, hence the same conditions. The presence of more sharp corners on the interdigitated detectors would lead one to believe that these detectors should have more leakage than the planar gap devices. This result is also not understood at this time. More measurements of the I-V characteristics of these detectors are presented by S. F. Soares<sup>3</sup> in his dissertation.

#### F. $R(\omega)$ versus Bias and Beam Position for Planar Geometry Detectors.

The frequency response,  $R(\omega)$ , of a 4.5- $\mu\text{m}$  planar gap detector was studied extensively. The theoretical predictions in Chapter II show that changes in  $R(\omega)$  with respect to bias and beam position will be the greatest for this detector. Several bias voltages and beam positions, summarized in Table 7. Scans from d.c. to 10 GHz were made at all of the different bias-beam position combinations.

The 9, 12, and 15-V scans were used to determine the value of the inductance of the bonding wire on the rf microstrip package. The beam position and carrier drift velocities were fixed in the data fitting routine. The routine then found the best combination of amplitude and

3 db point to fit the 5-10-GHz range of the data. The -3 db point was found to be  $6.62 \pm 1.0$  GHz. The actual total impedance of the circuit is unknown due to the uncertainty in measuring the resistance of the detector. Therefore, assuming a  $50\text{-}\Omega$  termination load, the value of the induction was determined to be 1.20 nH, which is consistent with a piece of wire 1-2 mm in length. The package bandwidths found for each data run are listed with Figure 28. The increasing package bandwidth with increasing bias for this detector is not significant and did not occur with the other detectors.

With the effect of the inductor known, the remaining bias-beam position scans were fitted to the theory with the -3 db point for the rf-package fixed. The fitting routine adjusted the amplitude and beam position for the best fit of the theory to the data. Again, the drift velocities of the carriers were fixed to the bulk values for the average applied field. The fitted parameters are compared to the expected values in Table 8. At first glance, the fitted values do not appear to agree with the expected values. Remember, as seen in Chapter II, at high biases, the difference in the slope of the theoretical curves in the 5 to 10-GHz frequency range is very small with respect to changes in beam position. Also, even at lower biases, as the beam approaches the cathode, denoted by  $x < 0$ , the difference in  $R(\omega)$  with respect to changes in beam position is very small. These trends are clearly seen in the fitted data. At the lowest bias, 7.5 V, the best agreement between theory and data is seen. The two 7.5-V, 0.8- $\mu\text{m}$  bias beam combination scans show good agreement, with the position being off only 0.2- $\mu\text{m}$  between best theoretical fit and the assumed known value. The 7.5-V, -1.7- $\mu\text{m}$ , and 1.8- $\mu\text{m}$  bias-beam position combinations do not appear

to be that good. Yet notice that the total distance that the detector was known to be translated was  $2.5 \mu\text{m}$ . The theoretical fit indicates that the beam was translated a total of  $2.66 \mu\text{m}$ , which is in very good agreement with the known values. A rather large discrepancy between the expected and theoretically fitted values for the beam position is seen in the 25 and 40-V data. This is not unexpected, since again at the higher biases, the discrimination in beam position is very weak. Given that the  $R(\omega)$  curves are very nearly identical at high biases, it is easy to see that the data fitting routine could choose any value in its allowed range. It is noted that when there is a range of parameters, that will equally fit the data, the simplex routine will always move to the largest. By doing this, the routine thinks it is reducing the total error between theory and data since for a given error, the ratio of error to fitted value is smallest for the largest acceptable value. The simplex routine uses this ratio to break ties between two parameters that give an equal residual error between the data and theory.

Problems with discriminating between data sets were more evident with the smaller,  $3.0\text{-}\mu\text{m}$  gap detector. With this detector five  $R(\omega)$  scans, all at  $x = 0.8 \mu\text{m}$ , and with biases of 3, 15, and 27 V were used to determine the inductance of the rf-package. A -3 db point of  $4.71 \pm 1.6 \text{ GHz}$  was found for the rf-package, which implies an inductance of  $1.69 \text{ nH}$ . With this -3 db point, the  $R(\omega)$  versus beam position data was compared to theory. The detector was biased at 3 V for all of the position sensitivity scans. The positions used were -1.0, 0.8, and  $+1.8 \mu\text{m}$ , and again  $x < 0$  indicates the cathode side of the detector. For this data reduction run, the drift velocities and -3 db point of the rf-package were fixed and the fitting routine varied the amplitude and

beam position to achieve a best fit. The results were inconclusive. The fitting routine could not discriminate between any of the data sets, even though the beam was moved a total of  $2.8 \mu\text{m}$  on a  $3.0\text{-}\mu\text{m}$  detector. Consider the 5-10-GHz range graph for a  $3\text{-}\mu\text{m}$  detector shown in Chapter II (Fig. 12). It is seen that very little difference exists between the three curves, even though the beam is moved considerably. In this respect, the theory agrees with the data, and the fitting routine consistently chose the large position value of approximately  $+1.2 \mu\text{m}$ . As a self consistency check, a second data fitting run was performed on the above six data sets. This time, however, all of the parameters were allowed to vary. The results are listed in Table 9. The only restriction in this data fitting routine was that the hole drift velocity was tied to the electron drift velocity such that the relationship between the two was the same as that in bulk material. Doing this, and letting all parameters vary, a reproducible set of drift velocities and -3 db points was obtained. The expected drift velocity for electrons and holes under this bias was  $7.2 \times 10^6$  and  $4.3 \times 10^6$  cm/sec, respectively. This is in very good agreement with the fit. Also, the six -3 db rf-package points are also in good agreement with the 4.71-GHz average value obtained previously. The only discrepancy between the theoretical fits and the experiment is in the value of beam center,  $x_0$ . The values of  $x_0$  in the experiment varied from  $-1.0$  to  $+1.8 \mu\text{m}$ , but the fitting routine homed in on  $1.4 \mu\text{m}$  five out of six times. However, the nearly identical theoretical  $R(\omega)$  curves for this detector as a function of position indicates that the data fitting routine would, and did, have trouble finding any difference, and again, given a range of acceptable values, the largest values are chosen.

The problems with the 4.5- $\mu\text{m}$  and 3.0- $\mu\text{m}$  data fits were expected to be even more prevalent in the 1.0- $\mu\text{m}$  detector. Hence, only a total of six scans were taken. The first three scans again were used to determine the inductance of the rf microstrip bonding wire. A -3 db point of  $8.41 \pm 0.95$  GHz was found for this package implying that the inductance for this bonding wire was 0.946 nH. However, the  $R(\omega)$  versus position fits were not as inconclusive as expected. The beam was positioned at x values of -0.5, 0.0, and +0.5  $\mu\text{m}$  on the detector. The values of x returned by the fitting routine were +0.195, 1.5, and 1.46  $\mu\text{m}$ , respectively. Again, it is seen that for the beam on the cathode side of the detector discrimination between different beam positions is inconclusive. However, the fitting routine could discern a difference in the -0.5- $\mu\text{m}$  data. This is somewhat surprising in that the same procedures failed to find any distinction in similar scans for the 3.0- $\mu\text{m}$  detector.

There are three explanations as to why the data from the 3.0- $\mu\text{m}$  detector is so identical as to block any changes in  $R(\omega)$  with respect to beam position but not the 1.0- $\mu\text{m}$  detector.

First, the value of the bonding wire inductance for the 3.0- $\mu\text{m}$  detector, resulting in a 4.71-GHz pole, is the largest of the three detectors. The amount of inductance present in any given package is a quasi-random value since the bonding wire lengths were not constant from detector to detector. This high inductance for the 3.0- $\mu\text{m}$  detector dominates the  $R(\omega)$  roll-off in the 5-10-GHz range. The relatively small changes in  $R(\omega)$ , due to changes in the beam position, are easily lost in the single pole roll-off due to the 4.71-GHz pole from the bonding wire inductance. The bonding wires on the 4.5 and 1.0- $\mu\text{m}$  detector both have

considerably lower inductance than on the 3.0- $\mu\text{m}$  detector. The 1.0  $\mu\text{m}$  has the lowest inductance, 0.946 nH, which means that the behavior of  $R(\omega)$  in the 5-10-GHz band is not entirely dominated by the  $L/R$  inductance roll-off. The second factor that enhances the changes in  $R(\omega)$  with position is the low bias on this detector. Since the "flat band" voltage scales as the square of the gap width, the very low flat band bias condition of the 1.0- $\mu\text{m}$  detector means that  $V$  does not have to be very large to achieve a constant drift velocity. Couple this with the fact that the  $\mathbf{E}$ -field scales linearly with the gap width, for a given bias, then much lower, but still constant, drift velocities can be obtained in the 1.0- $\mu\text{m}$  detector than either of the other two. For example, the "flat band" voltage for the 4.5- $\mu\text{m}$  and 1.0- $\mu\text{m}$  detector is 3.24 V and 0.16 V, respectively. To achieve a nearly constant drift velocity across the gap region a bias of approximately twice  $V_{\text{FB}}$  is needed. Hence, the drift velocity for electrons at two times  $V_{\text{FB}}$  is approximately 4.5 times slower in the 1.0- $\mu\text{m}$  device than in the 4.5- $\mu\text{m}$  device. Thus, the 0.5-V bias on the 1.0- $\mu\text{m}$  detector provides the slowest "constant" velocity of the charges of any of the detectors. Finally, the set-up procedure for the 1.0- $\mu\text{m}$  detector was somewhat suspect. Procedurally, the  $x = 0$  position is defined as the point where the d.c. short circuit photocurrent is zero. This normally well defined point on the 4.5- $\mu\text{m}$  and 3.0- $\mu\text{m}$  detectors was much less distinct in the 1.0- $\mu\text{m}$  detector. The best that the detector could be positioned was  $\pm 0.3 \mu\text{m}$ . With this large an uncertainty on a small detector, it is very likely that at some point the center of the beam was off of the detector, and hence the only illumination was from the wings of the beam. This is the most likely explanation why some position sensitivity

was seen in the 1.0- $\mu\text{m}$  detector. Even though, as with the 4.5- $\mu\text{m}$  detector, the total beam motion of 1.0  $\mu\text{m}$  was very close to the fitted value of 1.33  $\mu\text{m}$ , the problems with the uncertainty in the initial position make this result suspect.

In conclusion, the detector response model derived in Chapter II has been compared with experimental data. Frequency response measurements for three detectors were made under a variety of beam positions on the detector and detector bias. The theoretical fit of the data revealed some discrepancy between the nominal beam positions and those derived from fitting the experimental data to the model. Good agreement in the magnitude of the total beam displacement across the detectors was found with the 4.5- $\mu\text{m}$  and 1.0- $\mu\text{m}$  detectors. The fact that the bonding wire inductance was lower for these two detectors probably accounts for the differences that can be seen in their position data. Had the inductance been greater, then the L/R roll-off of the package would have dominated the data and washed out any change in  $R(\omega)$  with beam position, as it did with the 3.0- $\mu\text{m}$  detector. The major conclusion of this section is that any real knowledge of detector performance has been washed by the inductance of the rf-package. Since this packaging technique is widely used, it is also concluded that other reported results may suffer from the same L/R limitation as seen here. Some of the researchers using this packaging technique insure that they use as short a bonding wire as possible, hence reducing the L/R roll-off to a minimum. However, other researchers use bonding wires as long as the ones used here, and therefore they must also suffer from the same L/R limitations. It is pointed out that for a 1.5-nH inductance and a 50- $\Omega$  impedance, the FWHM pulse response would be 30.0 psec. This impulse

response is not that different from most reports in the literature. For detector-limited operation of the entire msm photodiode-rf-package system, the bonding wires must be eliminated completely. This implies a total redesign of detector rf-microstrip package, and has not been attempted. The success of the model in matching the known change in beam position is very encouraging. The method of determining the origin on the detectors, while extremely repeatable, has not had independent verification that the  $x = 0$  position is in the exact geometric center of the detector. Indeed, the results of the theoretical fits indicate that the defined position of  $x = 0$  is not truly in the geometric center of the gap, but should be more toward the cathode side. The exact reason for this offset is not known at this time. One conjecture is that the existence of a ground plane on one side of the detector and the rf microstrip on the other may slightly upset the balance of the two msm pads, hence skewing the short circuit position response results. The position sensitivity of this short circuit device is being studied further.

#### G. Performance of the 4.5- $\mu\text{m}$ Detector to 18 GHz.

In light of the theoretical predictions of detector performance, an 8 to 18-GHz amplifier was obtained. The amplifier circuit was calibrated in the same manner as the lower frequency circuits and  $R(\omega)$  as a function of bias was measured for 15 V. The beam was centered at nominal  $x = 0$ . The 15 V,  $x = 0$  data from 9 MHz to 10 GHz, and the new 8-18-GHz data are shown in Fig. 29. The jump in the data could be caused by any number of things (alignment, detector ageing) since several months elapsed between taking the two data sets. Translating

the 8-18 GHz curve up (approx. 1 db) to meet the old curve at 8 GHz, the data sets are seen to overlap nicely in the 8-10-GHz range. This strongly implies that if the entire scan, out to 18 GHz, was taken in one day, that the curves would all line up as they do for the data to 10 GHz. The data shows that the response of the detector-rf-microstrip package continues to drop off with frequency due to the domination of the response by the bonding-wire inductance. This simple pole response is subtracted from the data in Fig. 30. The theoretical detector response (from Chapter II) is also plotted here, with the parameters for drift velocity and beam position being taken from the 5-10-GHz fit of the previous section. Excellent agreement between theory and the compensated data is seen out to 14 GHz in frequency. The roll-off of the compensated data above 14 GHz is probably due to the SMA connector which has a -3 db point of 18 GHz. Including a simple 18-GHz pole in the theoretical curve does indeed match the data out to 18 GHz. Therefore, the indications are very strong that the theory of Chapter II does indeed predict the frequency response of the msm structure out to very high frequencies. Also, the inductance of the bonding wire is a major contributor to the frequency, and therefore time, response of any device packaged in this manner. Finally, and most interesting, it appears that a 15-20-GHz detector, with a 30% rf-quantum efficiency, could be made on bulk Si. All previously reported detectors with this high a frequency response were made on GaAs, InGaAs, etc., which all possess carriers with much higher mobilities and higher saturation velocities.

Given the success with the 4.5- $\mu\text{m}$  fit and assuming RC does not limit the response, a 75-GHz bandwidth, 1.0- $\mu\text{m}$  detector on bulk Si may

be feasible, as predicted in Chapter II. Another conclusion from this result is that the charge carriers are traveling at their respective bulk drift velocities. This is somewhat surprising since the charges are moving within  $0.2 \mu\text{m}$ , or less, of the crystal surface. It is well known that in GaAs the surface states reduce the mobility of carriers near the surface. It was thought that this mobility reduction would also be seen in Si. The above result seems to disprove this premise. A discernible change in  $R(\omega)$  can be seen for at most a 30% change in the carrier drift velocity. Possibly, the thin  $\text{SiO}_2$  layer that forms upon exposure to air sufficiently passivates the surface states. Confirmation that the charges near the surface are moving at their respective bulk drift velocities needs a redesigned rf-microstrip package that has a flat frequency response out to 18 GHz. This work is currently being pursued.

#### H. Full Bandwidth Analysis of Planar Gap Detectors

In the previous section, the high-frequency behavior of the planar gap detectors was compared to the theoretical model developed in Chapter II. As a reminder, the reason for only using the 5 to 10-GHz region of the data is the enhanced low-frequency gain of msm detectors. This low-frequency gain, which has yet to be satisfactorily explained, has been reported previously and is also seen on the detectors used in this study. One possible explanation for this gain mechanism is presented in Appendix I, but does not satisfactorily match the data and is not used here.

The low-frequency gain in these detectors is assumed, for this analysis, to be independent of the high-frequency characteristics of the

detectors. Thus, a linear superposition of the high-frequency response and the low-frequency gain mechanism is utilized to study the low-frequency behavior of the planar gap msm photodiodes. The low frequency portion of  $R(\omega)$  was isolated by subtracting the predicted high-frequency response, using the parameters found in the preceding section, from the data. The data-minus-high-frequency-model residual was then compared to a superposition of two-simple poles and a single-simple pole. The simplex routine was used to fit the amplitude and -3 db point for the poles to the residual data.

The two-pole fit to the low-frequency data gave inconsistent results between data sets. The single, simple-pole results were consistent between data sets and are presented here. The 4.5- $\mu\text{m}$  detector, due to its size relative to the beam spot, was studied extensively. The full set of fit parameters, both low and high frequency, for the 4.5- $\mu\text{m}$  detector are listed in Table 10 and the fitted data is shown in Figures 31 and 32. The 7.5<sup>1</sup>-V at 0.6- $\mu\text{m}$ , 25-V, and 40-V data sets were all taken on the same day. The 7.5<sup>2</sup>-V, at -0.41- $\mu\text{m}$ , +0.6- $\mu\text{m}$ , +2.25- $\mu\text{m}$  data sets were taken the following day. A comparison of the two +0.6- $\mu\text{m}$  7.5-V data sets show that there was a 3 db change in amplitudes, both low and high frequency, between the two data sets which is roughly consistent the observed  $\pm 1$  db variations in the calibration. The fact that both the low and high-frequency amplitudes are displaced by identical amounts indicates that this change is due to the system and not the detector.

The low-frequency response versus bias is now considered. The detector was positioned at near midgap, 0.6  $\mu\text{m}$ , and  $R(\omega)$  was measured at 7.5, 25, and 40 V. The high-frequency fit placed the position parameter

at  $2.25 \mu\text{m}$  for the 25-V and 40-V data. This is an artifact of the software, which as explained above always chooses the largest parameter among a range of equally good fits. Therefore, it is assumed that the beam was in reality at the same position as for the 7.5-V data taken on this day. By normalizing the -3 db point,  $f_p$ , to the 40-V data, the frequency response is compared to the hole drift velocity, also normalized to its 40-V value. The normalized results are shown in Table 11 and the data plotted in Figure 34. A similar comparison of the high and low-frequency amplitudes is also shown. Good agreement between the change with bias between the hole drift velocity and the frequency response of the simple pole is clearly seen. Again, it is clearly seen that the amplitude of the low-frequency pole is directly proportional to the amplitude of the high-frequency response. From these two comparisons it appears that the frequency response of the low-frequency pole is directly proportional to the hole drift velocity and transit time. The strong correlation between the amplitudes of the high and low-frequency mechanisms indicate that there is some relationship between them. If this low-frequency mechanism is related to photoconductive gain, as described in Appendix I, then this correlation in amplitude is expected. However, remember that a gain-bandwidth product correlation is not proper on a single detector. The constant gain-bandwidth product argument is only valid between two photoconductive detectors with different recombination times. A photoconductor's frequency response is fixed by the recombination time. Its gain, however, is not fixed, and is a function of the charge carrier drift velocity. For more details see Appendix I.

To test these correlations between the low and high-frequency mechanisms, the bias on the detector was set at 7.5 V and  $R(\omega)$  was measured at three different positions, -0.41, +0.6, +2.25  $\mu\text{m}$ . The -0.41- $\mu\text{m}$  beam position places the beam closer to the detector cathode, thus decreasing the hole transit time. Conversely, a positive position places the beam close to the anode, increasing the hole transit time. One would expect that  $f_p$  would be greatest when the beam is near to the cathode, if the hole transit time is truly the limiting factor. This is not the case. The peak of  $f_p$  is near the center and falls off as the beam is moved away from center.

The amplitude, however, still shows that somehow the holes are involved. This is seen in the gain of the high-frequency signal. By defining the gain as the ratio of the low-frequency amplitude to the high-frequency amplitude, several interesting facts can be seen. (Table 12) From Table 12 two facts relevant to the low-frequency gain mechanism can be noted. First, the gain decreases with increasing bias. Second, the gain increases as the transit time of the holes, at a given bias, increases. This would indicate that some sort of photoconductive gain may be present. That is, the longer the holes transit time, the higher the gain. This is consistent with a photoconductive gain mechanism. Carriers are generated and flow around the circuit until they recombine. Therefore, a single electron-hole pair could be counted more than once before the hole reaches the cathode and recombines. Hence, anything that keeps the hole around longer will increase the low-frequency gain. Note, that the 25-V data appears to be the sole contradiction to this statement. It is pointed out, however, that there

is only a 9% change in the hole drift velocity from the 40-V data. This small change could easily be lost in the system noise.

To test further this idea of the relationship between the transit time of the holes and the low-frequency response of MSM detectors, the 3.0 and 1.0- $\mu\text{m}$  detectors were tested in a similar fashion to the 4.5- $\mu\text{m}$  detector. However, the 1-500 MHz amplifier failed and no definitive results were obtained. The absence of the low-frequency range did cause problems in the low-frequency data fits. Without this range of frequencies, the amplitude of the low-frequency pole could not be seen. Remember, once a simple pole starts to roll-off, it keeps rolling off as  $1/f$ . Thus, a 100-MHz bandwidth pole looks just like a 300-MHz pole with lower amplitude when observed at 600 MHz and beyond. The location of the elbow in the roll-off of a simple pole is necessary for a proper data fit. It was hoped that, if the bandwidth of the simple pole was tied to the hole transit time, then by decreasing the detector electrode spacing, this pole could be seen at 400 MHz and beyond. However, attempts to fit the data with a simple pole resulted in wildly inconsistent results. This is due to the fact that the beginning of the roll-off could not be seen without the low-frequency amplifier (Fig. 33). Therefore, many combinations of amplitude and frequency would work equally well. Attempting to put an upper limit on the amplitude of the low-frequency pole, so as not to exceed the measured d.c. value, also failed. In this case, the fitting routine consistently pushed the amplitude to the maximum limit and did some very fine adjustments with the bandwidth.

The inability to detect the flat portion of the low-frequency pole on even the 1- $\mu\text{m}$  detector implies that transit time may not be the

limiting value to the low-frequency bandwidth. If the transit time was important, then the 1- $\mu\text{m}$  detector, having a smaller transit time at equal drift velocities over the 4.5- $\mu\text{m}$  detector, should have shown the flat portion of the low-frequency response easily at 400 MHz. Its absence suggests that, in light of the 4.5- $\mu\text{m}$  results, the hole drift velocity itself is the limiting value for this low-frequency behavior, not transit time. Obviously this low-frequency behavior needs to be investigated in much more detail than has been undertaken to date.

#### I. Planar versus Interdigitated Frequency Response

It was originally hoped that a direct comparison between the planar and interdigitated detectors could be made. The variability and dominance of the bonding wire inductance makes any direct comparison between any two different detectors very questionable. The only comparisons that can be made are relative changes within a given detector. These relative changes could, however, be compared between detectors, with the individual detector as its own reference. Since very similar results were obtained with all detector gap dimensions, only one detector pair will be studied here. For example, consider the  $R(\omega)$  data versus bias for the 4.5- $\mu\text{m}$  planar and interdigitated detectors (Fig. 35 and 36). Taking the 40-V response as a reference in both graphs, the change in  $R(\omega)$  with bias can be compared between the two detectors. Clearly, both detectors exhibit the same saturation effect above 25-V bias. However,  $R(\omega)$  for the planar detector decreases more rapidly with decreasing bias than does the interdigitated detector. The most probable explanation for this is that the additional corners on the interdigitated detector raises the average electric field strength

inside of the depletion region. Thus, the average drift velocity of the charge carriers is higher in the interdigitated device than in a planar device at the same bias.

Another manifestation of the higher average  $\mathbf{E}$ -field strength can be seen in the  $R(\omega)$  versus bias data. Figure 37 and 38 show the  $R(\omega)$  versus position data for the same detectors used above. Even though the interdigitated detector is at a lower bias, it is clearly seen that the change in  $R(\omega)$  with position is reduced relative to the planar detector. In terms of the model, this can only be explained by the interdigitated detector having a higher charge carrier drift velocity, and therefore a higher electric field, than the planar device.

Two conclusions can be drawn from this comparison. First, the interdigitated detectors can be operated at a lower bias than a planar detector and the drift velocities are still near saturation. Secondly, the interdigitated design is inherently less sensitive to beam position than the planar detector. This implies that the interdigitated detector has a larger, more uniform active area than the planar device. It would seem then, that in all respects the interdigitated detector geometry is a superior design to the planar gap.

#### J. Responsivity Maps

The final experiment performed on these detectors was to map the responsivity as a function of beam position. The response map of each detector was made under different biases at four different frequencies. The biases used were the same biases with which the  $R(\omega)$  data was taken. D.C., 1-GHz, 5-GHz, and 9-GHz response maps were made at each bias.

Many similarities are seen between all of the maps, hence only representative data will be shown.

As before, the data from one detector, the 3.0- $\mu\text{m}$  planar gap device, will be presented in detail. Then, select examples from other detectors will be presented in order to show that the response is similar. For all of the maps a 2.0  $\mu\text{m}$  FWHM spot was stepped by 2.0  $\mu\text{m}$  across the detector surface in a 40x40 array.

First, to be considered is the d.c. response map at 3.0 and 15 V for a 3.0- $\mu\text{m}$  planar detector. Figures 39, 40, and 41 shows the d.c. response map at 3.0 and 15 V. The z axis on the 3-d plots displays the value of the responsivity. Clearly the d.c. photoresponsive area is not confined to just the gap region. In fact, the contour plots of the 3.0-V, 3-D map, Figure 40, show that the peak response is actually outside of the gap region, located towards the cathode side of the detector and near the corners of the electrodes. The electrodes have been drawn to scale on Fig. 40. These areas of peak response near the electrode corners are not surprising, since this should be a region of very high electric-field strength. Peaks can be seen at both ends of the gap region, which is also expected. The skewing of the center of the peak toward the cathode side of the detector is thought to correspond to the balancing of the electron and hole current to produce a maximum. If the polarity of the detector is reversed, the peaks also switch sides. For even moderate biases, these peaks have d.c. quantum efficiencies in excess of 100%, reaching as high as 300% at high biases. The highest quantum efficiency on the 3.0- $\mu\text{m}$  gap detector, shown in Fig. 41, is 211% at 15-V bias. Moving further away from the gap region, the d.c. response decreases, but does not reach zero even 40- $\mu\text{m}$  away from

gap center. The long lifetime of the carriers in Si is the reason for this extended d.c. response area. The actual gap region of the detector is clearly seen as a narrow ridge spanning the two peaks. The d.c. response in the gap is smaller than at the peaks outside the gap region for two reasons. First, inside the gap the electric field is weaker as one moves away from the corners. Secondly, inside the gap the metal electrodes physically block some of the uv radiation from reaching the Si, therefore reducing the responsivity.

Other points of interest that are seen on the response maps, are holes in the bonding pads and a region of higher response closer to the edges of the bonding pads. The holes in the bonding pads are not intentional, but occasionally result from the bonding process tearing a hole in the contact pad. This tear exposes the Si providing direct access to the uv light. Again, due to the long lifetime of carriers in Si, a significant amount of d.c. photoresponse can be seen in these exposed areas. The area of higher response, with respect to its surroundings inside of a tear, is clearly seen on the left side of Fig. 39. The higher response at the edges of the bonding pads can also be seen in Fig. 39. The construction of the detectors is such that only the small  $20\text{-}\mu\text{m} \times 5\text{-}\mu\text{m}$  electrodes that form the actual gap region are in direct physical contact with the Si. The large  $75\text{-}\mu\text{m}$  square bonding pads are separated from the Si by a 100 nm thick  $\text{SiO}_2$  layer. The existence of this region of higher response is unexpected. It also appears in the rf response maps, even out to 9 GHz, as will be shown later. It is postulated that the carriers can tunnel through the  $\text{SiO}_2$  layer to the electrode if the  $\mathbf{E}$ -field is high, as it is around sharp

edges. A stronger field does increase this effect as seen in the 3-V and 15-V 3-D plots (Fig. 39 and 41).

Next, response maps were taken at 1 GHz. Figures 42, 43 and 44 shows the 1-GHz response map at 3 V and 15 V. The most notable change between d.c. and 1 GHz is that the responsive area is largely confined to the gap region and underneath the cathode. As with the d.c. response, very little rf signal is seen when the beam is on top of the anode. At 3-V bias, the 1-GHz responsive area extends only across the gap region and the cathode. A 15-V bias, a larger responsive region is seen. The additional responsive areas, over the 3-V case, coincide with a hole in the bonding pad and the edges of the bonding pad, as seen before in the d.c. data. The reduction in the photoresponsive area by going from d.c. to 1 GHz is assumed to be a time-of-flight limitation. That is, the carriers cannot reach a pad in time to be collected before the next rf cycle.

The time-of-flight limitation on the responsive area is corroborated further by the 9-GHz response maps (Figures 45-48). It is clearly seen on the 3-V contour maps for both 1 GHz and 9 GHz that the active area reduces in size as the frequency increases (Fig. 43 and 46). Increasing the bias will, at a given frequency, also increase the photoresponsive area as seen in Fig. 46 and 48. Again, as with the d.c. and 1-GHz response maps, the increase in active area with bias is seen mainly at the edges of the bonding pad. At first, the hole in the bonding pad also appears to have some responsivity at 9 GHz. Close inspection of this region, however, shows that the center of this hole is not responsive, with only the edges responding to the 9-GHz beatnote.

This area does not show up in the contour plot (Fig. 48) due to limitations in the plotting routine.

Identical behavior was observed with the 4.5 and 1.0- $\mu\text{m}$  devices. All of the planar gap detectors showed a thin ridge, confined to the gap region, spanning twin peaks of d.c. responsivity located near the corners of the cathode. The anode showed very little response when the uv beam was incident upon it, in contrast to the cathode. The response at the edges of the bonding pads was also seen, but to a lesser degree on the 1.0- $\mu\text{m}$  detectors. This is simply due to the bias not being as large as for the wider gap detectors. The most notable effect is that, at a constant bias, the photoresponsive area decreases with increasing frequency. The active area also increases with increasing bias at a constant frequency.

The response maps of the interdigitated detectors behaved much like their planar-gap counterparts. Contour plots of the d.c., 1-GHz, and 9-GHz response for a 3- $\mu\text{m}$  interdigitated detector at 3-V bias are shown in Fig. 49, 50, and 51, respectively. Fig. 52 and 53 are 1-GHz and 9 GHz contour maps taken at 15-V bias. The similarities between this 3.0- $\mu\text{m}$  gap interdigitated and its planar gap counterpart are easily seen. The gap region is clearly defined as it snakes through the electrodes in all of the plots. At d.c., the gap region is terminated by a region of high responsivity at both ends. The bonding pads are clearly outlined in the d.c. plot. Increasing the frequency to 1 GHz, the responsive area decreases from that at d.c. However, unlike the planar detectors, increasing the frequency to 9 GHz does not reduce the active area over the 1-GHz case, as long as the bias remains constant. But increasing the bias to 15 V does increase the 9-GHz responsive area

over the 3-V responsive area. Also, at 15 V, the responsive area outlining the bonding pad is again seen. Consistent with the 3-V results for this detector, the 1-GHz and 9-GHz responsive areas are the same.

Thus, the interdigitated detectors responsive area behaves in the same manner as does the planar detectors with the exception that, at constant bias, the responsive area does not shrink with increasing frequency. This fact may not be that surprising when the field structure inside of the interdigitated detectors is considered. With all of the sharp corners inherent in an interdigitated design, the  $E$ -field strength is going to be considerably higher, on average, than it would be in a simple planar device. This high-strength highly-convoluted field appears to keep the active area constant over a much wider range of frequencies than its planar device counterpart. These results for the interdigitated detectors were consistently observed for all three gap dimensions of interdigitated detectors.

#### K. GaAs Detector Results.

As mentioned in the introduction, GaAs msm photodiodes were also fabricated and tested. It was hoped that differences between the Si and GaAs response curves would further show the effects of material parameters on detector response. A GaAs msm photodetector was produced and placed in the uv heterodyne system for testing. It was found, however, that the d.c. and rf responsivity was not constant with time. Figure 54 shows the change in the d.c. responsivity over a period of about one hour. Clearly this degradation in the d.c. response is an undesirable feature. The d.c. response did not regenerate when the light was turned off, implying that the degradation was permanent. The

detector was further illuminated with approximately 700  $\mu\text{W}$  of cw uv light for 12 hours. The result was that even after 12 hours of constant illumination the responsivity was still decreasing. This shows that bare GaAs is not a suitable uv-detector material and is consistent with studies on degradation of the surface photoluminescence of GaAs<sup>4</sup>. In these experiments it was found that the surface photoluminescence of freshly cleaved GaAs decayed irreversibly with time under visible laser illumination. A possible mechanism for this degradation is photo-enhanced migration of surface defects into the bulk. This implies that some means, possibly a AlGaAs cap layer, must be found to keep the detector surface from degrading under uv illumination. Hence, no further test on GaAs detectors were performed.

Figure 25: Detector Saturation Test.

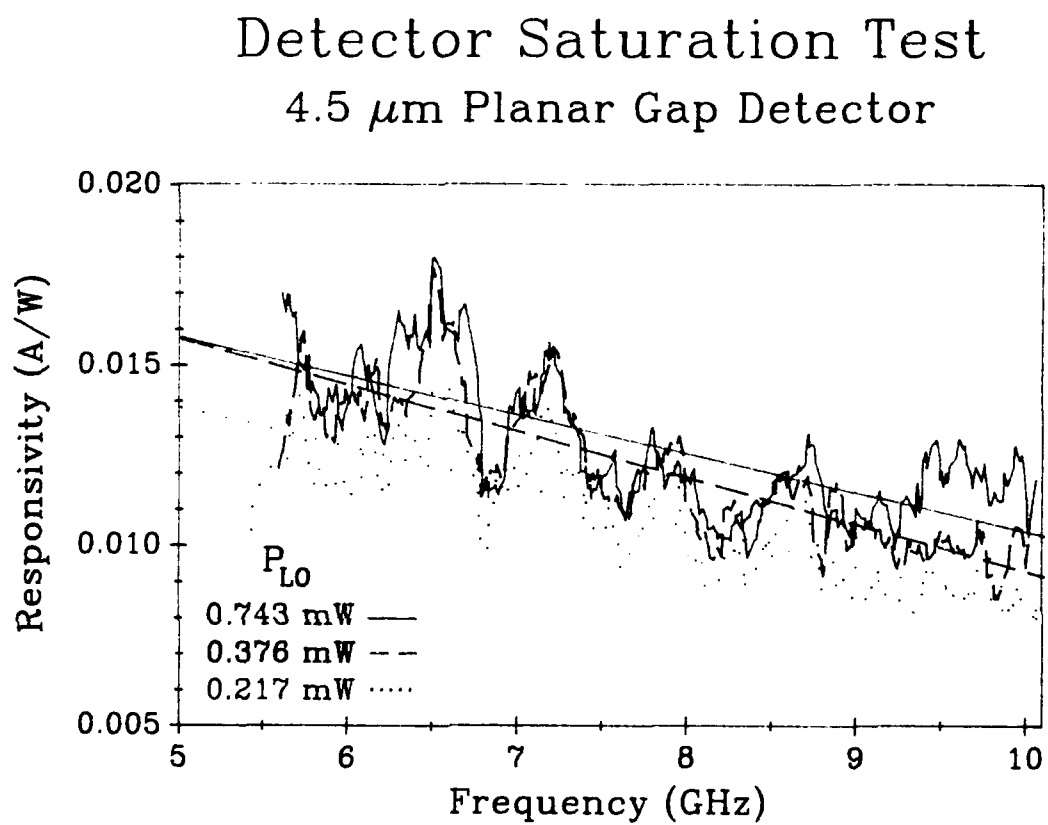


Figure 26: D.C Current-Voltage Characteristics for 4.5, 3.0 and 1.0- $\mu\text{m}$  Interdigitated Detectors.

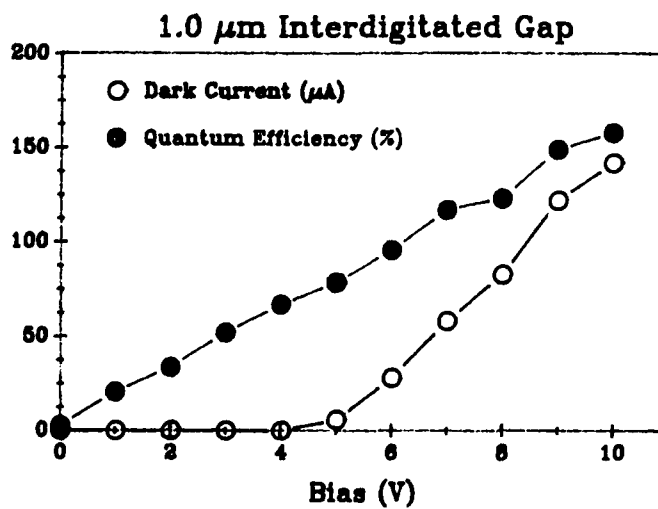
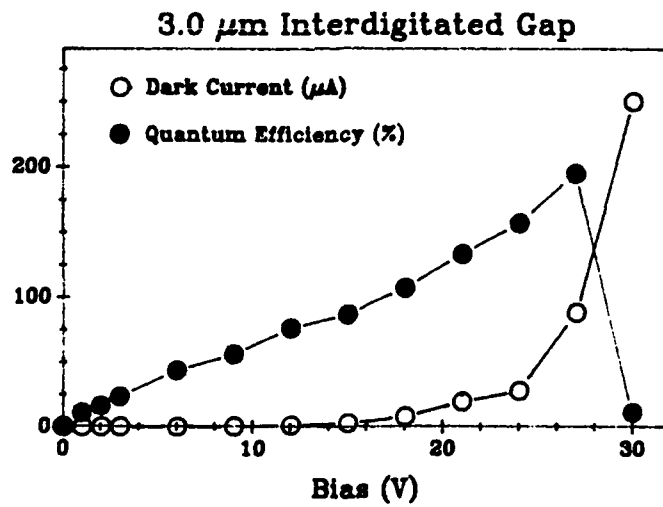
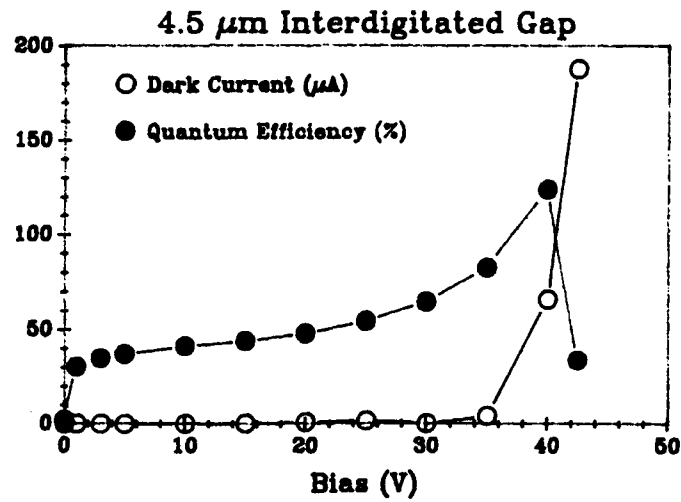


Figure 27: D.C Current-Voltage Characteristics for 4.5, 3.0 and 1.0- $\mu\text{m}$  Planar Detectors.

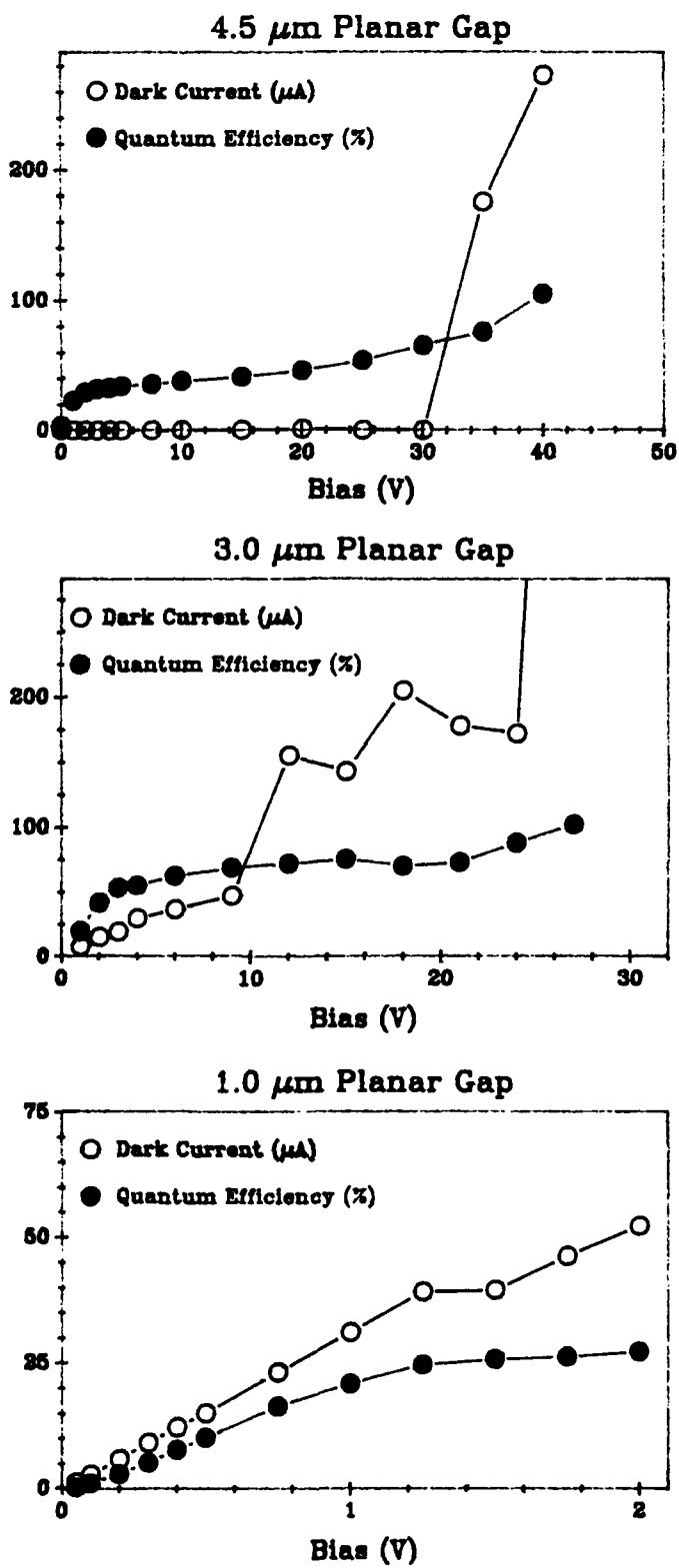
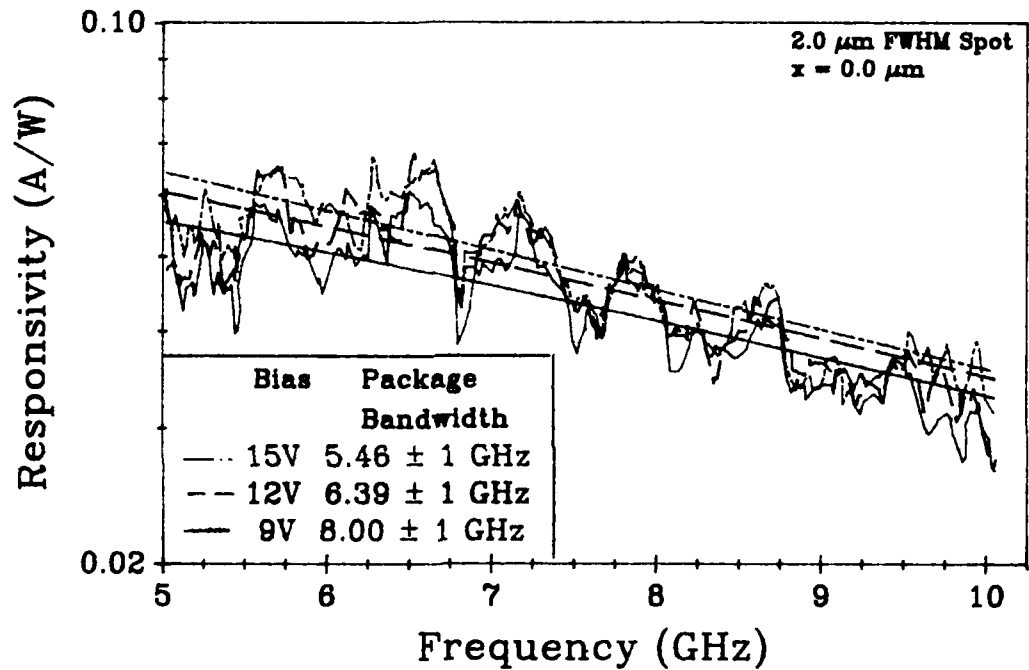


Figure 28: RF Package L/R Bandwidth Determination.

### High Frequency Fit to Determine RF Package L/R Bandwidth



4.5  $\mu\text{m}$  Planar Gap Device

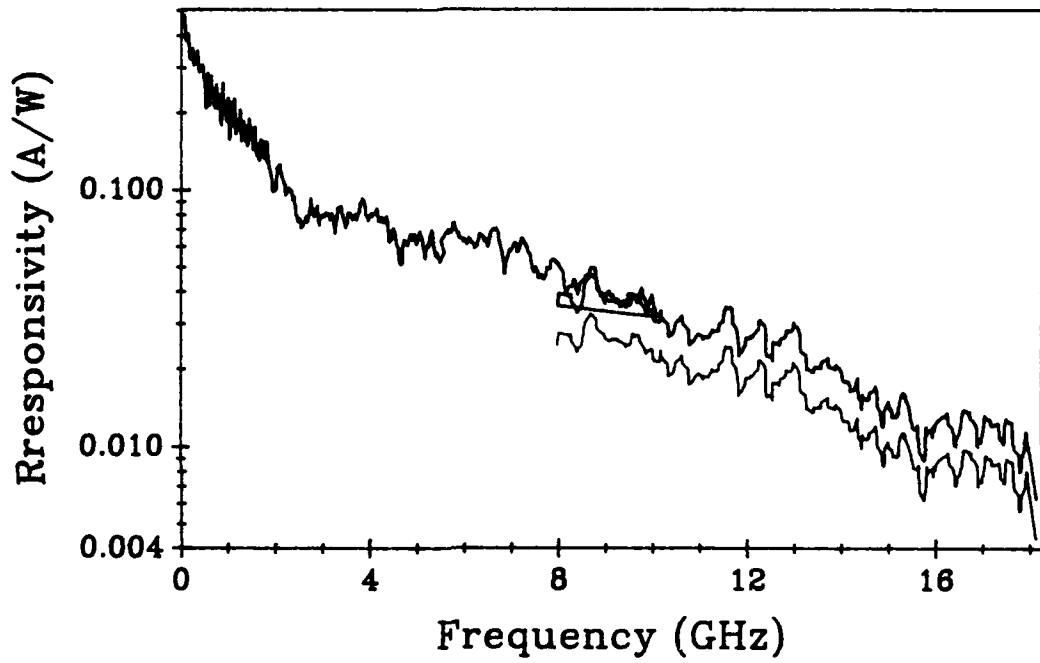
Figure 29: 4.5- $\mu\text{m}$  Planar Detector  $R(\omega)$  to 18 GHz.4.5  $\mu\text{m}$  Planar Detector

Figure 30: High-Frequency Model Fit to 18 GHz for a 4.5- $\mu\text{m}$  Planar Gap Detector.

### 4.5 $\mu\text{m}$ Planar Detector

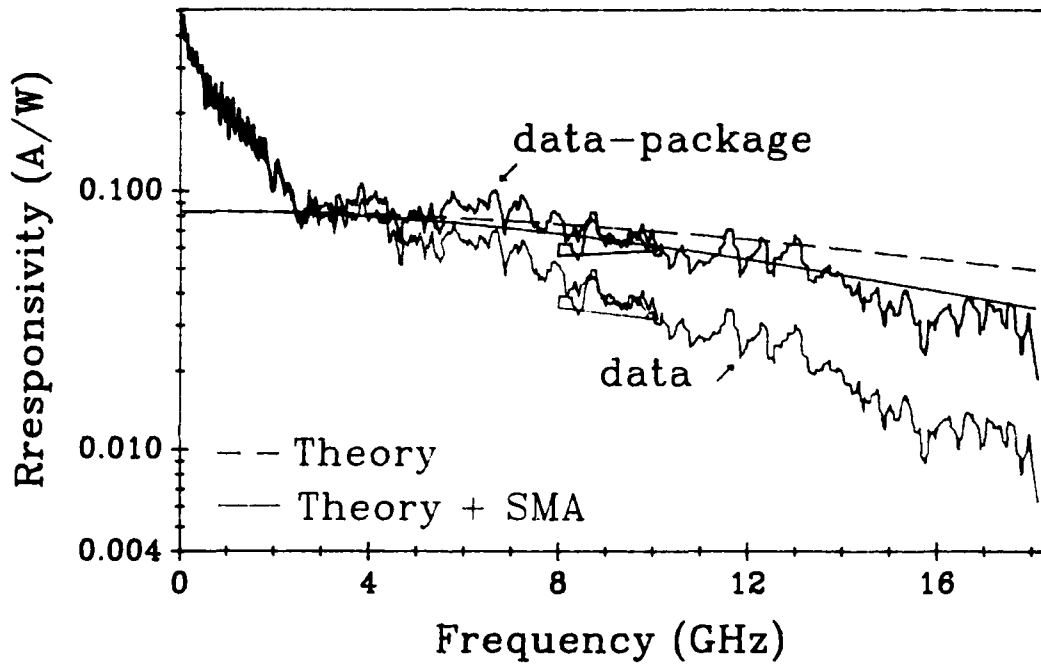


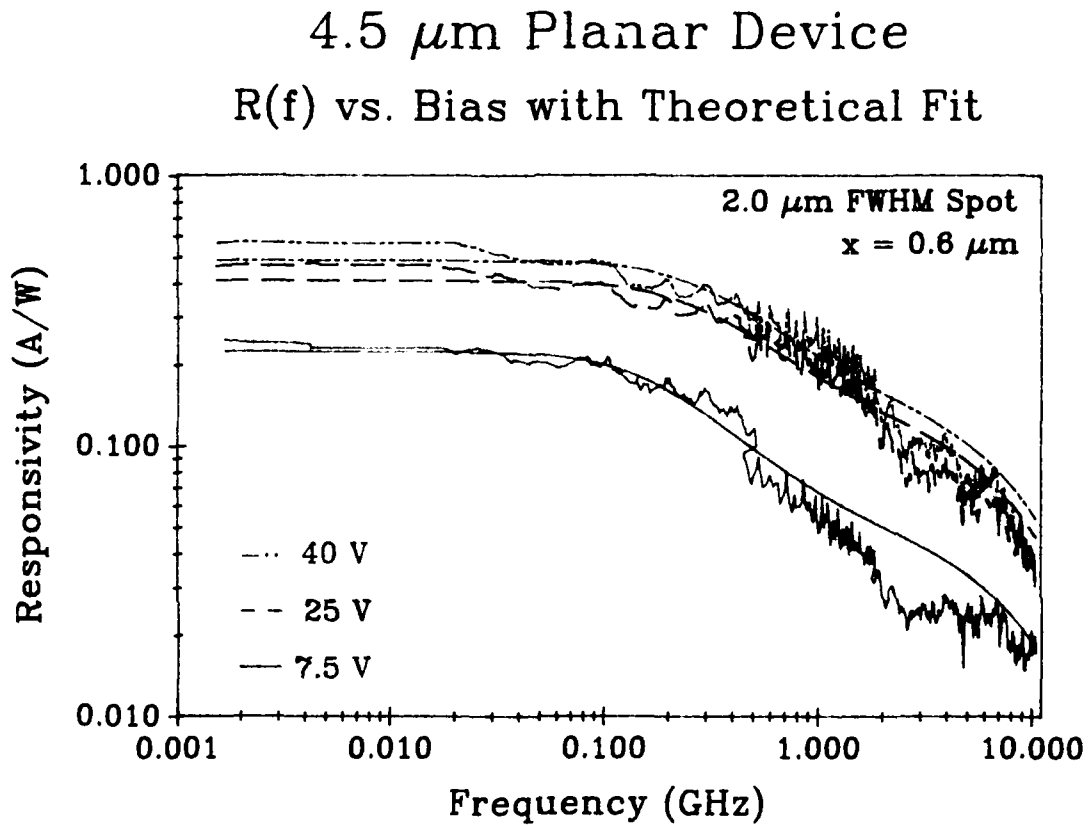
Figure 31:  $R(\omega)$  versus Bias for a 4.5- $\mu\text{m}$  Planar Gap Detector.

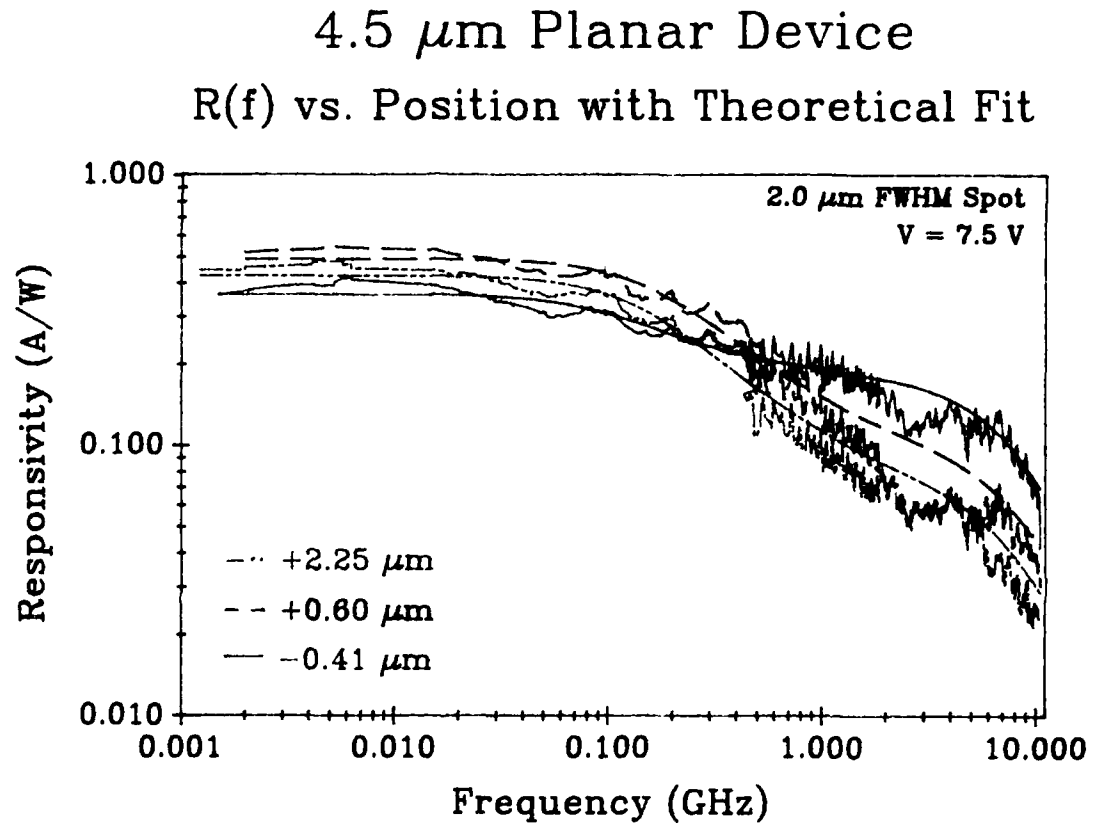
Figure 32:  $R(\omega)$  versus Beam Position for a 4.5- $\mu\text{m}$  Planar Gap Detector.

Figure 33:  $R(\omega)$  versus Bias for a 3.0- $\mu\text{m}$  Planar Gap Detector.

### 3.0 $\mu\text{m}$ Planar Device $R(f)$ versus Bias

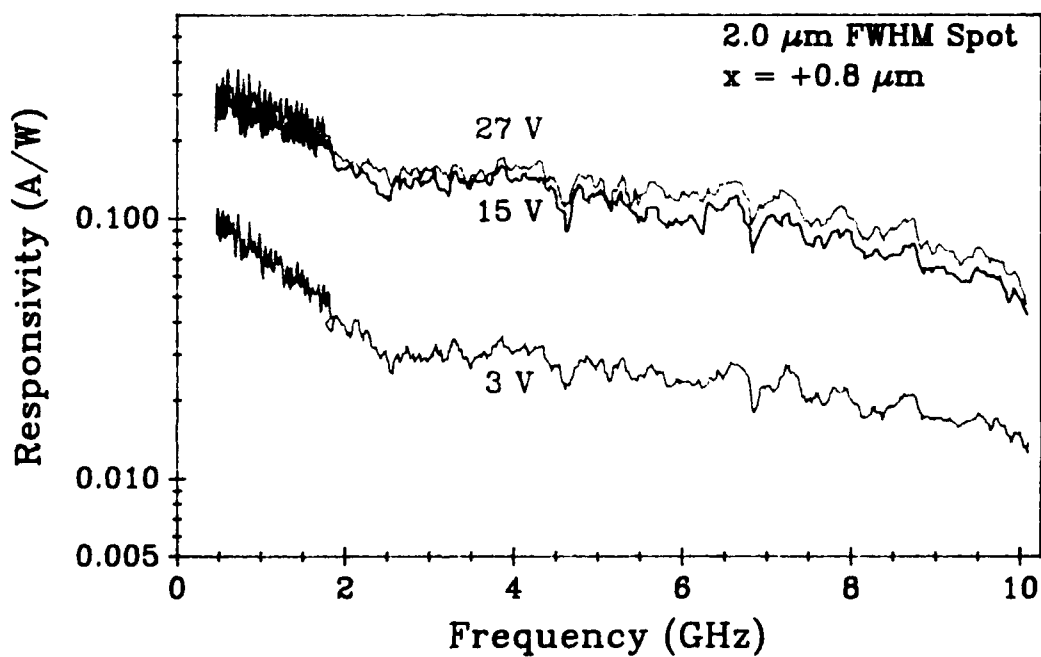


Figure 34: Low-Frequency Mechanism Bandwidth versus Hole Drift Velocity.

Low-Frequency Bandwidth versus Hole Drift Velocity for a 4.5- $\mu\text{m}$  Planar-Gap Detector

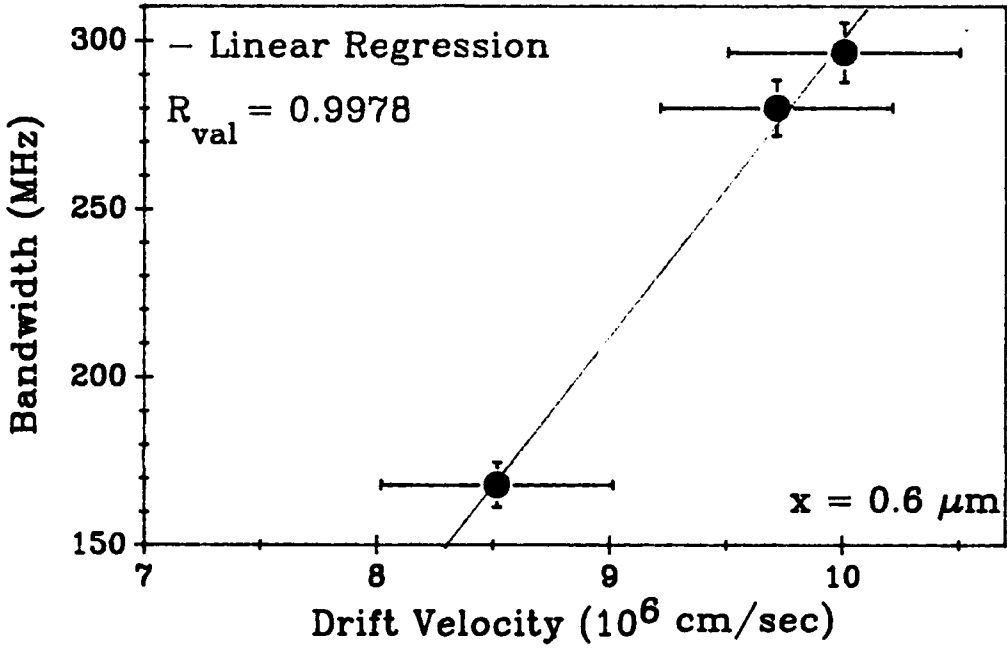


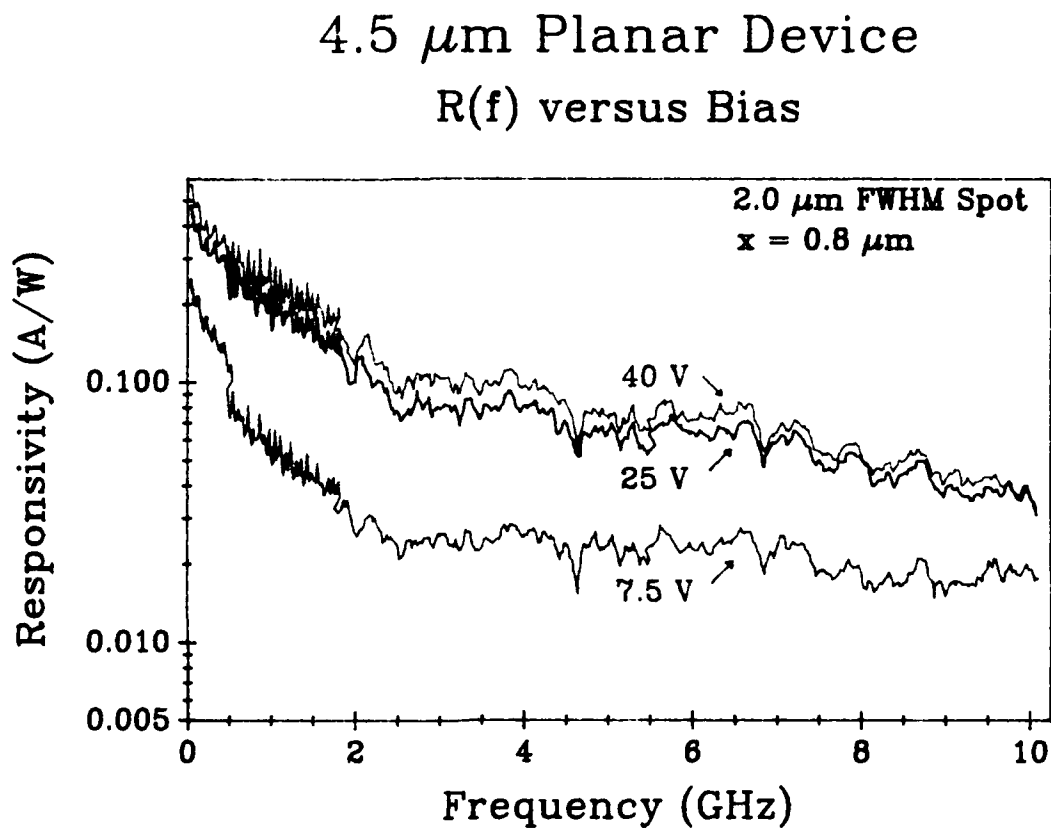
Figure 35:  $R(\omega)$  versus Bias for a 4.5- $\mu\text{m}$  Planar Gap Detector.

Figure 36:  $R(\omega)$  versus Bias for a  $4.5\text{-}\mu\text{m}$  Interdigitated Gap Detector.

4.5  $\mu\text{m}$  Interdigitated Device  
 $R(f)$  versus Bias

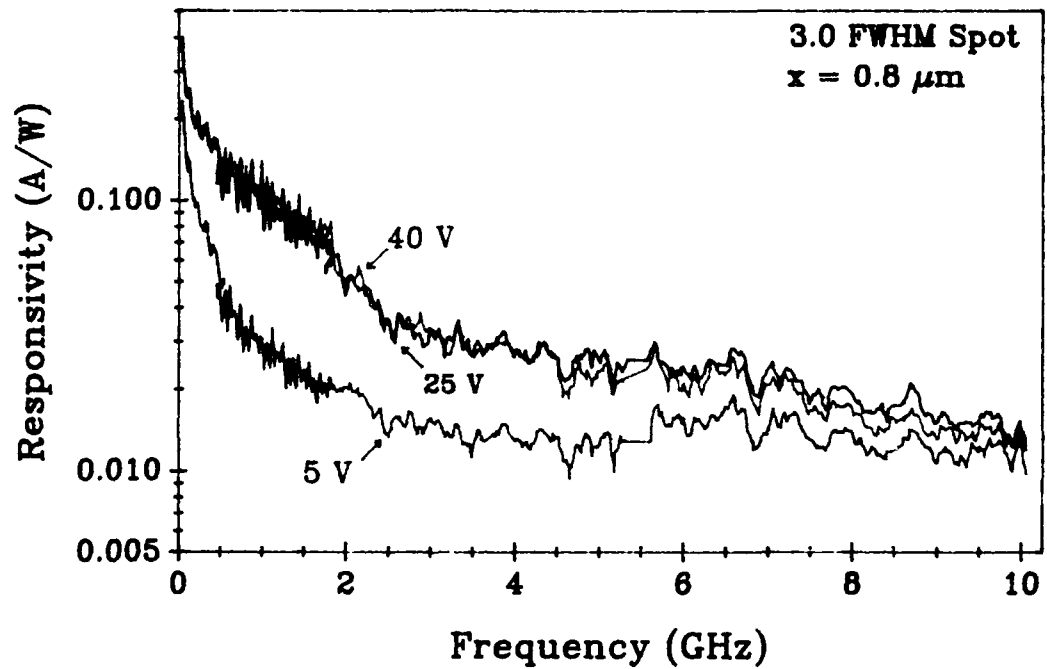


Figure 37:  $R(\omega)$  versus Beam Position for a 4.5- $\mu\text{m}$  Planar Gap Detector.

### 4.5 $\mu\text{m}$ Planar Device $R(f)$ versus Position

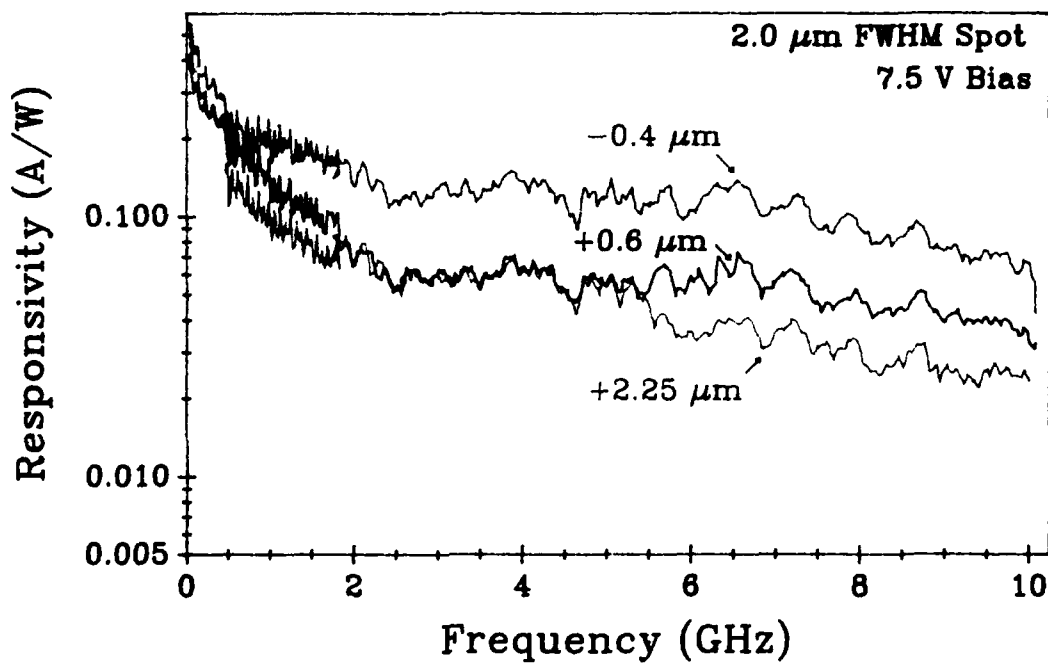


Figure 38:  $R(\omega)$  versus Beam Position for a 4.5- $\mu\text{m}$  Interdigitated Gap Detector.

### 4.5 $\mu\text{m}$ Interdigitated Device $R(f)$ versus Position

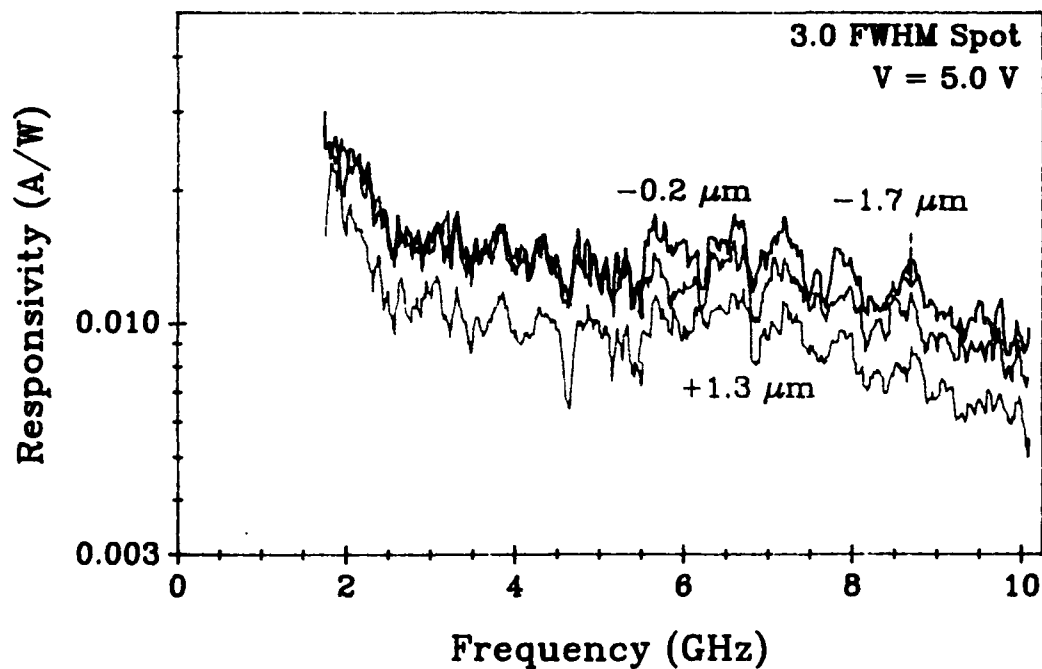


Figure 39: D.C. Responsivity Map of a 3.0- $\mu\text{m}$  Planar Gap Detector.  
( $V = 3.0 \text{ V}$ )

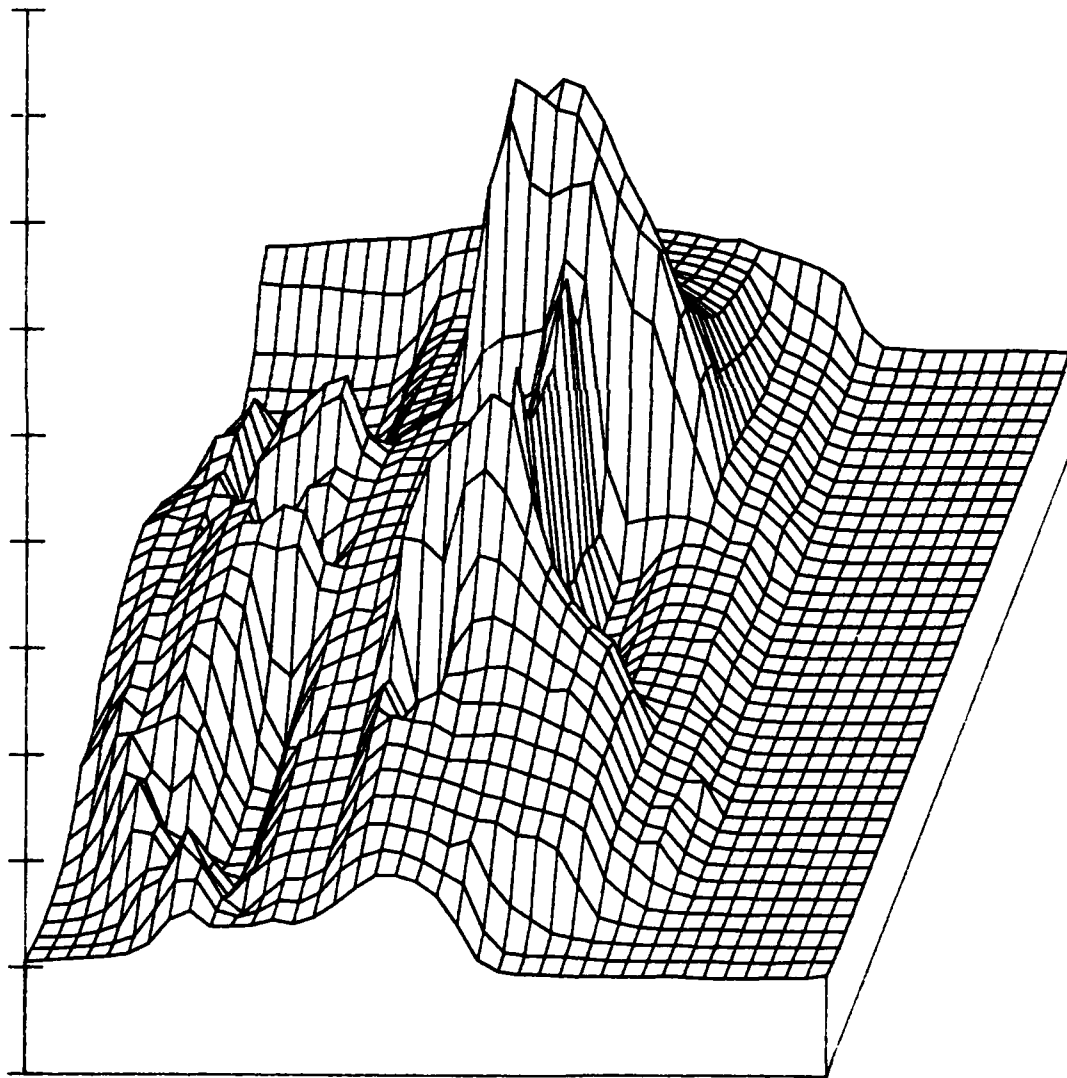


Figure 40: Contour Plot of Figure 39.

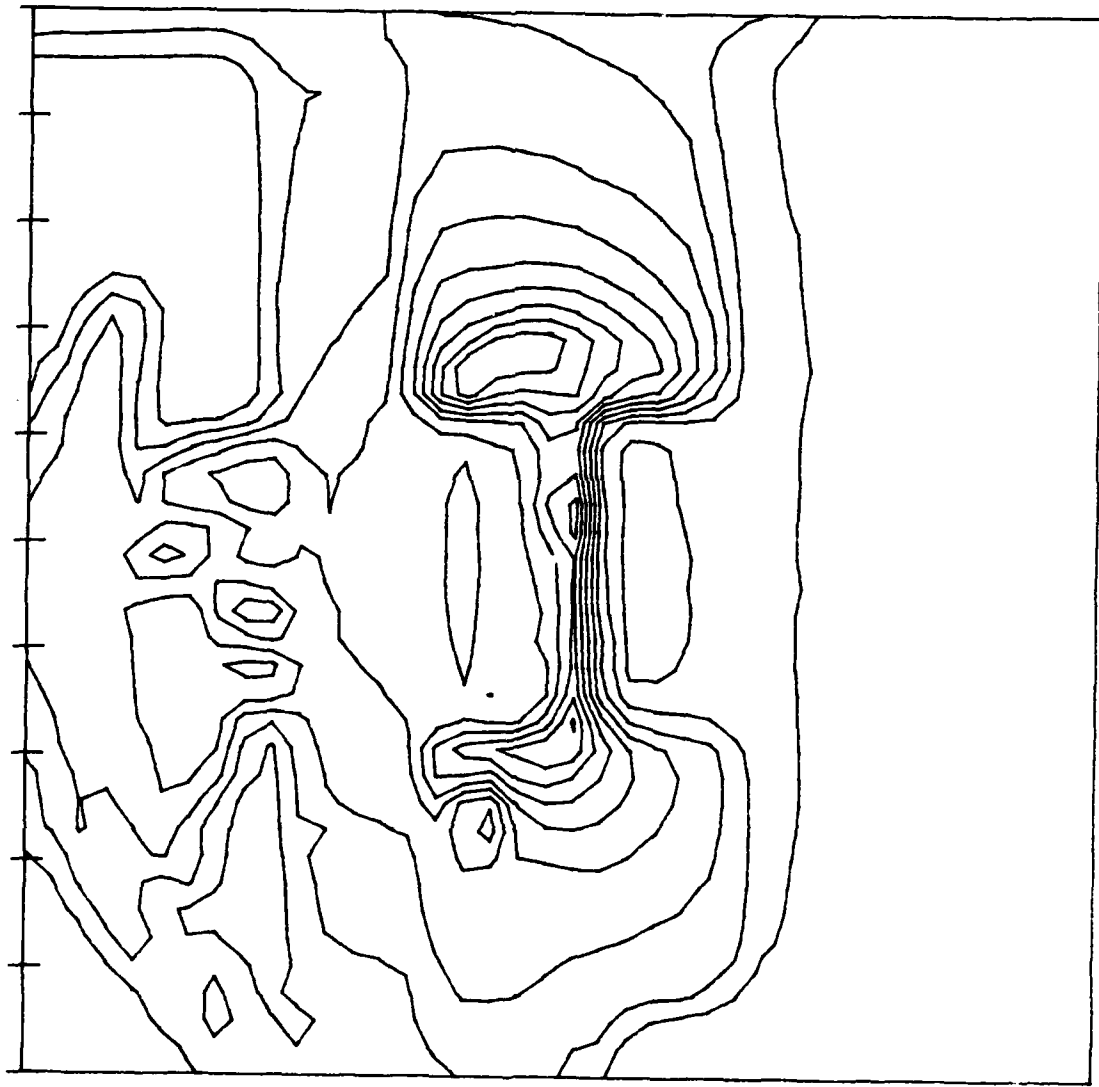


Figure 41: D.C. Responsivity Map of a 3.0- $\mu\text{m}$  Planar Gap Detector.

(V = 15.0 V)

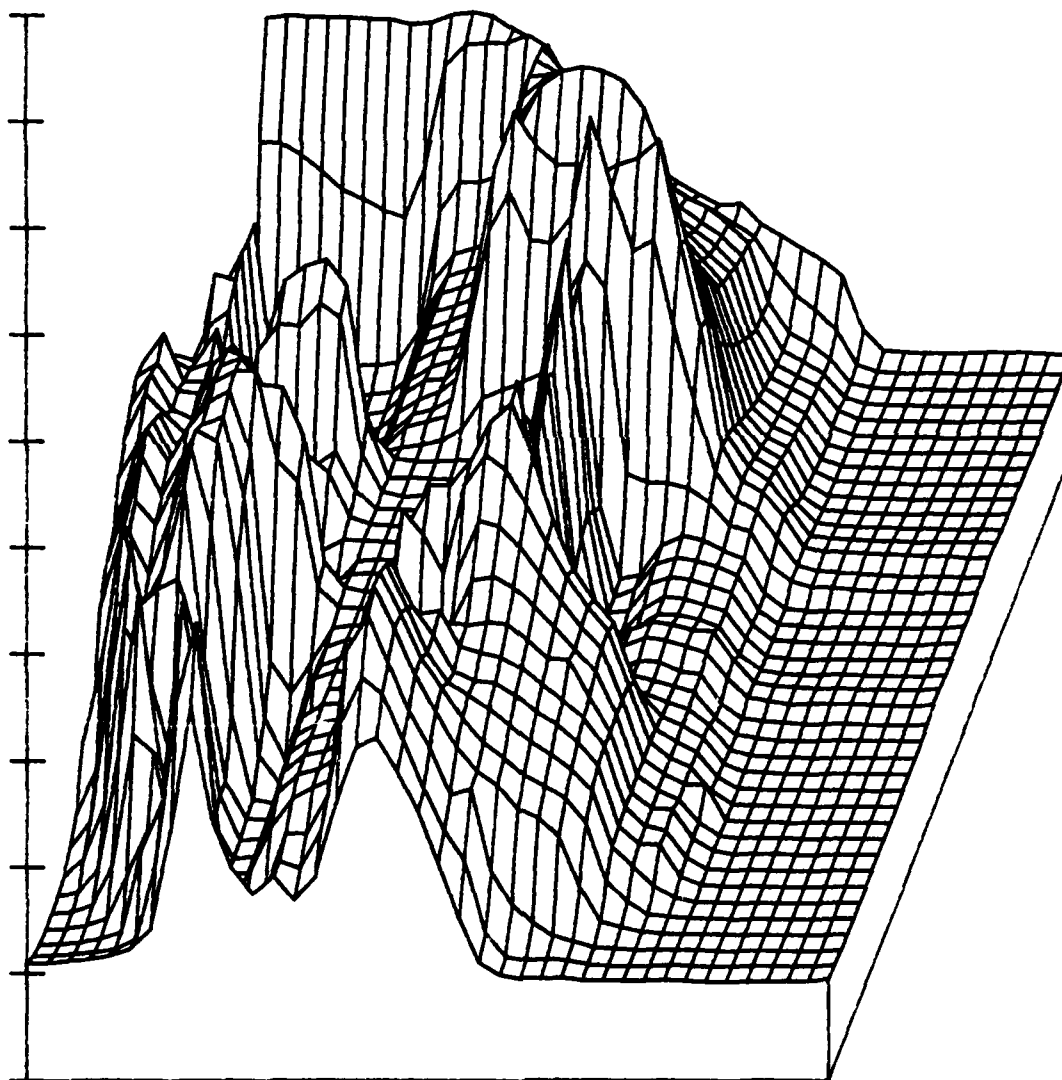


Figure 42: 1 GHz Responsivity map of a 3.0- $\mu\text{m}$  Planar Gap Detector.  
( $V = 3.0 \text{ V}$ )

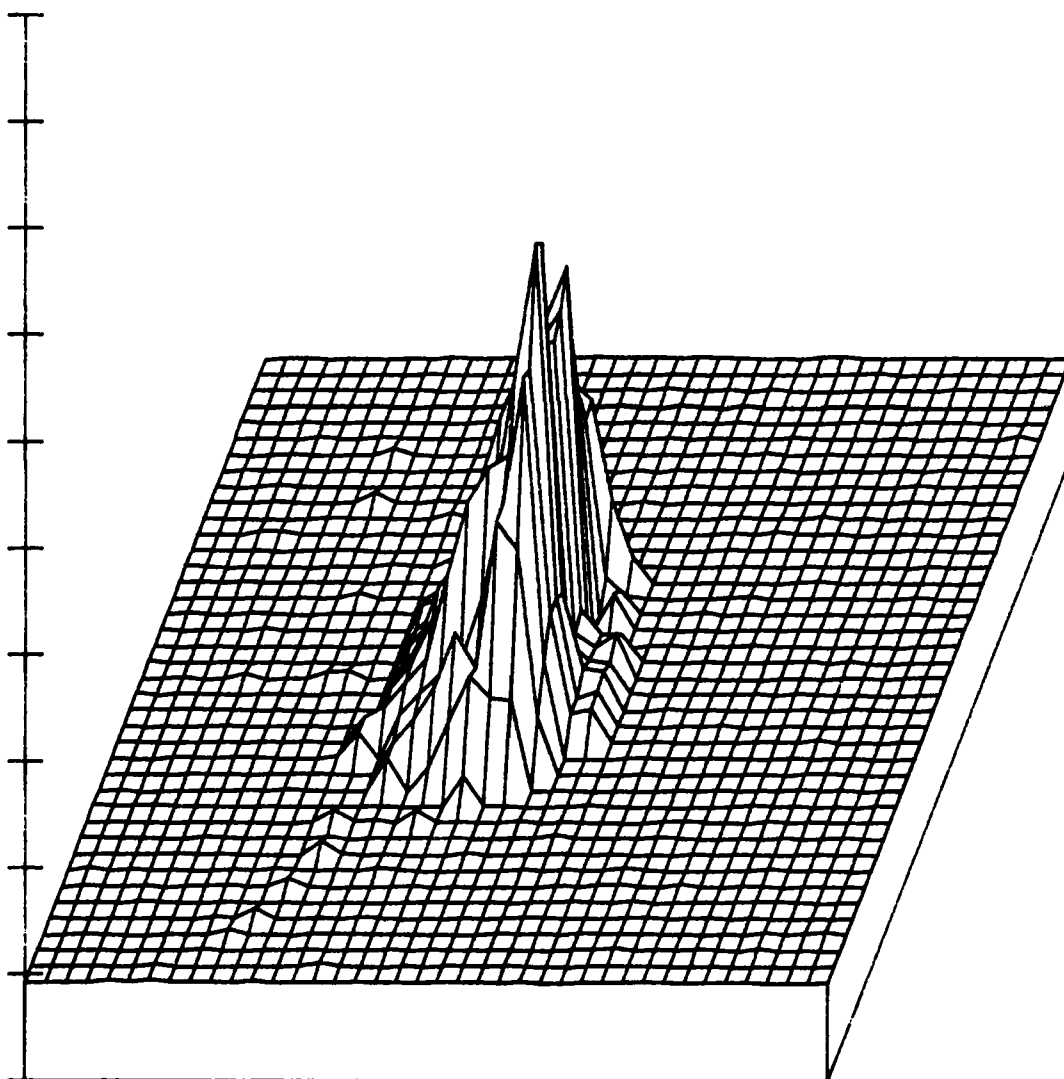


Figure 43: Contour Plot of Figure 42.

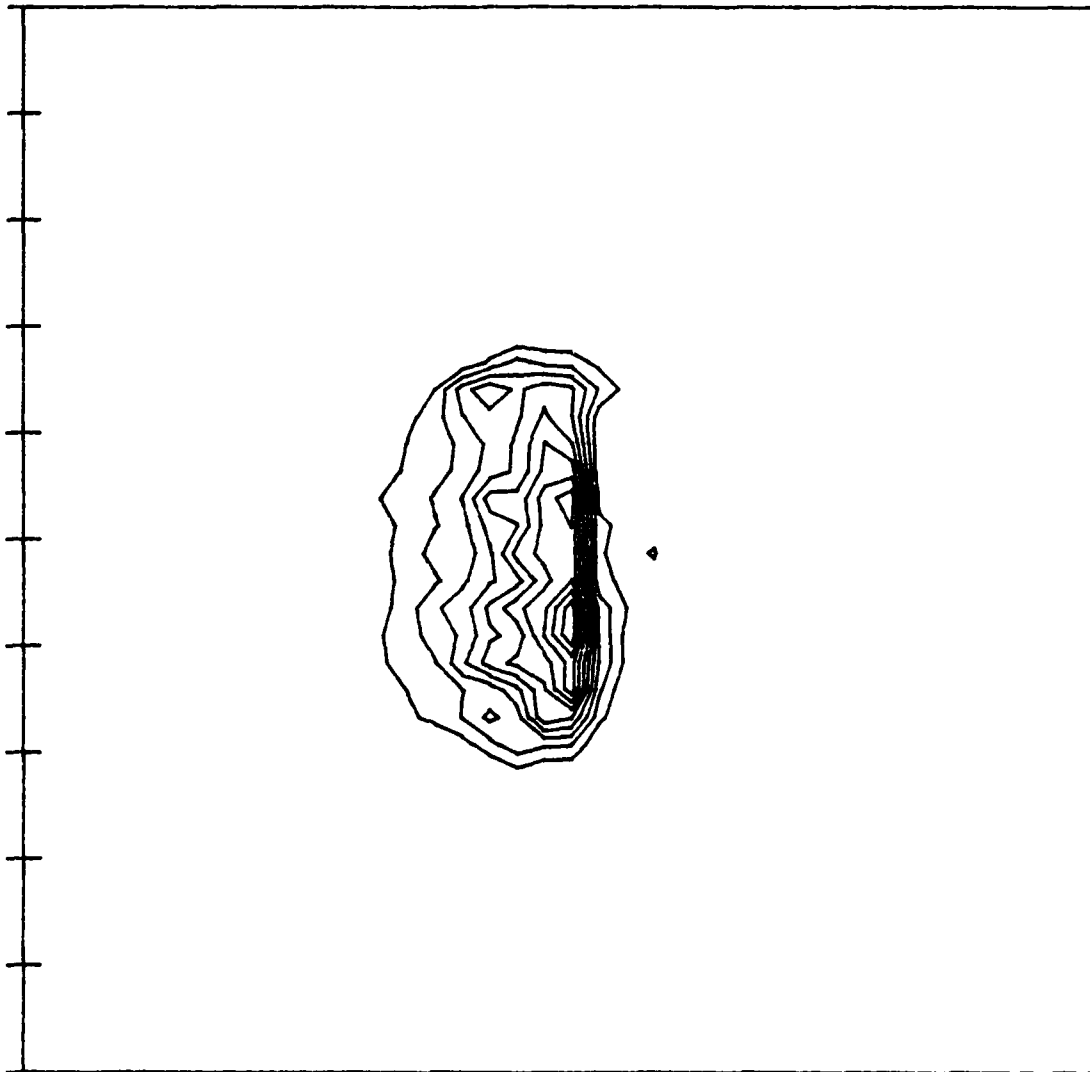


Figure 44: 1 GHz Responsivity map of a 3.0- $\mu\text{m}$  Planar Gap Detector.

(V = 15.0 V)

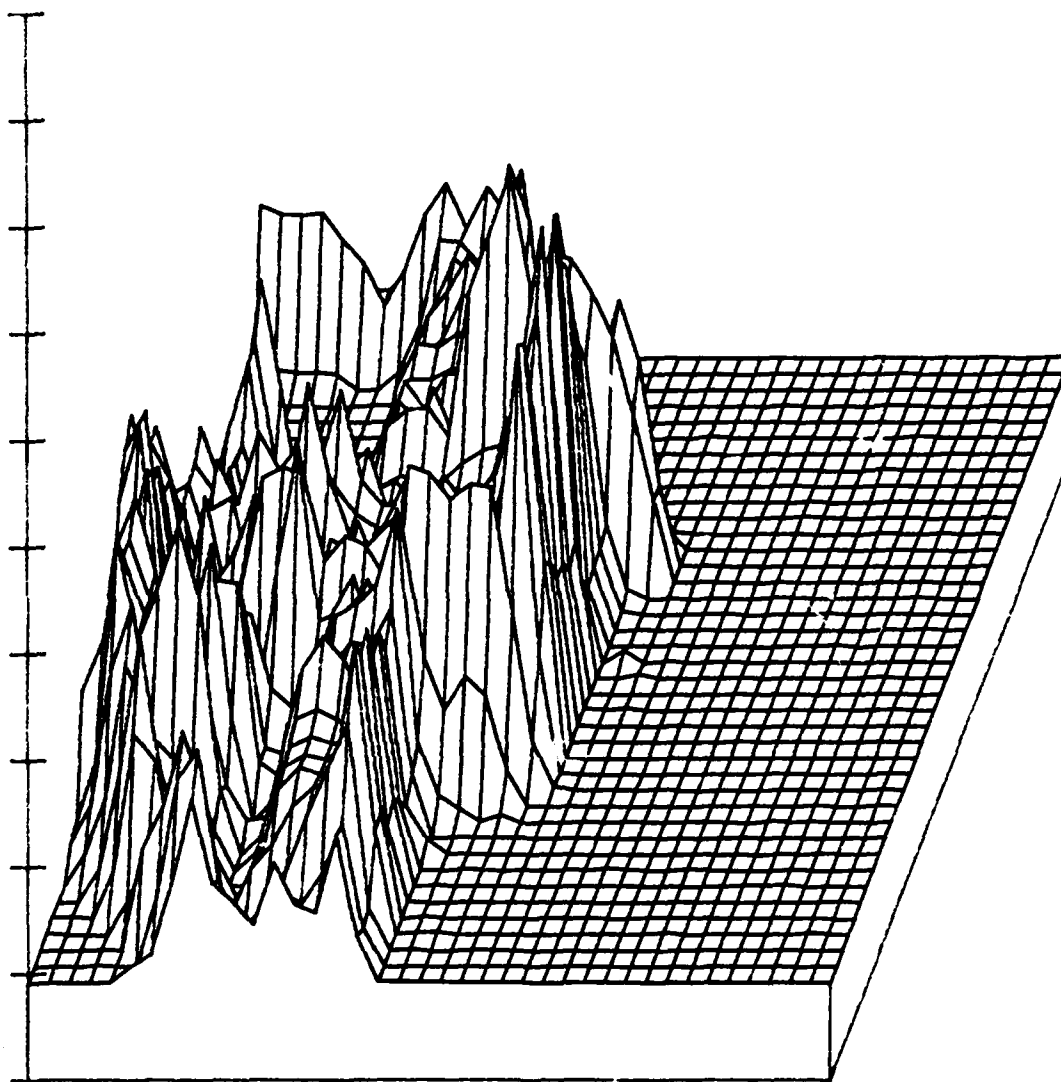


Figure 45: 9 GHz Responsivity map of a 3.0- $\mu\text{m}$  Planar Gap Detector.  
( $V = 3.0 \text{ V}$ )

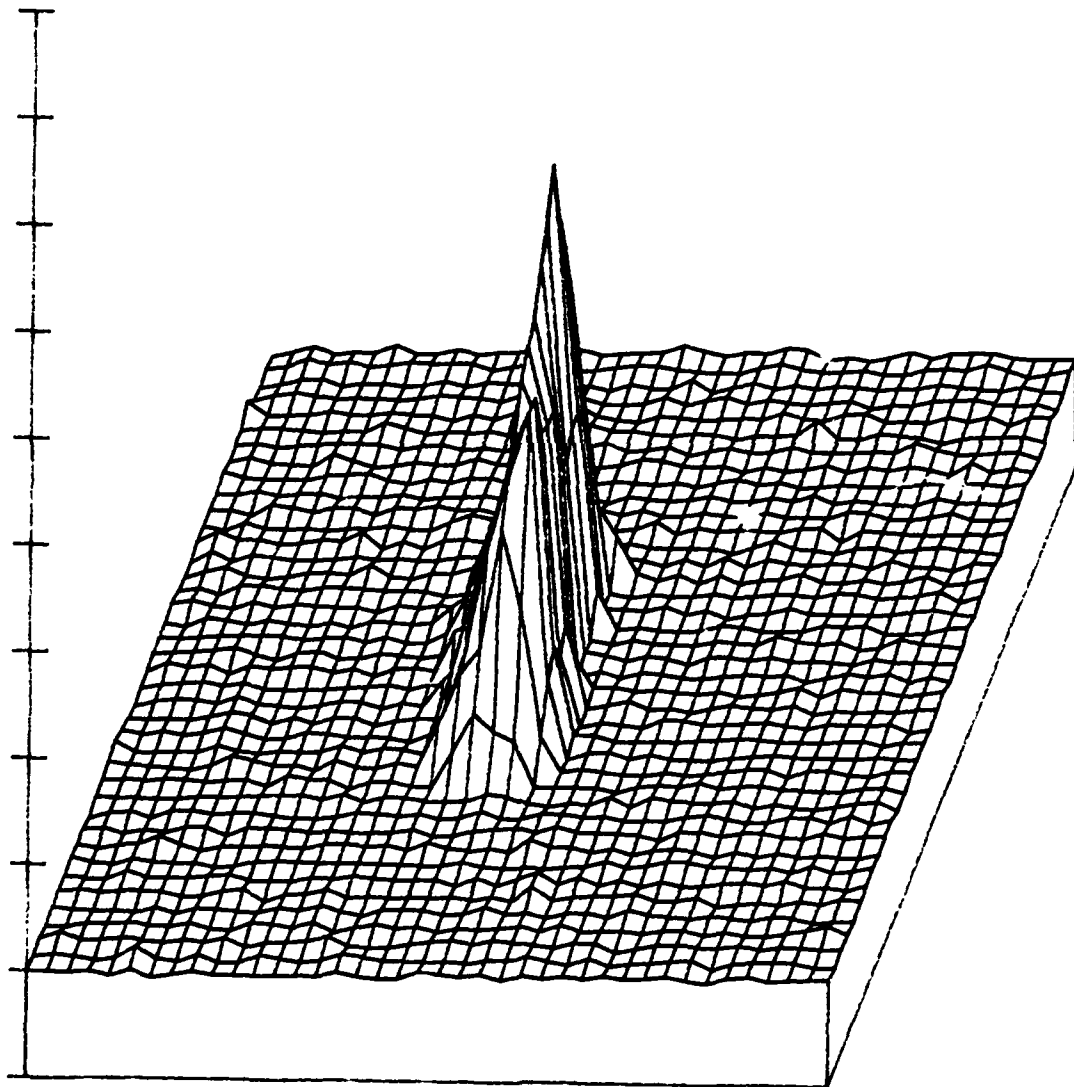


Figure 46: Contour Plot of Figure 45.

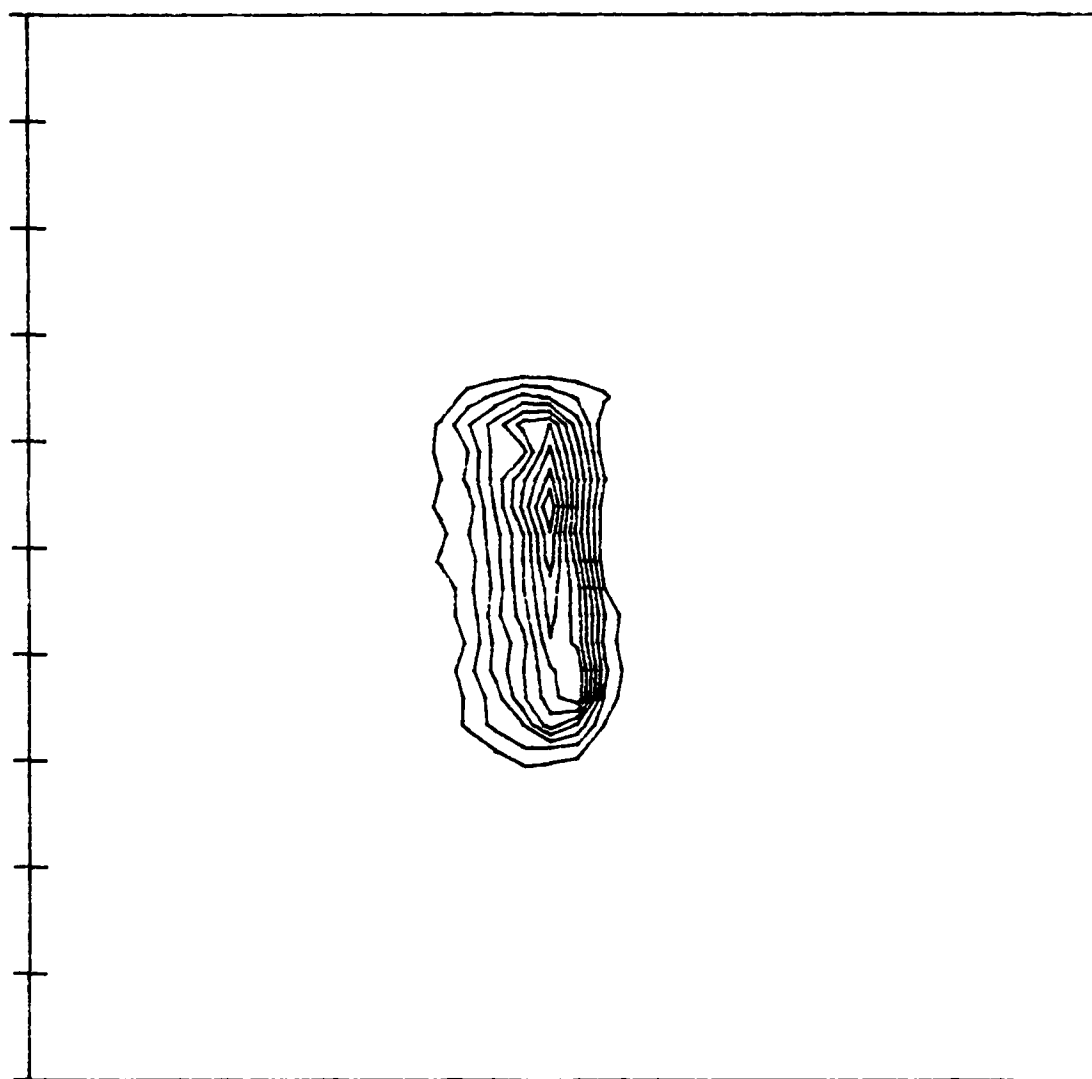


Figure 47: 9 GHz Responsivity map of a 3.0- $\mu\text{m}$  Planar Gap Detector.

( $V = 15.0 \text{ V}$ )

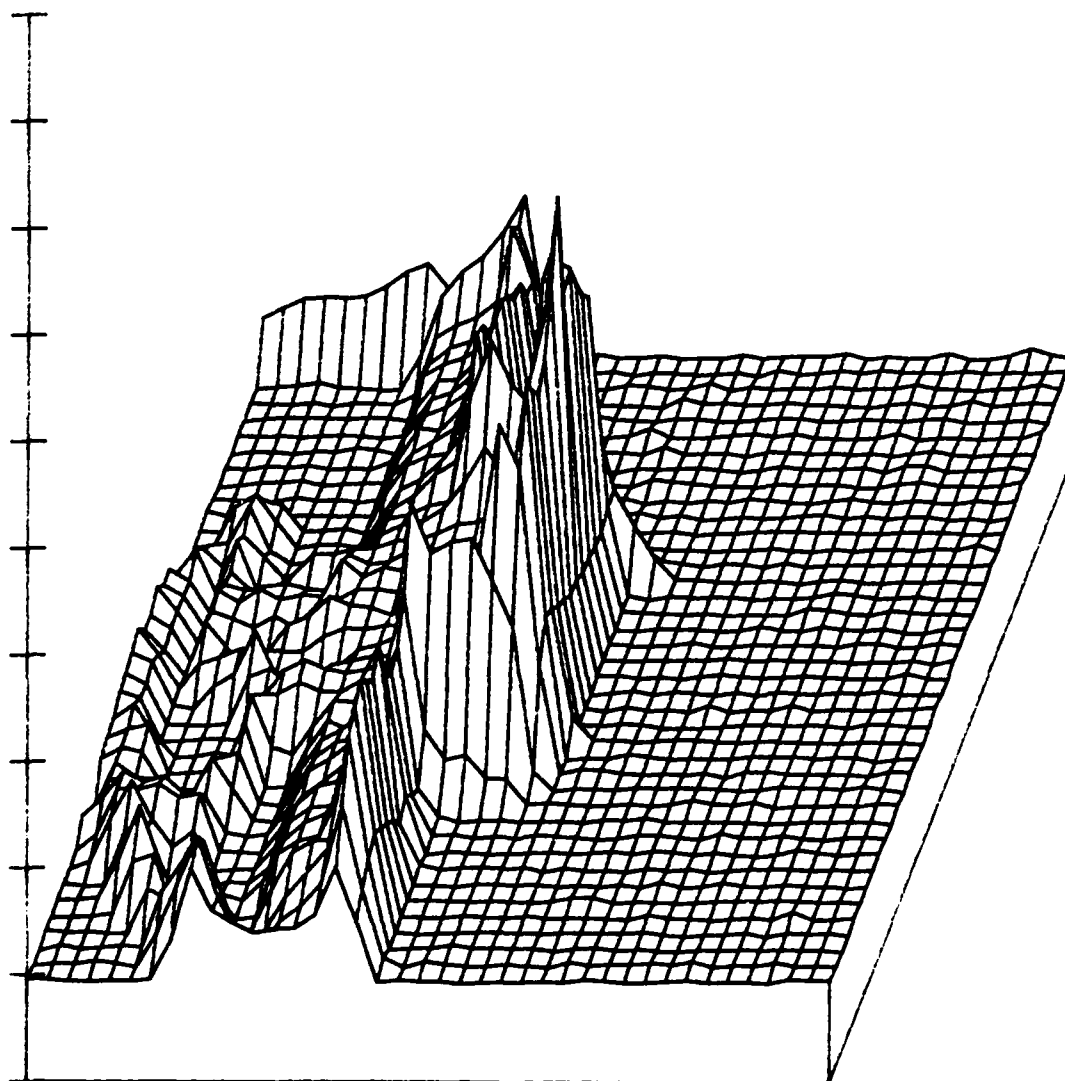


Figure 48: Contour Plot of Figure 47.

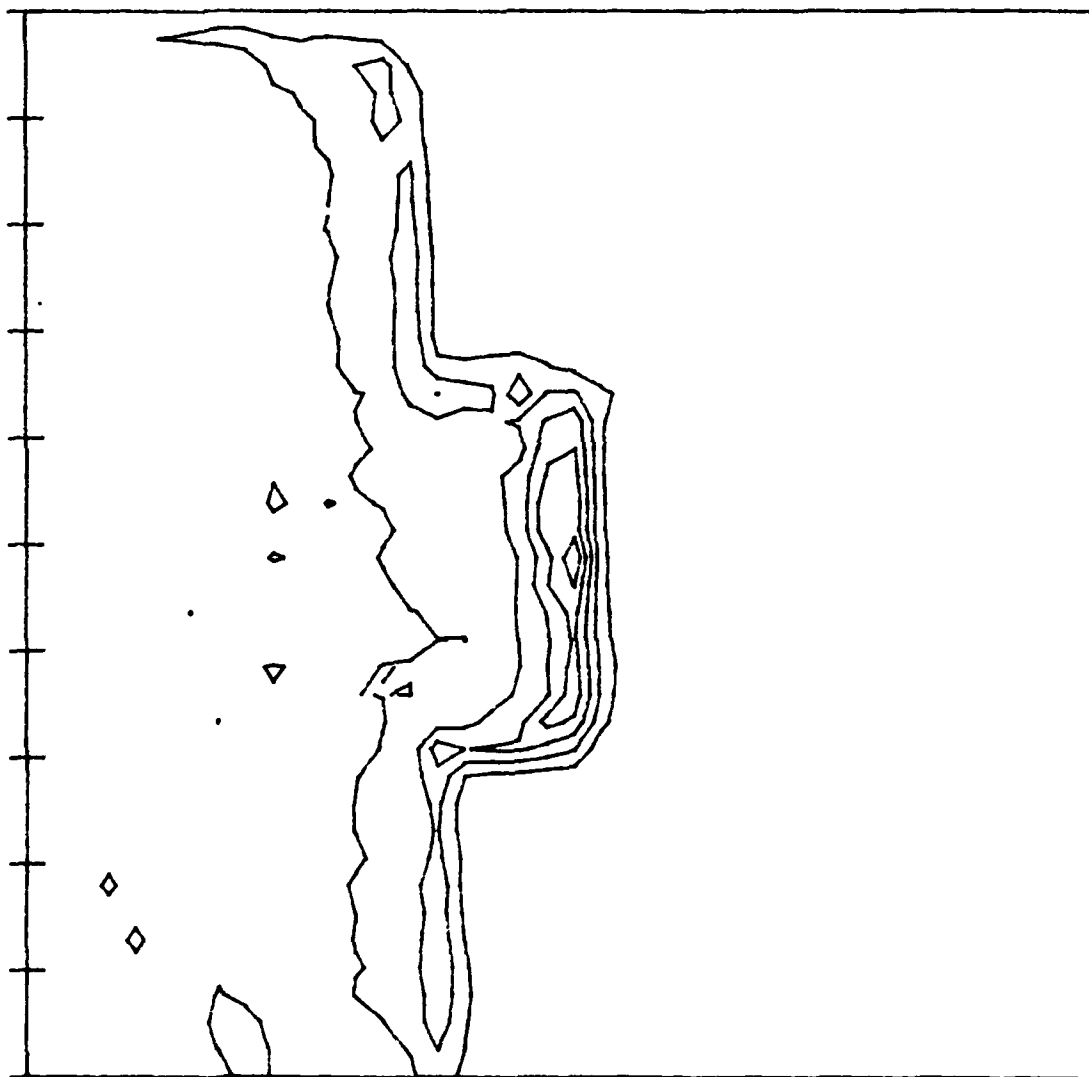


Figure 49: D.C. Responsivity Contour Plot of a 3.0- $\mu\text{m}$  Interdigitated Gap Detector. ( $V = 3.0\text{ V}$ )

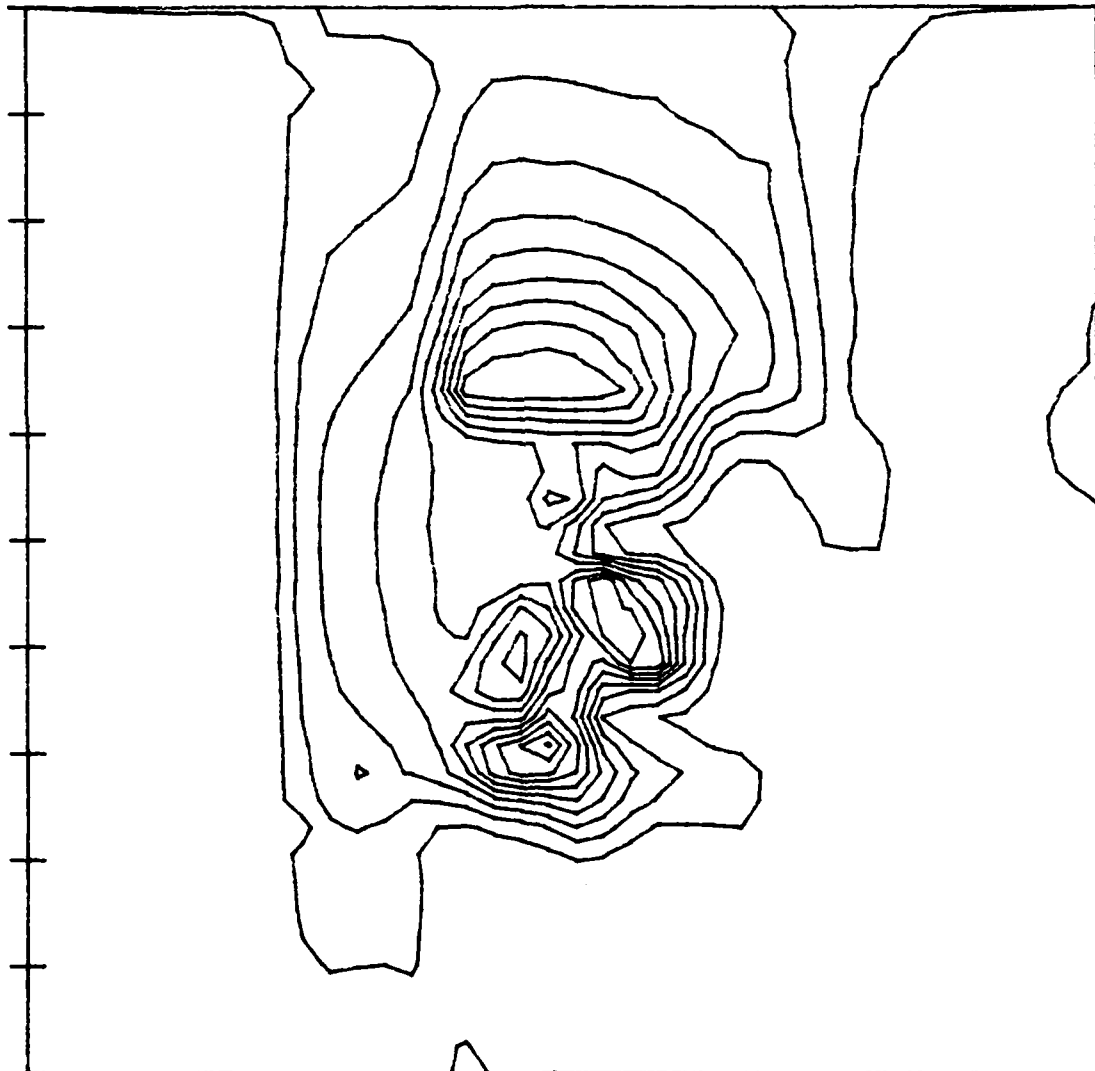


Figure 50: 1 GHz Responsivity Contour Plot of a 3.0- $\mu\text{m}$  Interdigitated Gap Detector. ( $V = 3.0 \text{ V}$ )

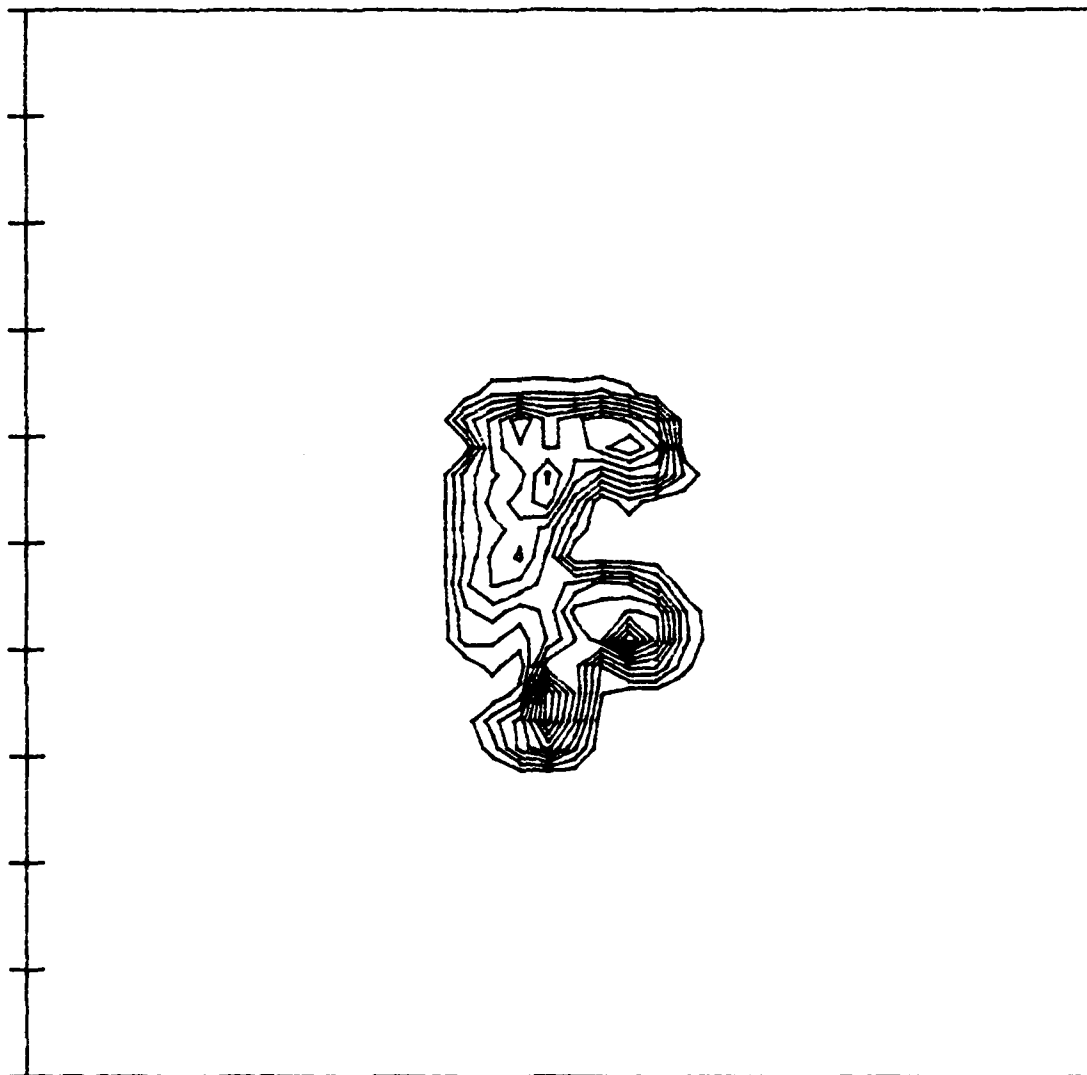


Figure 51: 9 GHz Responsivity Contour Plot of a 3.0- $\mu\text{m}$  Interdigitated Gap Detector. (V = 3.0 V)

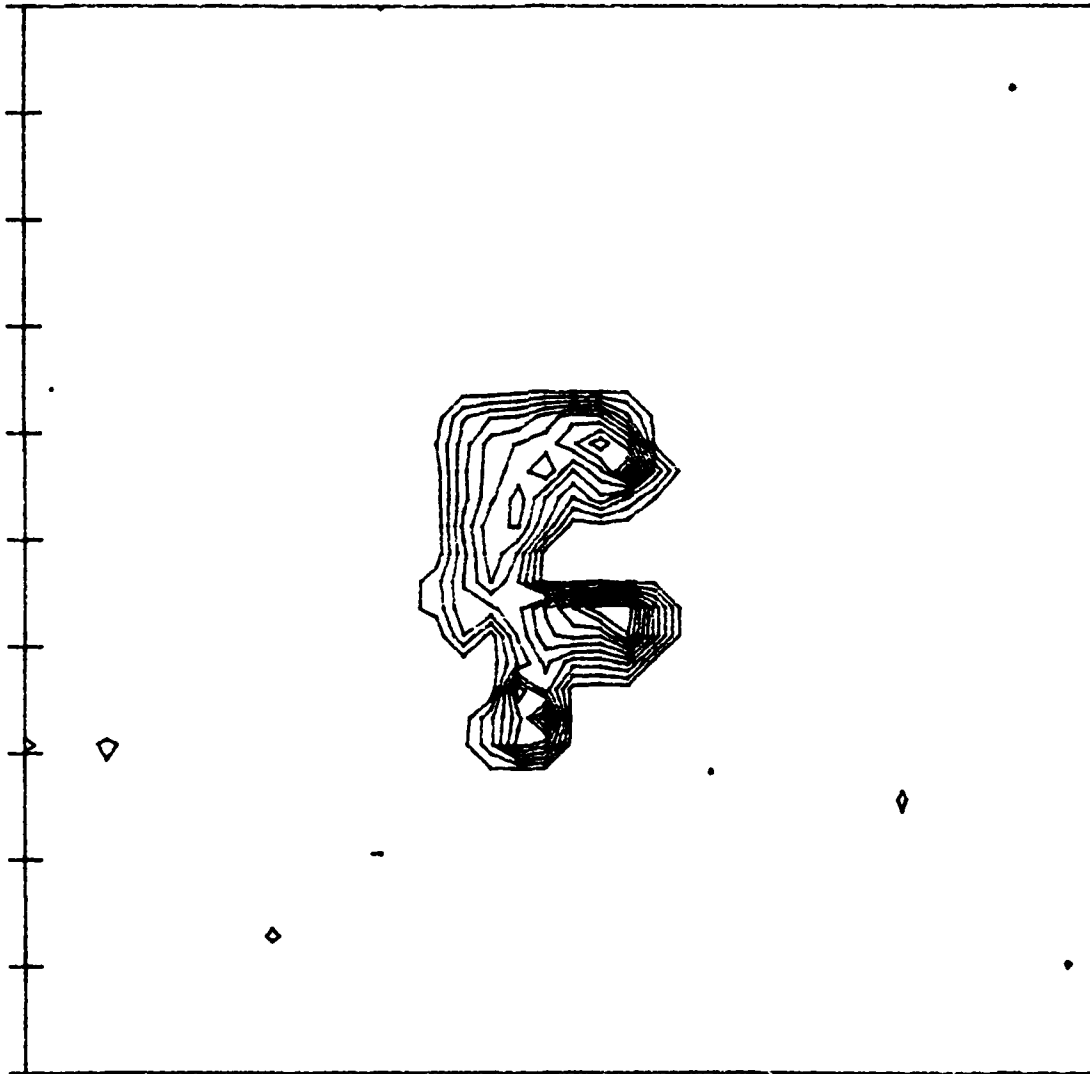


Figure 52: 1 GHz Responsivity Contour Plot of a 3.0- $\mu\text{m}$  Interdigitated Gap Detector. (V = 15.0 V)

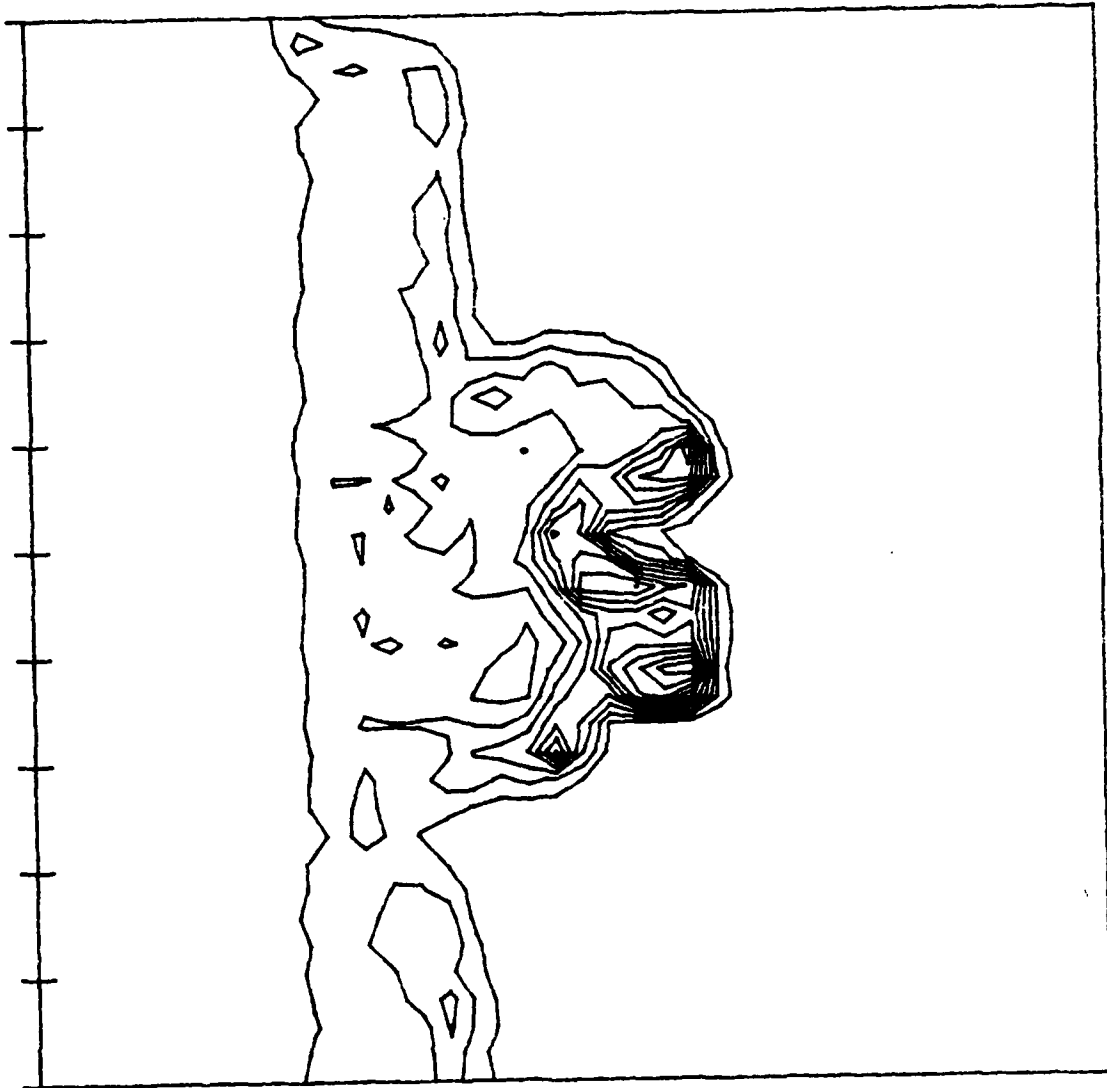


Figure 53: 9 GHz Responsivity Contour Plot of a 3.0- $\mu\text{m}$  Interdigitated Gap Detector. ( $V = 15.0 \text{ V}$ )

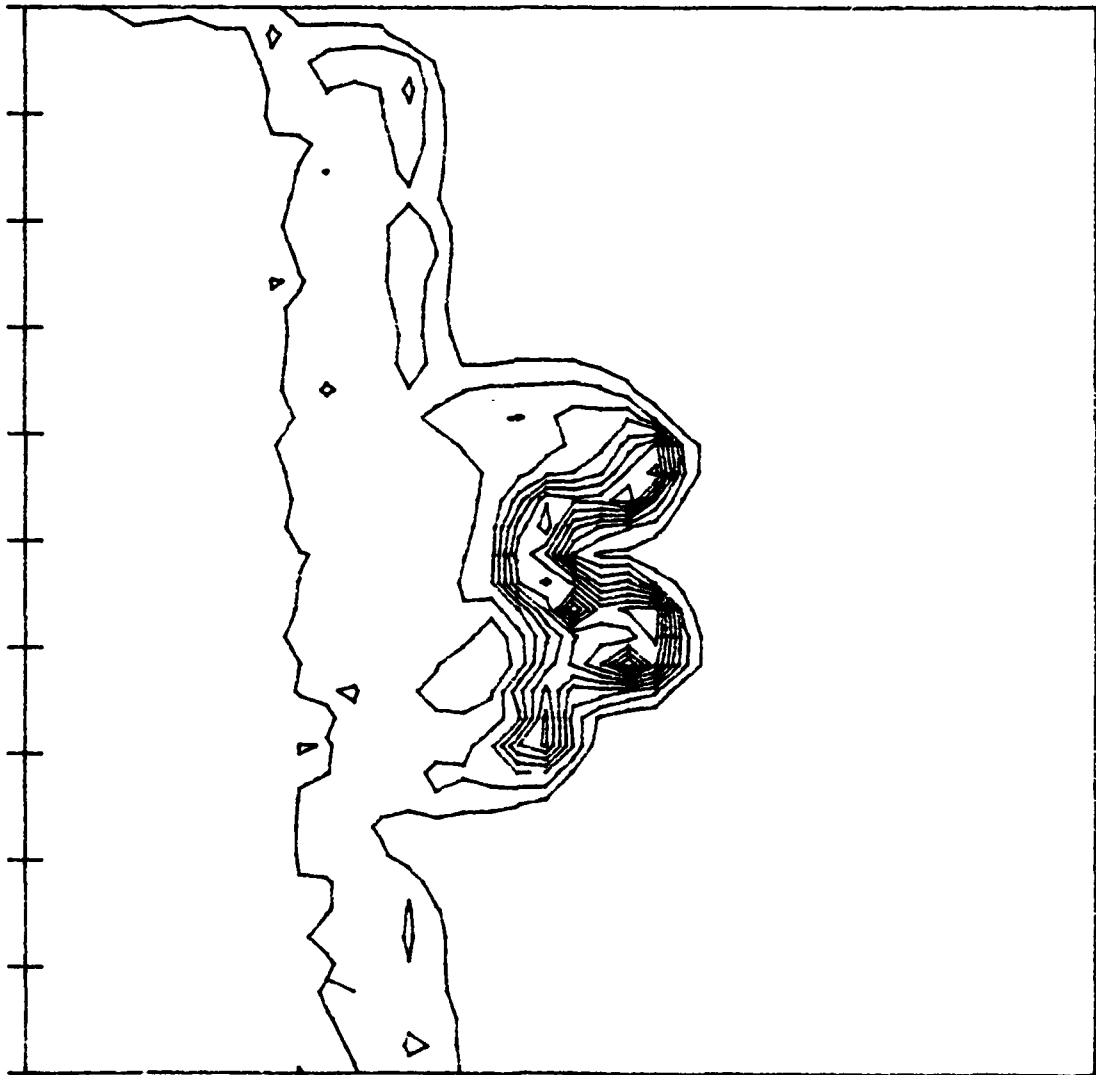


Figure 54: D.C. Photoresponse versus Time of a GaAs MSM Detector.

## Degradation of a GaAs Detector versus Time

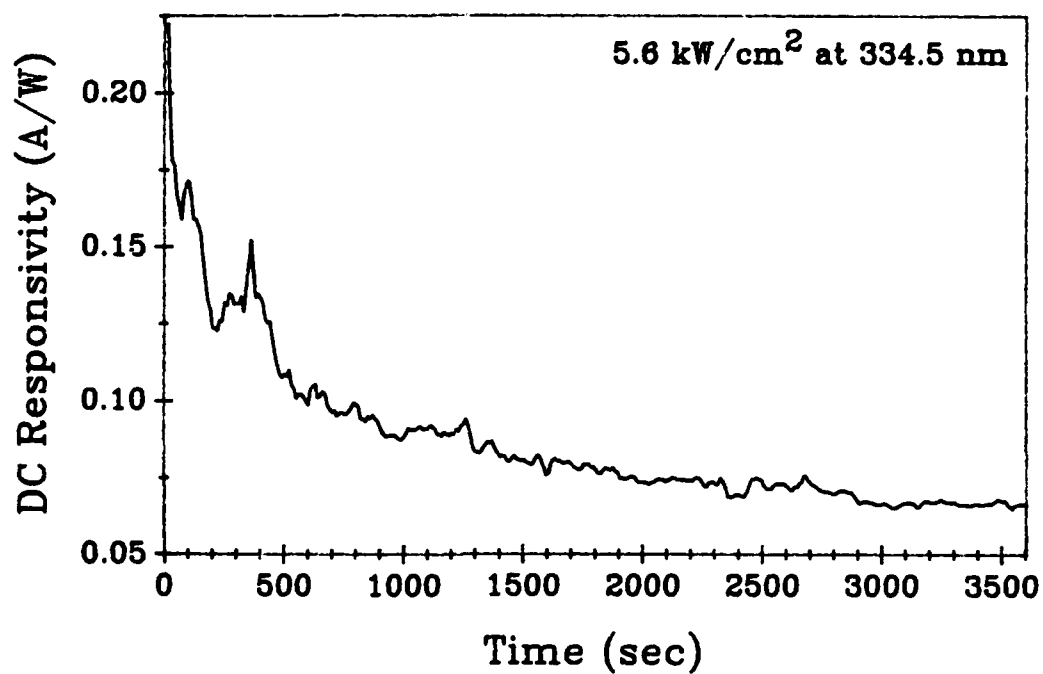


Table 7: Bias and beam Position for the 4.5- $\mu\text{m}$  planar detector

| Bias<br>(V) | X Position<br>( $\mu\text{m}$ ) | Figure No. |
|-------------|---------------------------------|------------|
| 9           | 0.0                             | 28         |
| 12          | 0.0                             | 28         |
| 15          | 0.0                             | 28         |
| 7.5         | -1.7, +0.8, +1.8                | 32 and 31  |
| 25.0        | 0.8                             | 31         |
| 40.0        | 0.8                             | 31         |

Table 8: Beam Position Fit to High-frequency Data.

| Bias<br>(V) | $X_0$ expected<br>( $\mu\text{m}$ ) | $X_0$ fitted<br>( $\mu\text{m}$ ) |
|-------------|-------------------------------------|-----------------------------------|
| 7.5         | +0.8                                | 0.60                              |
| 25.0        | +0.8                                | 2.25                              |
| 40.0        | +0.8                                | 2.25                              |
| 7.5         | -1.7                                | -0.41                             |
| 7.5         | +0.8                                | 0.60                              |
| 7.5         | +1.8                                | 2.25                              |

Table 9: Data fit variables.

| $v_n$<br>(106 cm/sec) | $v_p$ | $x_o$<br>( $\mu\text{m}$ ) | -3 db point<br>(GHz) |
|-----------------------|-------|----------------------------|----------------------|
| 7.36                  | 4.25  | 1.42                       | 4.73                 |
| 7.73                  | 4.30  | 1.40                       | 4.79                 |
| 7.25                  | 4.36  | 1.42                       | 4.74                 |
| 7.74                  | 4.31  | 1.42                       | 4.79                 |
| 7.60                  | 4.29  | 1.42                       | 4.77                 |
| 7.30                  | 4.29  | 1.23                       | 4.77                 |



Table 11: Low-frequency characteristics versus hole drift velocity.

| Bias(V) | Normalized Values |       |        |        |
|---------|-------------------|-------|--------|--------|
|         | $v_p$             | $f_p$ | HF Amp | LF Amp |
| 40      | 1.000             | 1.000 | 1.000  | 1.0    |
| 25      | 0.911             | 0.945 | 0.856  | 0.830  |
| 7.5     | 0.641             | 0.554 | 0.389  | 0.491  |

Table 12: LF Gain vs Bias and Position

| Bias  | Position | Gain |
|-------|----------|------|
| 40 V  | +0.60    | 3.80 |
| 25 V  | +0.60    | 3.69 |
| 7.5 V | +0.60    | 4.80 |
| 7.5 V | -0.40    | 1.04 |
| 7.5 V | +0.60    | 5.32 |
| 7.5 V | +2.25    | 6.38 |

## References

1. M.S. Caceci and W.P. Cacheris, "Fitting Curves to Data, The Simplex algorithm is the answer", BYTE, May 1964, pg 340, (1964).
2. S. M. Sze, Physics of semiconductor Devices, 2nd Ed., John Wiley and Sons, (1981).
3. S.F. Soares, Ultraviolet Heterodyne Photodetectors, Ph.D. Dissertation, Dept. of Elec. Eng., Univ. of NM, (1989).
4. M.Y.A. Raja, S.R.J. Brueck, M. Osinski, and J. McInerney, Appl. Phys. Lett., 52, pg. 625, (1988).

## Chapter V

### Conclusions and Recommendations

Several major accomplishments have resulted from this work. From this work several conclusions about the performance and limitations of msm detectors are made. Also, some recommendations for further study on the present msm design are presented. Finally, a new detector design is put forth that should show some improvements over the present design.

First, to our knowledge, the only reported uv-heterodyne system has been assembled, calibrated, and tested out to 18 GHz. The system's day-to-day repeatability has a  $\pm 1$ -db standard deviation in detector output response. This small error, when compared to the 40 to 50-db signal, indicates that the system is highly stable. Using computer controlled micropositioners, detailed mapping of a detector's responsive area is reported for the first time. Finally, this system allowed for the first very high frequency response,  $>20$  MHz, of any detector in the ultraviolet.

Significant advances in msm detector modeling were also made. The responsivity of a msm detector under illumination by a modulated uv point light source has been analytically solved. The model assumes a constant drift velocity for the charge carriers and a well defined drift path that is independent of depth in the crystal. The short penetration depth of uv light into any semiconductor permits these approximations. An analytical solution for the charge density, as a function of time and space, for an impulse of light has been previously reported.<sup>1</sup> However, calculating the current in the external circuit from this charge density cannot be done in closed form. However, by working in the frequency

domain, this work has led to a closed form analytical solution for the current in the external circuit due to a uv point source located somewhere inside the gap region of a msm detector. This theory may lend itself to longer wavelengths by using numerical techniques to sum several currents with different charge carrier drift velocities and path lengths, depending upon the depth inside of the semiconductor.

For uv wavelengths, the model does appear to adequately predict detector behavior. The model predicts that a 4.5- $\mu\text{m}$  wide msm photodiode has a -3-db point of approximately 21 GHz at 30-V bias. A 1- $\mu\text{m}$  wide detector under a 6.7-V bias is predicted to have a 75-GHz bandwidth. The model, however, does not include RC effects and it is doubtful that the present 1.0- $\mu\text{m}$  detector design would reach this predicted frequency.

The theory was compared to data for several detectors. The 4.5- $\mu\text{m}$  planar gap detector was tested extensively. The theory predicted a 21-GHz -3-db point for this detector under a 30-V bias. Direct comparison of theory and data was obscured by the effects of bonding wire inductance in the rf package. However, good results were obtained by including this simple L/R pole in the theoretical fit. It was found that the theory combined with the inductor roll-off matches the data very well out to 14 GHz. When the 18-GHz bandwidth of the SMA connector was included, the theory matched the data out to 18 GHz. Thus, these measurements tentatively support the model, but limitations in the rf packaging prevented a complete comparison of the model with the data. A relative check on the viability of the model was confirmed with the response versus position scans. The model does correctly predict the change in the high frequency response as a function of change in beam position on a 4.5- $\mu\text{m}$  detector to within 0.2  $\mu\text{m}$ .

Similar results could not be obtained with the 3.0- $\mu\text{m}$  detector. This was due to the large value of the package inductance effectively obscuring the small changes in  $R(\omega)$  with position. Problems with accurately locating the defined gap center also caused the  $R(\omega)$  versus position fits to the model to be questionable for the 1.0- $\mu\text{m}$  detector. In order to confirm the model and probe for modifications in carrier drift characteristics near the semiconductor surface, the rf package must be totally redesigned. This was unexpected, since the present design is widely used in high-speed devices reported in the literature. It is encouraging, though, that with a proper rf package, the msd detectors should perform very well. The charge carriers near the surface of Si appear to behave as if they were in bulk material. This result is new and unexpected.

The responsivity curves of the planar and interdigitated detectors were compared. It was found that the dark current of the interdigitated detectors was lower than for the planar-gap detectors of equal gap dimension. Again, the rf-packaging limitations precluded any direct rf comparisons, but relative comparisons could be made. It was found that the relative changes in  $R(\omega)$  for changes in beam position or detector bias were lower for the interdigitated design than for the planar. Also, the active area of the interdigitated detectors was more uniform and less sensitive to changes in detector bias than the planar detectors. In light of the detector model, this implies that the average drift velocities of the charge carriers were higher in the interdigitated, than in the planar, detectors. To achieve these higher velocities the average electric field strength must be higher. The source for this enhanced field, since nearly identical biases were used,

is the existence of more corners on the electrodes of the interdigitated detectors, than on the planar.

Confirmation that the responsivity is higher around the corners on the electrodes was seen in the responsivity maps of the detector surface. These highly detailed maps show definite areas of high responsivity located near the corners of the electrodes in both the interdigitated and the planar detectors. These maps also showed that the large d.c. responsive area decreased in size at rf frequencies. The planar detectors showed a decrease in active area between 1 GHz and 9 GHz, while the interdigitated detector's responsive area remained nearly constant. This is consistent with the hypothesis that the additional corners in an interdigitated device causes higher electric fields, hence higher drift velocities, than in a planar device.

Contrary to this result, however, is the d.c. dark current behavior of the interdigitated detectors. Without exception, the interdigitated detectors tested had lower dark currents than their planar counterparts. This result is not understood at this time and should be the subject of further investigation.

Moving away from the gap region, another interesting result is seen at the edges of the cathode bonding pad. A region of higher responsivity, with respect to its surroundings, is seen along this edge. The response is present even out to 9 GHz for the higher biases. Apparently the  $\text{SiO}_2$  dielectric layer, used to isolate these pads from the Si, is not thick enough. Obviously, some of the photo-generated charge can tunnel through the dielectric to reach the pad. Therefore, it is clear that this insulating layer must be thicker.

The low-frequency gain seen in all msm photodiodes was analyzed next. It was found that an apparent relationship between the bandwidth of the gain mechanism and the drift velocity of the holes exists. It was also found that the gain amplitude was related to the hole transit time. Increasing the hole transit time by either lowering the bias, or moving the beam further away from the cathode, increased the gain.

The final detector tested was a msm photodiode on GaAs. However, both d.c. and rf photoresponse decreased with time, thus making this an unsuitable photodetector. This degradation is assumed to be related to the degradation of the surface photoluminescence of GaAs under visible laser irradiation.

Several areas of additional study are suggested by the results of this work. First, and foremost, the redesign of the rf package must be accomplished in order to definitively test the model against detector performance.

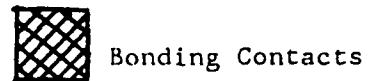
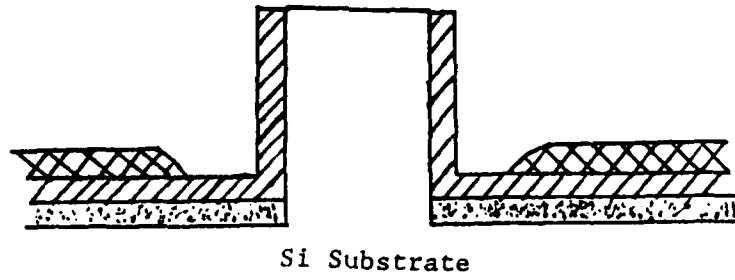
Assuming that the high frequency model is accurate, the low-frequency gain mechanism should be studied more extensively. If this mechanism is similar to photoconductive gain, then the bandwidth will not depend upon detector gap dimension, but only recombination. This does not appear to be the case, but the variable and uncontrolled inductance of the rf package does raise some difficulties. The true limiting mechanism must be found, be it hole transit time or recombination time limited. The gain amplitude does appear to be related to the hole transit time. If so, then a detector with a higher barrier should have a smaller gain since the photoconductivity would be lower with a less leaky (more resistive) diode.

Finally, an improved msm detector design is presented. The model in Chapter II is based on the premise that the charge carrier drift velocities are constant. Also, the distance traveled by a charge was assumed to be constant. Under high biases and uv illumination, these assumptions are valid. However, changing to a mesa design would eliminate the need for the uv-illumination restriction. The mesa design is shown in Figure 5-1. A small mesa is etched into the silicon and Ni Schottky diodes are laid down on the side walls, and on top of an SiO<sub>2</sub> insulating layer. Gold bonding pads are then laid down on top of the Ni contacts. Light enters into the Si parallel to and between the Ni contacts. The advantage of this design is two fold. First, the geometry of the applied electric field is much simpler and an analytic expression has previously been obtained for this field. Secondly, the field strength is constant as a function of depth in the semiconductor. This implies that this design should work as well, or better, at near IR wavelengths than it would at uv. The planar photodiodes probably do not have this property. In a planar msm device, the deeper into the semiconductor an electron-hole pair is produced, the farther they have to travel to their respective electrodes. The electric field strength also decreases with depth, further increasing the transit time of the charges. With the mesa design, the distance traveled by a charge is independent of its depth in the crystal, as is the electric field strength. The model derived in this work will be an even better description of the mesa structure photodiode. At IR wavelengths, the diffusion of the photo-generated carriers is less than for uv because of the longer penetration depth in either detector. Hence, the mesa device

might have a better rf quantum efficiency at IR wavelengths than in the uv.

In conclusion, several significant advances in the state of the art of msm photodiodes have been made. A detailed, microscopic model for the detector response has been derived and tested. A unique uv heterodyne system has been built and calibrated. Several detectors were tested and compared to theory. The limitations in the high frequency response of these detectors lies with the rf package, and not with the detectors themselves. The rf package design was a standard one used by many researchers in this area. Given a properly designed rf package, a 4.5- $\mu\text{m}$  gap, 21-GHz bandwidth detector, fabricated on bulk Si, with a 30% quantum efficiency appears feasible. The model predicts that a 1.0- $\mu\text{m}$  gap device would have a 75-GHz bandwidth with a comparable quantum efficiency. This result is a truly remarkable, totally unexpected, and most important result of this work.

Figure 55. Proposed Mesa MSM Photodiode Design, End View.



### References

1. S. M. Sze, Physics of Semiconductor Devices, 2nd Ed., John Wiley and Sons, (1981).

## Appendix I.

### Photoconductor or Photodiode?

During the course of this work, the question of whether reported detector is a photoconductor or a photodiode arose several times. The source of confusion is that a given type, or geometry, detector was reported both as a photodiode and as a photoconductor by different authors. (Sometimes by the same author at different times) As an example, it was found that msm structures were reported as being photoconductors or as photodiodes, depending upon the author. Some confusion appears to exist as to what makes a certain detector a photoconductor or a photodiode. A photoconductive msm structure must function as a resistor in the circuit. However, several sources were found where metal Schottky contacts were laid down on a semiconductor to form the photoconductor. Schottky contacts, if unannealed, are rectifying structures and it appears that the reported detector is really a photodiode. In many cases the author's reporting left much for the reader to assume. Some articles just reported that Al on Si contacts were made, assuming that the reader would realize that Al can easily make ohmic contacts on Si. However, the mention of the necessary thermal annealing of the Al into the Si to form the ohmic contacts was omitted. Other times, the detector made had one true rectifying Schottky contact and one ohmic. Then, by forward biasing the rectifying contact, a true photoconductor was produced. However, the fact that the second metal contact was ohmic was unclear.

Another closely related point of confusion, or more precisely a lack of rigor, is in the frequency response of both photoconductive and photovoltaic detection. A clear distinction between two types of

detection was not found in two standard textbooks.<sup>1,2</sup> Also, a great lack of rigor is missing in the derivations found not only in textbooks, but in many journal articles. The difference between photoconductive and photovoltaic detection is delineated here.

The simplest detection scheme is a photoconductor. An incident photon is absorbed by the detector and an electron-hole pair is created. The motion of the electron and hole sets up a photocurrent in the external circuit. How the detector interacts with the external circuit is the key to whether a detector is a photoconductor or a photodiode. The photoconductive detector acts as a resistor in series with the electronics utilized to measure the photocurrent in the detector. Therefore the current at any point inside of the photoconductive detector is equal to the current in the external circuit, taking into account some propagation time.

This is not the case in a photovoltaic detector such as a photodiode. Photovoltaic detection is where a photon creates a free electron-hole pair in a region where no free charge previously existed. The motion of this charge creates a time varying electric field at the electrodes of the detector. Therefore, all of the charge moving in the region between the electrodes at any one time affects the current in the external circuit. The photodiode acts as a capacitor in series with the external electronics.

A rigorous treatment from first principles for the detector response of an ideal MSM photodiode was presented in Chapter II of this work. As with photodiodes, the derivations of detector response in photoconductors found in the open literature was incomplete. Kingston<sup>1</sup> and Yariv<sup>2</sup> both derive the photoconductive response from a rate equation

and arrive at the same conclusions. This technique is the standard photoconductor calculation found in the literature. In all cases the calculation starts with the equation of continuity,

$$\vec{\nabla} \cdot \mathbf{J} + \partial \rho / \partial t = G - R \quad (\text{A1})$$

where  $G$  and  $R$  are the generation rate due to the incident photons and the recombination rate of the free carrier, respectively. The next step is to invoke steady state conditions and knowing  $G$ , and assuming the  $R$  has the form of the charge density divided by the carrier lifetime, they solve for the steady state charge density. Finally, the illuminating light is turned off and assuming that  $R = \rho / \tau$ , the charge density as a function of time is solved for, resulting in an impulse response of

$$i = i_0 e^{-t/\tau} \quad (\text{A2})$$

The frequency response of the detector is found by taking the Fourier transform of the impulse response resulting in

$$i = \frac{q\eta P}{\hbar\omega_{LO}} \left[ \frac{v\tau}{2x_g} \right] \frac{1}{(1 + \omega^2\tau^2)^{1/2}} \quad (\text{A3})$$

where,  $v$  is the drift velocity of the carrier and  $2x_g$  is the spacing between the ohmic contacts of the photoconductor. The value in parenthesis is the photoconductive gain. The frequency response is seen to drop off as a simple pole with a bandwidth,  $f_p$ , as

$$f_p = \frac{1}{2\pi\tau} \quad (\text{A4})$$

and from this bandwidth and the photoconductive gain, it is seen that the gain-bandwidth product is a constant for a given drift velocity and contact spacing. Hence, by shortening the lifetime of the carriers, the bandwidth may be increased, but only at the expense of the gain. This does not imply that, for a given detector, the gain-bandwidth product will always be constant. For a given detector the only constant is the bandwidth. However, for two detectors with identical contact spacing and drift velocities, the gain-bandwidth product is a constant since the lifetime of the carriers cancel out. Therefore, the bandwidth of a given single detector is a constant and independent of bias. Lowering the bias, which lowers the gain, does not result in an improved bandwidth.

The frequency response derived above was made using a simple steady-state argument based on Eqn A1 without the details of  $\mathbf{J}$  and  $\rho$  distributions. A more rigorous derivation is now presented. First, a one dimensional non-diffusion model is used in order that a direct comparison with the previous theory can be made. The charge density in a semiconductor due to a modulated light source was derived in Chapter II. A simple modification to include recombination can be made to Eqn. 45. Then, following the same steps to arrive at the charge density, given by Eqn 49, gives the charge density with recombination, but not diffusion, included. The complex current,  $i'$ , which is equal to the current density in one-dimension, is then given by

$$i' = v\rho = \frac{q\eta P e^{i\omega t}}{\hbar\omega_{L0}} \exp(-(x-x_0)/v\tau) \exp(-i\omega(x-x_0)/v)$$

(A5)

In a photoconductor, continuity of current demands a constant current equal to the current in the external circuit. Hence, place the light source at  $x_0 = 0$  and evaluate the current at  $x = 0$ . By letting  $t = 0$ , the initial current,  $i_0$ , is

$$i_0 = q\eta P / \hbar\omega_{LO} . \quad (A6)$$

Now, this current exits the photoconductor at  $x = x_G$ , which is 1/2 of the detector width, an additional charge then enters the semiconductor at  $x = -x_G$ . This process continues with an exponential decay representing the carrier recombination. The current then at  $x = 0$  is

$$i' = i_0 + i_1 + \dots = \sum_n i_n \quad (A7)$$

where

$$i_n = \frac{q\eta P}{\hbar\omega_{LO}} \exp\{-n2x_G/v\tau\} \exp\{-i\omega n(2x_G/v)\} \exp\{-i\omega n(2\Phi)\} \quad (A8)$$

where the  $\exp\{-2x_G/v\tau\}$  is the decrease in the amplitude of the current after traveling a total distance of  $2x_G$ , the detector width, due to recombination. The  $\exp\{-i\omega(2x_G/v)\} \exp\{-i\omega n(2\Phi)\}$  is the phase factor for the current after traveling around the circuit. The  $2x_G/v$  is the total time to traverse the detector and  $2\Phi$  is the time for a round trip in the external circuit. The total current in the external circuit is then given by Eqns A7 and A8 which is a geometric series, thus giving for the

total current,

$$i = \text{Re}[i'] = \frac{q\eta P}{\hbar\omega_{LO}} \times \text{Re} \left[ \frac{1}{1 - \exp(-2x_G/v\tau) \exp(-i2\omega[(x_G/v)+\Phi])} \right]. \quad (\text{A9})$$

In the low-frequency region, the detector length,  $2x_G$ , is much less than  $v\tau$ . Also,  $\omega 2x_G \ll v$ , and assuming  $\Phi$  is small, the exponentials can be expanded, keeping only the first terms

$$i \approx \frac{q\eta P}{\hbar\omega_{LO}} \text{Re}([1 - [1 - (2x_G/v\tau) - i2\omega[(x_G/v)+\Phi]]]^{-1}) \quad (\text{A10})$$

which gives, assuming  $\Phi = 0$ ,

$$i \approx \frac{q\eta P}{\hbar\omega_{LO}} \left[ \frac{v\tau}{2x_G} \right] \frac{1}{(1 + \omega^2\tau^2)^{1/2}} \quad (\text{A3})$$

which is exactly the expression that both Kingston and Yariv derived for a photoconductor! It is clearly seen that, in the low-frequency limit, Eqn A9 reduces to the form previously derived by the simple steady-state argument given by Eqn A3. However, Eqn A9 also shows that the photoconductor will have a high-frequency response when the phase term goes to an integral value of  $2\pi$ . This corresponds to all of the sinusoidal currents adding in phase, producing a resonance condition in

the detector and external circuit. The condition for this resonance is

$$n2\pi = 2\omega((x_G/v) + \Phi) \quad (A12)$$

which implies that the resonance frequency,  $f_R$ , is

$$f_R = \frac{n}{((2x_G/v) + 2\Phi)} \quad (A13)$$

which is integral multiples of one over the round trip time for the current. For example, consider a Si photoconductor with  $2x_G = 1 \mu\text{m}$ . Assume a bias sufficient to produce  $v = 5 \times 10^6 \text{ cm/sec}$  and a nominal recombination time for bulk Si of  $10^{-3} \text{ sec}$ . Eqn (A8) predicts that the -3 db point would be at approximately 280 Hz, and that the frequency response would continue to roll-off at -10 db per decade increase in frequency. However, if  $\Phi = 0$ , which implies an infinite speed of light in the external circuit (i.e. an ideal circuit), then the first resonance should occur at 50 GHz and have the same amplitude as the d.c. photocurrent. This high amplitude, however, will not be seen since the external circuit will have considerably more loss at 50 GHz than it will at d.c. Diffusion, RC, L/R and other detector parameters will also cause the frequency response to fall off and this fast resonance will probably not be seen.

The problem of a leaky photodiode detector is now addressed. Virtually every report of MSM photodiodes has commented on an enhanced-low-frequency response over that at high frequency. This enhanced-low-frequency behavior is evident in the  $R(\omega)$  data previously presented in this work. The effect has not, until now, been successfully explained. Many conjectures have been put forth, but no satisfactory identification

of this mechanism have been made. Here, a partial explanation of this enhanced-low-frequency behavior is attempted.

The barriers of an ideal photodiode are sufficiently high, under reverse bias conditions, such that there is no leakage current. Real diodes, however, have some leakage current associated with them. Any current traveling around the external circuit will eventually arrive at one of the diode junctions in an MSM device. The leaky nature of the diode barrier should allow a small fraction,  $T$ , of this current through the barrier back into the depletion region of the MSM photodiode. This appears to be somewhat similar to the photoconductor, except that this device has a reduction in the current that is due to more than recombination. Also, the device is still working as a photovoltaic device, implying that the space average current in the depletion region is what is seen in the external current, not the current at any given point in the semiconductor. The space average photocurrent,  $i_o'$ , can be found by setting  $t = 0$  and integrating Eqn A5, resulting in

$$i_o' = \frac{q\eta P}{\hbar\omega_{LO}} \left[ \frac{1 - \exp\{-(x_G - x_o)[(1/v\tau) + (i\omega/v)]\}}{(x_G - x_o)[(1/v\tau) + (i\omega/v)]} \right] \quad (A14)$$

which reduces to Eqn 54 in Chapter II when the recombination time  $\tau$  goes to infinity. This initial photocurrent,  $i_o'$ , is the current in the external circuit from the incident point source of light located at  $x = x_o$ . Now, this current travels around the circuit in a time  $\Phi$ , and arrives at the electrode located at  $x = -x_G$ . The leaky barrier then transmits a portion,  $T$ , back into the photodiode. This acts as a second

source of current, but now located at  $x = -x_G$ , instead of  $x = x_0$ . The current due to this leakage is given by Eqn A14 with the replacement of the amplitude  $q\eta P/\hbar\omega_{LO}$  by the product of T and Eqn A14, giving the current,  $i_1'$ , in the semiconductor as a function of position as

$$i_{10}' = \frac{q\eta P}{\hbar\omega_{LO}} \left[ \frac{1 - \exp(-(x_G - x_0)[(1/v\tau) + (i\omega/v)])}{(x_G - x_0)[(1/v\tau) + (i\omega/v)]} \right] \times \exp(-(x+x_G)/v\tau) \exp(-i\omega[(x+x_G)/v]) \exp(-i\omega\Phi) \quad (A15)$$

The current in the external circuit due to this leaking diode,  $i_1'$ , is again the space average current in the diode, thus

$$i_1' = \frac{1}{2x_G} \int_{-x_G}^{+x_G} dx i_{10}' \quad (A16)$$

This current, due to the leakage of the original photocurrent, again travels through the external circuit to arrive back at the diode to start the leakage process over again. Hence, the above process is repeated  $n$  times until the current finally dies out. The expression for

the leakage current on its nth round trip,  $i_n'$ , can be expressed as

$$i_{in}' = \frac{q\eta P}{\hbar\omega_{LO}} \left[ \frac{1 - \exp\{-(x_G - x_0)[(1/v\tau) + (i\omega/v)]\}}{(x_G - x_0)[(1/v\tau) + (i\omega/v)]} \right] \times \left[ \frac{\text{Te}^{i\omega t} \left[ 1 - \exp\{-2x_G[(1/v\tau) + (i\omega/v)]\} \right]}{2x_G[(1/v\tau) + (i\omega/v)]} \right]^n \quad (\text{A17})$$

and the total current measured in the external circuit is given by the summation of the  $i_n'$ 's,

$$i' = \sum_{n=0}^{\infty} i_n'$$

which is a geometric series, giving

$$i' = \frac{q\eta P}{\hbar\omega_{LO}} \left[ \frac{1 - \exp\{-(x_G - x_0)[(1/v\tau) + (i\omega/v)]\}}{(x_G - x_0)[(1/v\tau) + (i\omega/v)]} \right] \times \left[ 1 - \left[ \frac{\text{Te}^{i\omega t} \left[ 1 - \exp\{-2x_G[(1/v\tau) + (i\omega/v)]\} \right]}{2x_G[(1/v\tau) + (i\omega/v)]} \right] \right]^{-1} \quad (\text{A18})$$

Notice that as  $T$  approaches zero, as for an ideal photodiode, that the expression for  $i'$  approaches that of an ideal photodiode given by Eqn A14. For the low-frequency behavior, the exponential in the second bracket term is now expanded and the first three terms are kept,

resulting in

$$i' \approx \frac{q\eta P}{\hbar\omega_{LO}} \left[ \frac{1 - \exp\{-(x_G - x_0)[(1/v\tau) + (i\omega/v)]\}}{(x_G - x_0)[(1/v\tau) + (i\omega/v)]} \right] \times$$

$$\left[ \frac{1}{1 - T + Tx_G(1 + i\omega\tau)/v\tau} \right]$$

(A19)

The above expression looks very much like a photoconductor with gain of  $v\tau/Tx_G$  and a single pole roll-off determined by the recombination time. However, as  $T$  goes to zero, the photodiode portion dominates. As  $T$  goes to unity, as the case for a photoconductor, the photodiode portion is unchanged, but the photoconductive nature of the detector dominates, such that the device behaves as an ideal photoconductor. However, the roll-off of the above equation is much more severe than is actually measured in an MSM photodiode. However, one can see how a transition from a photodiode to a photoconductor can be made by using a simple, leaky diode model.

In conclusion, a concise explanation between a photoconductive and photovoltaic detector has been given. Shortcomings in the preciseness in the literature as to why a given detector is either a photoconductor or a photovoltaic device has been shown. Also, a theoretical description in one-dimension, without diffusion, of the frequency response characteristics of the photoconductor has been derived from first principles for the first time. The results of the calculations reduce to that derived by a less rigorous rate-equation argument which is widely used. The new model not only predicts the low-frequency

behavior of the photodiode, but also predicts the existence of several high-frequency resonances in the detector. Further development of this model to include diffusion could, in practice, be accomplished by identical steps as used here, but starting with the current given by Eqn 75 in Chapter II. The generalization is left as an exercise to the reader. Finally an attempt at explaining the enhanced-low-frequency response of msm photodiodes with a simple leaky diode model was attempted with only limited success.

### References

1. R. H. Kingston, Detection of Optical and Infrared Radiation, Springer-Verlag, (1979).
2. A. Yariv, Introduction to Optical Detection, Holt, Reinhart and Winston, (1976).